Fictive Impurity Approach

to

Dynamical Mean Field Theory

Dissertation

zur

Erlangung des Doktorgrades (Dr. rer. nat.)

der

Mathematisch-Naturwissenschaftlichen Fakultät

der

Rheinischen Friedrich-Wilhelms-Universität Bonn

vorgelegt von

Andreas Fuhrmann

aus

Krasnojarsk

Bonn 2006

Angefertigt mit Genehmigung der Mathematisch-Naturwissenschaftlichen
Fakultät der Rheinischen Friedrich-Wilhelms-Universität Bonn.
Diese Dissertation ist auf dem Hochschulschriftenserver der ULB Bonn
$http://$`hss.ulb.uni`$-$`bonn.de/diss_online` electronisch publiziert.

1. Referent: Professor H. Monien, Universität Bonn.
2. Referent: Professor A. J. Millis, Columbia University, New York.

Tag der Promotion: 07.07.2006

Contents

Chapter 1

Fictive Impurity Models

1.1 Introduction

"Strongly correlated" materials [1] illustrate one of the most important tasks in condensed matter physics. These materials show a wide spectrum of exciting and useful properties including high temperature superconductivity [2] and magnetism with high spin polarization [3]. The electron-electron and electron-lattice interactions in "strongly correlated" materials are so strong, that the conventional method (that computes bands using density functional theory and treats the residual interactions between quasiparticles using perturbative approaches) fails. Developing a credible, material-specific theoretical framework for determining the behavior of strongly correlated compounds is a significant challenge to materials theory.

The dynamical mean-field theory (DMFT) formulated by A. Georges and co-workers [4] is a fundamental step forward in the treating of correlated systems. It is a local approximation where the self-energy keeps the frequency dependence but becomes momentum-independent. The mean-field theory allows the construction of a non-perturbative and computationally controllable theoretical procedure for computing physical properties. The self-energy is a function of frequency only, thus one can see it as the self-energy of a single-site "quantum impurity model", with the model parameters specified by a self-consistency condition. The method works very well by consideration of the Mott-transition in electronically three dimensional materials [5], the "double exchange" physics especially important for colossal magneto-resistance manganites [6], and the basic physics of heavy fermion compounds [7], in which the dominant physics is on-site. However, the inter-site correlations play an important role in the physics. For example, predictions of the single-site DMFT about the high temperature superconductors disagree strongly with data on the evolution with doping of quasiparticle velocity and "Drude" optical weight [8] and the orbital order/polaron glass physics of the manganites [9]. Therefore extension of the dynamical mean field method to include inter-site correlations is a reasonable step.

The main feature of the single-site dynamical mean-field theory is the mapping of the lattice model onto a single-site quantum impurity model, that is self-consistently embedded in a bath/medium. The natural extension is a change over to multiple-site quantum
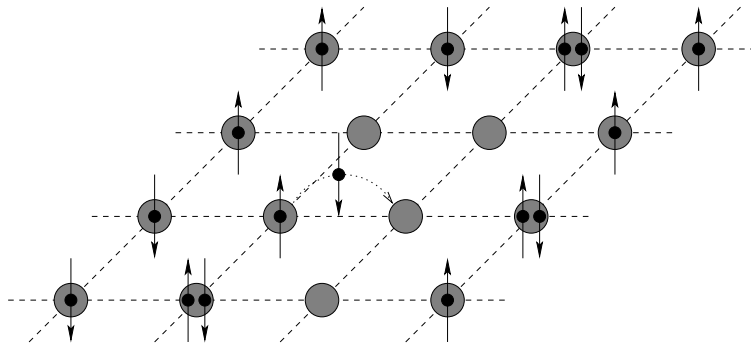
Figure 1.1: Sketch of the quadratic half-filled lattice. Black filled circles with arrows symbolize fermions with corresponding orientation of the spin's z-component.

impurity model, whose various self-energies could be used to compute a better representation of the lattice self-energy. The extensions like "Cellular-DMFT" (CDMFT) [10] and "Dynamical cluster approximation" (DCA) [11] have been proposed. A recent proposition, fictive impurity (FI) method [12], unifies the picture, in which the DCA and cluster approaches correspond to different choices of the basis in the same general expansion.

The goal of this work is a systematic analysis of the fictive impurity method, identification of advantages and disadvantages in the generalization on the basis of comparison with single impurity, DCA and analytical results. In particular we consider the self-energies, the inter-site spin-spin correlations, the internal energies, and the phase diagram.

In our study we investigate a 2-dimensional Hubbard model, which is one of the basic models, that describes interacting particles on the lattice [13]. It is the simplest strongly correlated many-particle system, where the kinetic energy and the on-site interaction have the same order, which cannot be reduced to a single-particle theory. The Hubbard model incorporates the short-range part of the Coulomb interactions, while avoiding the high complexity (such as screening effects) of the long-range Coulomb force. The Hamiltonian is given by

$$H = - \sum_{\langle i,j\rangle,\sigma} t_{ij} c_{i\sigma}^{\dagger} c_{j\sigma} + U \sum_i n_{i\uparrow} n_{i\downarrow}, \tag{1.1}$$

where $c_{i\sigma}^{\dagger}(c_{i\sigma})$ creates (annihilates) a fermion with spin σ at site i and the operator $n_{i\sigma} = c_{i\sigma}^{\dagger} c_{i\sigma}$ gives the number of particles with spin σ on site i, t_{ij} is the in-plane hopping matrix element and U is the Coulomb repulsion. We only consider the short-range hopping, thus $\sum_{\langle i,j\rangle}$ denotes the sum over all nearest-neighbors.

The 2-dimensional quadratic lattice at half-filling with dispersion

$$\varepsilon_{\boldsymbol{p}} = 2(\cos(p_x) + \cos(p_y)) \tag{1.2}$$

was used in present computations. There are two reasons to treat such a lattice: First, the x- and y-symmetry simplifies calculations. Second, a lot of interesting materials consist of the planes with the same structure. In fact, a number of high temperature superconductors

include CuO-planes, which have a quadratic layout of sites. An idealized quadratic lattice is shown in Figure 1.1. The lattice constant was set equal unity in present work.

The rest of this chapter is organized as follows: Section 1.2 presents the fictive impurity formalism as well as the formulation of the dynamical cluster approximation. Section 1.3 gives an overview over numerical techniques we used. In general, the N-impurity problem was solved using a semiclassical approximation [14] partly using Hirsh-Fye Monte Carlo algorithm [4]. Furthermore some practical computational hints will be found in this section. Section 1.4 guides through a large-U analytical treatment, was used to check our computational results. Section 1.5 gives the numerical results. Conclusion and outlook can be found in the last section of the present chapter.

1.2 Analytical Approaches

1.2.1 Fictive Impurity Models

The fictive impurity method is an alternative formulation of the cluster dynamical mean-field theory. The main idea is to expand the self-energy using a set of harmonic orthogonal functions and cut the expansion at a finite order, thereby replacing a general function by a small number of frequency-dependent coefficients, which may be determined from the solution of a several site fictive impurity model. The term "fictive impurity" because the cluster does not need to be a subcluster of the physical lattice, it can be any cluster self-consistently embedded in a medium.

Formalism

The model that we consider is a d-dimensional lattice with electrons moving with short ranged hopping amplitudes and interactions. The Hamiltonian is $H = H_0 + H_{\text{int}}$. The physical properties of the model can be derived from the general "Luttinger-Ward" expression for the action written in terms of the exact Green function G of the model [15, 12, 16]

$$S = \text{Trln}(-G) + \bar{\Phi}_{\text{skel}}[G], \tag{1.3}$$

where $\bar{\Phi}_{\text{skel}}[G]$ is the sum of all vacuum to vacuum "skeleton" diagrams, drawn with full Green functions and no self-energy insertions (Fig. 1.2). The electron's self-energy is determined via

$$\Sigma = \frac{\delta \bar{\Phi}_{\text{skel}}}{\delta G}. \tag{1.4}$$

Variation of the action (1.3) with respect to G and following substitution in of equation (1.4) lead to

$$\frac{\delta S}{\delta G} = G^{-1} + \Sigma = G_0^{-1} \equiv -(\delta_t - H_0). \tag{1.5}$$

In order to get convenience in the following derivation we make use of a Legendre trans-
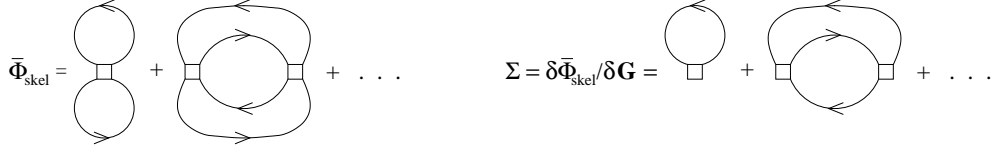
Figure 1.2: First two orders of the diagrammatic presentation of the Luttinger-Ward functional $\bar{\Phi}_{\mathrm{skel}}$ and the corresponding self-energy Σ, obtained by the variation of functional with respect to G.

formation and obtain a "new" Luttinger-Ward functional as a functional of Σ

$$\Phi_{\mathrm{skel}}[\Sigma] = \bar{\Phi}_{\mathrm{skel}} - \mathrm{Tr}(\Sigma G). \tag{1.6}$$

One can easily see, that equations (1.4) and (1.6) denote

$$\frac{\delta\Phi_{\mathrm{skel}}}{\delta\Sigma} = \frac{\delta\bar{\Phi}_{\mathrm{skel}}}{\delta G}\frac{\delta G}{\delta\Sigma} - G - \Sigma\frac{\delta G}{\delta\Sigma} = -G, \tag{1.7}$$

where $G[\Sigma]$ is identical to the G obtained via the Dyson equation

$$G[\Sigma] = (G_0^{-1} - \Sigma)^{-1}, \tag{1.8}$$

that can be derived by minimizing the functional

$$\Omega[\Sigma] = -\mathrm{Trln}(-G_0^{-1} + \Sigma) + \Phi_{\mathrm{skel}}[\Sigma] \tag{1.9}$$

with respect to Σ.

The dynamical mean field theory (DMFT)[4] can be derived from the equations (1.6) and (1.8): Define Φ_{loc} as an approximation to the exact $\Phi_{\mathrm{skel}}[\Sigma(\boldsymbol{p},\omega)]$, where the momentum-dependent self-energy is substituted by the local, only frequency-dependent self-energy $\Sigma_{\mathrm{loc}}(\omega) = \int(dp)\Sigma(\boldsymbol{p},\omega)$. Consistency demands, that it is equivalent to replacement $\bar{\Phi}_{\mathrm{skel}}[G]$ by $\bar{\Phi}_{\mathrm{skel}}[G_{\mathrm{loc}}]$ in equation (1.6), where $G_{\mathrm{loc}}(\omega) = \int(dp)G(\boldsymbol{p},\omega)$. Equation (1.8) transforms into equation $G_{\mathrm{loc}} = \int(dp)[G_0^{-1}(\boldsymbol{p},\omega) - \Sigma(\omega)]^{-1}$. The crucial observation which makes the single-site DMFT useful is that because Φ_{loc} is a functional of a function of frequency, it may be defined non-perturbatively as the solution of a single-site model, which is specified by a frequency-dependent Weiss field and by interaction terms related to the local interactions of the original model. The Weiss field is fixed by demanding that the impurity Green function is equal to the local Green function calculated from the lattice Hamiltonian, using the impurity model self-energy.

The DMFT can be generalized using a set of orthogonal functions $\{\phi_i, \psi_i\}$, which satisfy the following requirement

$$\delta_{\boldsymbol{p},\boldsymbol{p}'} = \sum_i \phi_i(\boldsymbol{p})\psi_i(\boldsymbol{p}'). \tag{1.10}$$

The self-energy becomes momentum-dependent

$$\Sigma(\boldsymbol{p}, \omega) = \sum_i \phi_i(\boldsymbol{p})\Sigma_i(\omega), \tag{1.11}$$

where $\Sigma_i(\omega) = \int(dp)\psi_i(\boldsymbol{p})\Sigma(\boldsymbol{p}, \omega)$. Inserting of the self-energy in equation (1.6) leads to

$$\Phi_{\text{skel}}[\{\Sigma_i\}] = \bar{\Phi}_{\text{skel}} - \sum_i \text{Tr}(\Sigma_i G_i), \tag{1.12}$$

with $G_i(\omega) = \int(dp)\phi_i(\boldsymbol{p})G(\boldsymbol{p}, \omega)$. The approximant for the self-energy in equation (1.11) is a sum that we truncate after the n'th summand

$$\Sigma(\boldsymbol{p}, \omega) \approx \Sigma_{\text{approx}}(\boldsymbol{p}, \omega) \equiv \sum_{i=0}^{n} \phi_i(\boldsymbol{p})\Sigma_i(\omega). \tag{1.13}$$

Thus $\Phi_{\text{approx}}[\Sigma_{\text{approx}}]$ is a functional obtained from Φ_{skel} by using the approximate self-energy instead of the exact one. Now Φ_{approx} is a functional of $n+1$ frequency dependent fields. Therefore it corresponds to the solution to $(m+1)$-site fictive impurity model ($n \leq m$) involving $n+1$ Weiss fields, and interactions derived from the original model. The Weiss fields are fixed by equation

$$G_i = -\frac{\delta\Phi_{\text{approx}}}{\delta\Sigma_i}, \tag{1.14}$$

where

$$G_i = \int(dp)\phi_i(\boldsymbol{p})[G_0^{-1}(\boldsymbol{p}, \omega) - \Sigma_{\text{approx}}(\boldsymbol{p}, \omega)]^{-1}. \tag{1.15}$$

The impurity model becomes a mathematical instrument that will be used to calculate the set of coefficients Σ_i for the self-energy Σ_{approx}.

Implementation

Generalization In order to extend the dynamical mean field theory we need to find an impurity model that yields the frequency-dependent expansions coefficients in equation (1.11). The model must involve n fields which have an orthogonality property, so that it will be possible to determine n independent Green functions and self-energies. It is convenient to define a m-component spinor of Grassmann variables ψ with ($n \leq m$). The action[1] in this notation is defined as

$$S = \psi^{\dagger}\left[\sum_{i=0}^{n} a_i \hat{M}_i\right]\psi + S_{\text{int}}, \tag{1.16}$$

where a_i are the frequency-dependent Weiss fields and $\hat{M}_i$ are the $m \times m$ matrices, which comply with the requirement

$$\text{Tr}[\hat{M}_i \cdot \hat{M}_j] = m\delta_{ij}. \tag{1.17}$$

---

[1]We do not write the imaginary time integration in this equation explicit.

The matrix $\hat{M}_0$ is the identity matrix. The impurity Green function in this presentation is

$$\hat{G}_{\mathrm{imp}} = \sum_{i=0}^{n} G_{\mathrm{imp}\,i}\hat{M}_i, \tag{1.18}$$

with

$$G_{\mathrm{imp}\,i} = \frac{1}{m}\frac{\delta \ln Z_{\mathrm{imp}}}{\delta a_i}. \tag{1.19}$$

The orthogonality relations lead to the self-energies

$$\Sigma_{\mathrm{imp}\,i} = \frac{1}{m}\mathrm{Tr}\left[\hat{M}_i\left(\sum_{j=0}^{n} a_j\hat{M}_j - \hat{G}_{\mathrm{imp}}^{-1}\right)\right], \tag{1.20}$$

which are equal to the frequency-dependent coefficients in equation (1.13).

The upper formalism is specified for the paramagnetic order. To complete the picture, we should discuss some variations, which we have, if the system becomes antiferromagnetic. The antiferromagnetic order leads to a spin-dependency in Green functions, in Weiss fields and in self-energies. The "matrix-split" $\hat{M}_i = \hat{M}_{i\sigma} + \hat{M}_{i\bar{\sigma}}$ allows to save the upper elegancy and to wright equations (1.18) – (1.20) in the antiferromagnetic form:

$$
\begin{aligned}
\hat{G}_{\mathrm{imp}} &= \sum_{\sigma}\sum_{i=0}^{n} G_{\mathrm{imp}\,i\sigma}\hat{M}_{i\sigma} \\
G_{\mathrm{imp}\,i\sigma} &= \frac{1}{m}\frac{\delta \ln Z_{\mathrm{imp}}}{\delta a_{i\sigma}} \\
\Sigma_{\mathrm{imp}\,i\sigma} &= \frac{2}{m}\mathrm{Tr}\left[\hat{M}_{i\sigma}\left(\sum_{\sigma}\sum_{j=0}^{n} a_{j\sigma}\hat{M}_{j\sigma} - \hat{G}_{\mathrm{imp}}^{-1}\right)\right].
\end{aligned}
\tag{1.21}
$$

Note that, the matrices $\hat{M}_{i\sigma}$ and $\hat{M}_{i\bar{\sigma}}$ together have the same number of non-zero matrix-elements like $\hat{M}_i$ (compare section 1.3.1).

Harmonic expansion In this section we expand the self-energy using orthogonal harmonic functions and truncate the expansion after the third summand. The self-energy becomes

$$\Sigma_{\sigma}(\boldsymbol{p}, \omega) \approx \Sigma_{0\sigma}(\omega) + \sum_{\boldsymbol{r}} e^{i\boldsymbol{p}\boldsymbol{r}}\Sigma_{\boldsymbol{r}\sigma}(\omega) + \sum_{\boldsymbol{r}'} e^{i\boldsymbol{p}\boldsymbol{r}'}\Sigma_{\boldsymbol{r}'\sigma}(\omega), \tag{1.22}$$

where the $\boldsymbol{r}$-sum is a sum over all nearest neighbors (NN) and the $\boldsymbol{r}'$-sum over all next nearest neighbors (NNN). Generally speaking we need $2(1 + 2d + 2d(d-1))$ fields to solve this problem. In this chapter we consider the hypercubic d-dimensional lattice[2], therefore we assume, that $\Sigma_{\boldsymbol{r}\sigma}(\omega) = \Sigma_{1\sigma}(\omega)$ for all NN's and $\Sigma_{\boldsymbol{r}'\sigma}(\omega) = \Sigma_{2\sigma}(\omega)$ for all

---

[2]The lattice constant a is equal 1.

NNN's. It means that we only need 3 (6) fields to solve the problem in the paramagnetic (antiferromagnetic) case. So the straightforward transformation leads to

$$\Sigma_\sigma(\boldsymbol{p}, \omega) \approx \gamma_{\boldsymbol{p}}^{(0)} \Sigma_{0\sigma}(\omega) + 2d\gamma_{\boldsymbol{p}}^{(1)} \Sigma_{1\sigma}(\omega) + 2d(d-1)\gamma_{\boldsymbol{p}}^{(2)} \Sigma_{2\sigma}(\omega), \tag{1.23}$$

and the momentum dependent $\gamma_{\boldsymbol{p}}$'s are defined as

$$\begin{aligned} \gamma_{\boldsymbol{p}}^{(0)} &= 1 \\ \gamma_{\boldsymbol{p}}^{(1)} &\equiv \frac{1}{2d} \sum_{\boldsymbol{r}} e^{i\boldsymbol{p}\boldsymbol{r}} = \frac{1}{d} \sum_{i=1}^{d} \cos(p_i) \\ \gamma_{\boldsymbol{p}}^{(2)} &\equiv \frac{1}{2d(d-1)} \sum_{\boldsymbol{r}'} e^{i\boldsymbol{p}\boldsymbol{r}'} = \frac{1}{d(d-1)} \sum_{i=1}^{d} \sum_{\substack{j=1 \\ j \neq i}}^{d} \cos(p_i)\cos(p_j). \end{aligned} \tag{1.24}$$

Using the upper notations the mean field equations become

$$G_{\text{imp}\,i\sigma} = \frac{1}{m}\frac{\delta \ln Z_{\text{imp}}}{\delta a_{i\sigma}} = \int (dp)\gamma_{\boldsymbol{p}}^{(i)} G_\sigma(\boldsymbol{p}, \omega), \tag{1.25}$$

where i=0,1,2.

Green function In current paragraph we will discuss the calculation of the lattice Green function (1.25) in the paramagnetic and antiferromagnetic regime.

The Green function as a function of the fermionic Matsubara frequencies in the paramagnetic order is defined as

$$G_\sigma(\boldsymbol{p}, \omega_n) = (i\omega_n + \mu - \varepsilon_{\boldsymbol{p}} - \Sigma_\sigma(\boldsymbol{p}, \omega_n))^{-1}, \tag{1.26}$$

with the lattice self-energy (1.23) and $\varepsilon_{\boldsymbol{p}}$ is the energy dispersion, which is defined as $\varepsilon_{\boldsymbol{p}} = -2dt\gamma_{\boldsymbol{p}}^{(1)}$ in the d-dimensional square lattice, with $t = t_{ij}\sqrt{2d}$ [4]. The $G_\sigma(\omega_n)$ is equal to the $G_{\bar{\sigma}}(\omega_n)$ in the paramagnetic case. The integration over the Brillouin zone leads to the lattice Green functions

$$G_{i\sigma}(\omega_n) = \frac{1}{(2\pi)^2} \int_{-\pi}^{\pi} dp_x \int_{-\pi}^{\pi} dp_y \gamma_{\boldsymbol{p}}^{(i)} G_\sigma(\boldsymbol{p}, \omega_n). \tag{1.27}$$

In the antiferromagnetic order one should consider two sublattices (A and B). The sublattice A(B) includes all sites with spin-up(-down) fermions in the Néel phase. In present work we only consider the nearest neighbor hopping, therefore the kinetic part of the Hamiltonian describes the hopping between two sublattices

$$H_{\text{kin}} = \sum_{\boldsymbol{p} \in \text{RBZ}, \sigma} \begin{pmatrix} c_{A\boldsymbol{p}\sigma}^\dagger & c_{B\boldsymbol{p}\sigma}^\dagger \end{pmatrix} \begin{pmatrix} 0 & \varepsilon_{\boldsymbol{p}} \\ \varepsilon_{\boldsymbol{p}} & 0 \end{pmatrix} \begin{pmatrix} c_{A\boldsymbol{p}\sigma} \\ c_{B\boldsymbol{p}\sigma} \end{pmatrix}, \tag{1.28}$$

where RBZ is a reduced Brillouin zone. According to the Hamiltonian (1.28) the Green function becomes a 2×2 matrix

$$\hat{G}_\sigma(\boldsymbol{p}, \omega_n) = \begin{pmatrix} G_{0\sigma} & G_{1\sigma} \\ G_{1\sigma} & G_{0\bar{\sigma}} \end{pmatrix} = \left((i\omega_n + \mu)\hat{1} - \hat{\varepsilon}_{\boldsymbol{p}} - \hat{\Sigma}_\sigma(\boldsymbol{p}, \omega_n) \right)^{-1}, \qquad (1.29)$$

with the self-energy matrix accords to equation (1.23), where

$$\hat{\Sigma}_{0\sigma} = \begin{pmatrix} \Sigma_{0\sigma} & 0 \\ 0 & \Sigma_{0\bar{\sigma}} \end{pmatrix}, \hat{\Sigma}_{1\sigma}(\omega_n) = \begin{pmatrix} 0 & \Sigma_{1\sigma} \\ \Sigma_{1\sigma} & 0 \end{pmatrix}, \hat{\Sigma}_{2\sigma}(\omega_n) = \begin{pmatrix} \Sigma_{2\sigma} & 0 \\ 0 & \Sigma_{2\bar{\sigma}} \end{pmatrix}. \qquad (1.30)$$

We do not write the ω_n-dependency of the matrix elements explicit. The diagonal elements of the self-energy $\hat{\Sigma}_\sigma(\boldsymbol{p}, \omega_n)$ are a sum of the on-site and the next nearest neighbor self-energy (interaction on the same sublattice). The off-diagonal entries present the nearest neighbor self-energy (interaction between fermions sitting on different sublattices).

Using the impurity Green function we obtain lattice Green functions

$$\hat{G}_{i\sigma}(\omega_n) = \frac{1}{(2\pi)^2} \int_{-\pi}^{\pi} dp_x \int_{-\pi}^{\pi} dp_y \gamma_{\boldsymbol{p}}^{(i)} \hat{G}_\sigma(\boldsymbol{p}, \omega_n), \qquad (1.31)$$

where $\gamma_{\boldsymbol{p}}^{(1)} = 0$ and $\gamma_{\boldsymbol{p}}^{(1)} = 0$ or $\gamma_{\boldsymbol{p}}^{(2)} = 0$ in case of 1- or 2-site cluster respectively.

Filtering

The self-energy in the fictive impurity method is defined as an *infinite* sum of $\phi_i(\boldsymbol{p})\Sigma_i(\omega)$ terms (1.11), which cannot be realized using numerical methods. For this reason we approximate the self-energy by the *finite* sum (1.13), and that leads to unphysical results such: causality violence in the self-energy, appearance of mid-gap states in the Mott phase and overestimating of the Néel temperature at large-U. The source of these troubles is probably the insufficient number of the orthogonal functions we take into account. In fact, generally one can reproduce a function using an infinite set of orthogonal functions (e.g. Fourier transformation), a finite set leads however to the "ringing" effects [12]. In order to avoid this technical problem in the fictive impurity formalism we introduce a set of filtering functions $\{f_i\}$ which transforms the self-energy (1.13) to

$$\Sigma(\boldsymbol{p}, \omega) \approx \Sigma_{\text{approx}}(\boldsymbol{p}, \omega) \equiv \sum_{i=0}^{n} f_i \phi_i(\boldsymbol{p})\Sigma_i(\omega) \qquad (1.32)$$

where $f_0 = 1$ and $0 \leq f_{i>0} < 1$. According to the derivation of the previous section and using equation (1.32) we get the lattice Green functions

$$G_i(\omega) = \frac{\partial \Omega_{\text{approx}}}{\partial \Sigma_i(\omega)} = f_i \int (dp)\phi(\boldsymbol{p})G(\boldsymbol{p}, \omega). \qquad (1.33)$$

The filtering functions considered here are frequency independent, which is a simple but a bit rude way to solve the truncating problem. It was found [12] that not all frequencies

are affected by the "ringing" effects, therefore a frequency dependent filtering can yield more exact results. The weak point is the numerical determination of so-called "bad" frequencies: The self-energy as a function of the Matsubara frequencies needs a relatively complex procedure for the analytical transformation, which is difficult to realize in each DMFT of the iteration.

Other quantities

This section introduce some quantities we calculated in the present work to compare the fictive impurity method with an other approach. Furthermore one will find couple of analytical quantities used as a benchmark in this work.

Internal energy   In order to get a general idea about the FI method we computed the internal energy as a function of T. A detailed derivation of energy was obtained according to the book by Fetter and Walecka [17] and is presented in the appendix A.2. Taking the final equation (A.19) we get the internal energy in the paramagnetic order

$$E = -T \sum_{n,\sigma} \frac{1}{(2\pi)^2} \int_{-\pi}^{\pi} dp_x \int_{-\pi}^{\pi} dp_y \left(\varepsilon_{\boldsymbol{p}} + \frac{1}{2} \Sigma_\sigma(\boldsymbol{p}, \omega_n) \right) G_\sigma(\boldsymbol{p}, \omega_n), \qquad (1.34)$$

with Green function (1.26) and the self-energy (1.23).

In the antiferromagnetic regime the dispersion, the self-energy and the Green function become 2×2 matrices, on that account we substitute the σ-sum in (1.34) by a trace and obtain the internal energy

$$E = -T \sum_n \frac{1}{(2\pi)^2} \int_{-\pi}^{\pi} dp_x \int_{-\pi}^{\pi} dp_y \mathrm{Tr} \left[\left(\hat{\varepsilon}_{\boldsymbol{p}} + \frac{1}{2} \hat{\Sigma}_\sigma(\boldsymbol{p}, \omega_n) \right) \hat{G}_\sigma(\boldsymbol{p}, \omega_n) \right], \qquad (1.35)$$

where $\hat{\varepsilon}_{\boldsymbol{p}} = \begin{pmatrix} 0 & \varepsilon_{\boldsymbol{p}} \\ \varepsilon_{\boldsymbol{p}} & 0 \end{pmatrix}$. The kinetic energy can be computed analog according to equation (A.20).

We verified our numerical results, comparing them with the analytical value of the internal energy in the atomic limit. The energy was calculated using the grand canonical potential Ω

$$E = \Omega + TS = \Omega - T\frac{\partial \Omega}{\partial T}, \qquad (1.36)$$

where S is the entropy. A paper by Kubo [18], which contains an analytical expansion of Ω up to fourth order in t, was used for the calculation of the internal energy (for details see appendix A.2).

Spin-spin correlation   Also the $\langle \sigma_{iz} \sigma_{jz} \rangle$-correlator was computed for the nearest neighbors as well as for the next nearest neighbors. An analytical value for estimation of the

numerical results was calculated using high-T series expansion of $\langle \boldsymbol{S}_1 \cdot \boldsymbol{S}_2 \rangle$ up to second order in t. Treating the Heisenberg model in the high-T limit (see appendix A.3) leads to

$$\langle \sigma_{1z} \sigma_{2z} \rangle = -\frac{t^2}{TU}. \tag{1.37}$$

The numerical calculation of the correlator depends on the impurity problem solver, and will be discussed later.

The equations of the current chapter are complete to treat those clusters which required one, two or three Weiss fields using the fictive impurity method. In order to expand these equations to consider larger number of fields one should start with a further expansion of the self-energy and follow the schema given above.

1.2.2 Dynamical Cluster Approximation

In the present work we compare our results calculated by the fictive impurity method with the results estimated by the dynamical cluster approximation (DCA) [11]. Therefore we introduce the DCA formulation in this section. Moreover we present the implementation for a 2- and 4-site cluster.

Formalism

In contrast to the single impurity DMFT, we consider a cluster of size N_c with periodic boundary conditions. The cluster should be a part of the physical lattice. The Brillouin zone is divided into N_c regions of equal areas, called reduced Brillouin zones (RBZ). The self-energy in each region becomes a constant value $\Sigma_\sigma(\boldsymbol{p}_k, \omega)$, where $\boldsymbol{p}_k$ is a momentum from the corresponding RBZ[3]. Figure 1.3 shows examples for 2- and 4-site cluster as a part of the 2-dimensional quadratic lattice and the corresponding participation of the Brillouin zone. Each color in the Brillouin zone corresponds to a certain value of the self-energy.

Now the procedure is the following: At first we solve the N_c-impurity problem and get in general N_c or ($2N_c$ in the antiferromagnetic case) Green functions. The Green function in real space, obtained from the impurity problem as well as the initial Weiss field, becomes momentum dependent after a simple discrete Fourier transformation

$$G_\sigma(\boldsymbol{p}_k, \omega) = \sum_{j=1}^{N_c} G_\sigma(\boldsymbol{r}_j, \omega) e^{i\boldsymbol{p}_k \cdot \boldsymbol{r}_j}$$

$$a_\sigma(\boldsymbol{p}_k, \omega) = \sum_{j=1}^{N_c} a_\sigma(\boldsymbol{r}_j, \omega) e^{i\boldsymbol{p}_k \cdot \boldsymbol{r}_j}, \tag{1.38}$$

with $j, k \in \{1, \ldots, N_c\}$. Further, the Dyson equation leads to a set of N_c momentum space self-energies

$$\Sigma_\sigma(\boldsymbol{p}_k, \omega) = a_\sigma(\boldsymbol{p}_k, \omega) - G_\sigma^{-1}(\boldsymbol{p}_k, \omega). \tag{1.39}$$

---

[3]It is convenient to take the average momentum of each region in the discrete Fourier transformation.

The momentum-dependent lattice Green function becomes

$$\bar{G}_\sigma(\boldsymbol{p}_k,\omega) = \frac{1}{V_{\mathrm{RBZ}}} \int_{\mathrm{RBZ}} (dp)^d \frac{1}{\omega + \mu - \varepsilon_{\boldsymbol{p}} - \Sigma_\sigma(\boldsymbol{p}_k,\omega)}, \tag{1.40}$$

where V_{RBZ} is the volume of the reduced Brillouin zone and the integration is performed over the RBZ which includes the momentum $\boldsymbol{p}_k$. The Dyson equation (1.39) leads to the new Weiss field in the momentum space

$$a_\sigma(\boldsymbol{p}_k,\omega) = \Sigma_\sigma(\boldsymbol{p}_k,\omega) + \bar{G}_\sigma^{-1}(\boldsymbol{p}_k,\omega), \tag{1.41}$$

and the inverse Fourier transformation gives the real-space Weiss field

$$a_\sigma(\boldsymbol{r}_j,\omega) = \frac{1}{N_c} \sum_{k=1}^{N_c} a_\sigma(\boldsymbol{p}_k,\omega) e^{-i\boldsymbol{p}_k \cdot \boldsymbol{r}_j}. \tag{1.42}$$

for the N_c-impurity problem.

Implementation

2-site DCA We consider a 2-site cluster as a part of the 2-dimensional quadratic lattice (Fig. 1.3 a)) with sites at $\boldsymbol{r}_0 = (0,0)^T$ and $\boldsymbol{r}_1 = (0,1)^T$. We choose the following vectors in the momentum space $\boldsymbol{p}_0 = (0,0)^T$ and $\boldsymbol{p}_1 = (\pi,\pi)^T$, because each of them lies in the middle of a reduced Brillouin zone. Equation (1.38) yields the Green function and the Weiss field in the momentum space

$$\begin{aligned} G_\sigma(\boldsymbol{p}_0,\omega) &= G_\sigma(\boldsymbol{r}_0,\omega) + G_\sigma(\boldsymbol{r}_1,\omega) \\ G_\sigma(\boldsymbol{p}_1,\omega) &= G_\sigma(\boldsymbol{r}_0,\omega) - G_\sigma(\boldsymbol{r}_1,\omega). \end{aligned} \tag{1.43}$$

Using the Weiss field from the last loop (or a inverse free Green function as an initial guess) we calculate the momentum space self-energy

$$\Sigma_\sigma(\boldsymbol{p}_i,\omega) = a_\sigma(\boldsymbol{p}_i,\omega) - G_\sigma^{-1}(\boldsymbol{p}_i,\omega), \tag{1.44}$$

with $i \in \{0,1\}$. Note, the self-energy is equal to $\Sigma_\sigma(\boldsymbol{p}_0,\omega)$ ($\Sigma_\sigma(\boldsymbol{p}_1,\omega)$) at every momentum in the RBZ, which contains momentum $\boldsymbol{p}_0$ ($\boldsymbol{p}_1$). The lattice Green function is obtained using

$$\bar{G}_\sigma(\boldsymbol{p}_i,\omega) = \frac{1}{\left(\sqrt{2}\pi\right)^2} \int_{\mathrm{RBZ}} (dp)^2 \frac{1}{\omega + \mu - \varepsilon_{\boldsymbol{p}} - \Sigma_\sigma(\boldsymbol{p}_i,\omega)}, \tag{1.45}$$

with $i \in \{0,1\}$. The replacement of the impurity Green function by the lattice Green function (1.45) in the Dyson equation (1.43) yields the new Weiss field. The inverse Fourier transformation

$$\begin{aligned} a_\sigma(\boldsymbol{r}_0,\omega) &= \frac{1}{2}(a_\sigma(\boldsymbol{p}_0,\omega) + a_\sigma(\boldsymbol{p}_1,\omega)) \\ a_\sigma(\boldsymbol{r}_1,\omega) &= \frac{1}{2}(a_\sigma(\boldsymbol{p}_0,\omega) - a_\sigma(\boldsymbol{p}_1,\omega)) \end{aligned} \tag{1.46}$$

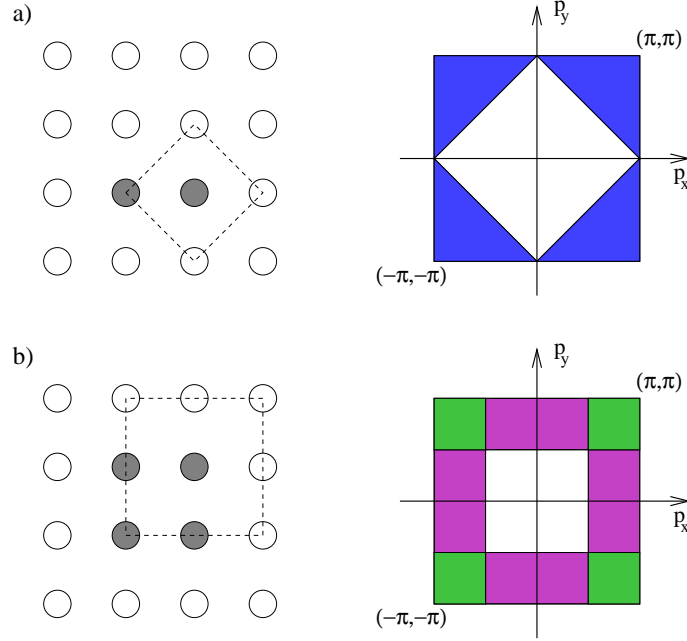leads to the new Weiss field for the two-impurity problem.

Figure 1.3: The 2- and 4-impurity cluster, with corresponding participation of the Brillouin zone. Each patter corresponds to one of the reduced Brillouin zones.

4-site DCA   The 4-site cluster and the participation of the Brillouin zone are shown in the Fig. 1.3 b). The approach in the 4-site case is analog. Using four real space vectors $\boldsymbol{r}_0 = (0,0)^T$, $\boldsymbol{r}_1 = (0,1)^T$, $\boldsymbol{r}_2 = (1,0)^T$ and $\boldsymbol{r}_3 = (1,1)^T$ and the momentum space vectors $\boldsymbol{p}_0 = (0,0)^T$, $\boldsymbol{p}_1 = (0,\pi)^T$, $\boldsymbol{p}_2 = (\pi,0)^T$ and $\boldsymbol{p}_3 = (\pi,\pi)^T$ we obtain the Green functions in the momentum space

$$
\begin{aligned}
G_\sigma(\boldsymbol{p}_0,\omega) &= G_\sigma(\boldsymbol{r}_0,\omega) + 2G_\sigma(\boldsymbol{r}_1,\omega) + G_\sigma(\boldsymbol{r}_2,\omega) \\
G_\sigma(\boldsymbol{p}_1,\omega) &= G_\sigma(\boldsymbol{p}_2,\omega) = G_\sigma(\boldsymbol{r}_0,\omega) - G_\sigma(\boldsymbol{r}_2,\omega) \\
G_\sigma(\boldsymbol{p}_3,\omega) &= G_\sigma(\boldsymbol{r}_0,\omega) - 2G_\sigma(\boldsymbol{r}_1,\omega) + G_\sigma(\boldsymbol{r}_2,\omega).
\end{aligned}
\tag{1.47}
$$

The equality $G_\sigma(\boldsymbol{r}_1,\omega) = G_\sigma(\boldsymbol{r}_2,\omega)$ follows from the x-y-symmetry in the quadratic lattice. The Dyson equation and the integrations over the corresponding reduced Brillouin zones give the lattice Green functions

$$
\bar{G}_\sigma(\boldsymbol{p}_i,\omega) = \frac{1}{\pi^2} \int_{\mathrm{RBZ}} (dp)^2 \frac{1}{\omega + \mu - \varepsilon_{\boldsymbol{p}} - \Sigma_\sigma(\boldsymbol{p}_i,\omega)},
\tag{1.48}
$$

where $i \in \{0, 1, 2, 3\}$. The Dyson equation with upper Green functions and the following inverse Fourier transformation

$$
\begin{aligned}
a_\sigma(\boldsymbol{r}_0, \omega) &= \frac{1}{4} \left(a_\sigma(\boldsymbol{p}_0, \omega) + 2a_\sigma(\boldsymbol{p}_1, \omega) + a_\sigma(\boldsymbol{p}_3, \omega) \right) \\
a_\sigma(\boldsymbol{r}_1, \omega) &= a_\sigma(\boldsymbol{r}_2, \omega) = \frac{1}{4} \left(a_\sigma(\boldsymbol{p}_0, \omega) - a_\sigma(\boldsymbol{p}_3, \omega) \right) \\
a_\sigma(\boldsymbol{r}_3, \omega) &= \frac{1}{4} \left(a_\sigma(\boldsymbol{p}_0, \omega) - 2a_\sigma(\boldsymbol{p}_1, \omega) + a_\sigma(\boldsymbol{p}_3, \omega) \right)
\end{aligned}
\tag{1.49}
$$

lead to the new Weiss field.

The energy (A.19) can be obtained analog to the calculation of the Green function, one should be careful with the integration over different RBZ's.

The equations, considered in this section, are specific to the paramagnetic case. The difference to the antiferromagnetic order is the same like in the section 1.2.1. The scalar functions in the equations (1.43) – (1.49) will be substituted by 2×2 matrices.

The advantage of the DCA is the momentum dependency of the self-energy, what was neglected in the original dynamical mean field theory. The disadvantages are the self-energy discontinuity in momentum space and the canonization between the cluster and the considering lattice. Moreover the expansion of the cluster is not straightforward because of the splitting of the Brillouin zone in N_c RBZ's.

1.3 Numerical Techniques

1.3.1 Semiclassical Approximation

The semiclassical approximation (SCA) was formulated by Hasegawa [19, 20] in 1980 and is based on the continuous Hubbard-Stratonovich transformation [13, 21]. Hasegawa used this method to study a "single-site spin fluctuation theory" which can be viewed as a simplification of the modern dynamical-mean-field theory. Semiclassical methods were also used in the works by Blawid and Millis [22] and by Pankov, Kotliar and Motome [23] in the study of models of electrons coupled to the large-mass oscillations.

As shown below SCA and QMC results are in good agreement, moreover, the semiclassical approximation is very cheap in matters of computational time. In fact, the SCA is approximately two decades faster than QMC for single-impurity models at large U. Therefore most of the computations in this chapter were performed using SCA.

Formalism

We start the formalism with a partition function, which is given as

$$
Z = \int \mathcal{D} \left[c^\dagger c \right] e^{-S_{\text{eff}}},
\tag{1.50}
$$

where the effective action is

$$S_{\text{eff}} = -\int_0^\beta d\tau \int_0^\beta d\tau' \, c^\dagger(\tau)\hat{a}(\tau,\tau')c(\tau') + \int_0^\beta d\tau \, U n_\uparrow(\tau)n_\downarrow(\tau). \qquad (1.51)$$

The Grassmann variables $c^\dagger = \left(c_\uparrow^\dagger, c_\downarrow^\dagger\right)^T$ and $c = (c_\uparrow, c_\downarrow)^T$ correspond to the fermionic creation and annihilation operators, and n_σ to the particle number operator $n_\sigma = c_\sigma^\dagger c_\sigma$, $\beta = T^{-1}$. $\hat{a} = \text{diag}(a_\uparrow, a_\downarrow)$ is the Weiss field which implies the effect of the environment on the impurity. The substitution

$$n_\uparrow n_\downarrow = \frac{1}{4}\left((n_\uparrow + n_\downarrow)^2 - (n_\uparrow - n_\downarrow)^2\right) = \frac{1}{4}(N^2 - M^2), \qquad (1.52)$$

where N is the particle number and M is the magnetization, decouples the most problematic part of the action:

$$S_{\text{eff}} = -\int_0^\beta d\tau \int_0^\beta d\tau' \, c^\dagger(\tau)\hat{a}(\tau,\tau')c(\tau') + \frac{U}{4}\int_0^\beta d\tau \, \left(N^2(\tau) - M^2(\tau)\right). \qquad (1.53)$$

We substitute $N(\tau)$ by $\langle N \rangle$ in the present approximation, whereas $\langle N \rangle = 1$ at the half filling. In other words, we neglect the real charge fluctuations.

$$Z = \int \mathcal{D}\left[c^\dagger c\right] \, e^{\int_0^\beta d\tau \int_0^\beta d\tau' c^\dagger(\tau)\hat{a}(\tau,\tau')c(\tau') + \frac{U}{4}\int_0^\beta d\tau \, M^2(\tau)} e^{-\frac{\beta U}{4}}, \qquad (1.54)$$

where term $\beta U/4$ shifts the energy at $-U/4$ and plays the same role like a chemical potential. For simplicity we do not write this constant term in the following derivation, because it does not affect the Green functions we are interested in. Using a Hubbard-Stratonovich transformation [21]

$$\int_{-\infty}^{\infty} dx \, e^{-\pi x^2 + 2\sqrt{\pi}Ax} = e^{A^2}, \qquad (1.55)$$

where A is a number and x is a scalar auxiliary field, we obtain a "new" partition function

$$Z = \int \mathcal{D}\left[c^\dagger c\right] \mathcal{D}[\varphi] \, e^{\int_0^\beta d\tau \int_0^\beta d\tau' \, c^\dagger(\tau)\hat{a}(\tau,\tau')c(\tau') - \int_0^\beta d\tau \left(\frac{1}{4U}\varphi^2(\tau) - \frac{1}{2}\varphi(\tau)M(\tau)\right)}, \qquad (1.56)$$

where rescaling $\varphi = \sqrt{\pi}x$ changes Z up to a constant. In general, the semiclassical field φ is a function of the imaginary time τ, but in this approximation we assume it to be τ-independent (semiclassical approximation)

$$Z = \int \mathcal{D}\left[c^\dagger c\right] \int_{-\infty}^{\infty} d\varphi \, e^{\int_0^\beta d\tau \int_0^\beta d\tau' \, c^\dagger(\tau)\hat{a}(\tau,\tau')c(\tau') - \int_0^\beta d\tau \left(\frac{1}{4U}\varphi^2 - \frac{1}{2}\varphi M(\tau)\right)}$$

$$= \int \mathcal{D}\left[c^\dagger c\right] \int_{-\infty}^{\infty} d\varphi \, e^{-\frac{\beta}{4U}\varphi^2 + \int_0^\beta d\tau \int_0^\beta d\tau' \, c^\dagger(\tau)\left(\hat{a}(\tau,\tau') + \frac{1}{2}\varphi\hat{\sigma}_z\delta(\tau-\tau')\right)c_\sigma(\tau')}. \qquad (1.57)$$

We have used $M(\tau) = \int_0^\beta d\tau'\, c^\dagger(\tau)\hat{\sigma}_z \delta(\tau - \tau')c(\tau')$ in the second line of equation (1.57), where $\hat{\sigma}_z$ is the third Pauli matrix. After a Fourier transformation, we perform a Grassmann integration[4]

$$
\begin{aligned}
Z &= \int \mathcal{D}\left[\tilde{c}^\dagger \tilde{c}\right] \left|\frac{\partial(\tilde{c}^\dagger, \tilde{c})}{\partial(c^\dagger, c)}\right| \int_{-\infty}^\infty d\varphi\, e^{-\frac{\beta}{4U}\varphi^2 + \beta \sum_{\omega_n} \tilde{c}^\dagger(\omega_n)\left(\hat{a}(\omega_n) + \frac{1}{2}\varphi\hat{\sigma}_z\right)\tilde{c}(\omega_n)} \\
&= \int_{-\infty}^\infty d\varphi\, e^{-\frac{\beta}{4U}\varphi^2} \prod_{\omega_n} \det\left[-\beta\left(\hat{a}(\omega_n) + \frac{1}{2}\varphi\hat{\sigma}_z\right)\right] \\
&= \int_{-\infty}^\infty d\varphi\, e^{-\frac{1}{4}\frac{\beta}{U}\varphi^2 + \sum_{\omega_n} \ln\det\left[-\beta\left(\hat{a}(\omega_n) + \frac{1}{2}\varphi\hat{\sigma}_z\right)\right]},
\end{aligned}
\tag{1.58}
$$

where c and $c^\dagger$ are functions of τ and $\tilde{c}$ and $\tilde{c}^\dagger$ are functions of the fermionic Matsubara frequencies ω_n; $\left|\frac{\partial(\tilde{c}^\dagger, \tilde{c})}{\partial(c^\dagger, c)}\right| = 1$ because of the isometry of the Fourier transformation.

In general a cluster consists of N sites, therefore the semiclassical field becomes a vector of N fields $\boldsymbol{\varphi} = (\varphi_1, \dots, \varphi_N)^T$, where each field φ_i acts on the corresponding cluster site i. Thus the general partition function is

$$
Z = \int_{-\infty}^\infty d\varphi_1 \dots d\varphi_N\, e^{-\beta V(\boldsymbol{\varphi})},
\tag{1.59}
$$

with

$$
V(\boldsymbol{\varphi}) = \frac{1}{4U}|\boldsymbol{\varphi}|^2 - T\sum_{\omega_n} \ln\det\left[-\beta\left(\hat{a}(\omega_n) + \hat{\Lambda}(\boldsymbol{\varphi}, \boldsymbol{s})\right)\right].
\tag{1.60}
$$

Note, $\hat{a}$ and $\hat{\Lambda}(\boldsymbol{\varphi}, \boldsymbol{s}) = \mathrm{diag}\left(s_1\varphi_1\hat{\sigma}_z, \dots, s_N\varphi_N\hat{\sigma}_z\right)$ are $2N \times 2N$ matrices, where $s_i = \pm 1/2$, with $i \in \{1, \dots, N\}$, corresponds to the z-component of the spin on the ith site of the cluster. Because of the symmetry of the integration we substitute $s_i\varphi_i$ by ϕ_i and obtain

$$
\begin{aligned}
Z &= 2^N \int_{-\infty}^\infty d\phi_1 \dots d\phi_N\, e^{-\beta V(\boldsymbol{\phi})} \\
V(\boldsymbol{\phi}) &= \frac{1}{U}|\boldsymbol{\phi}|^2 - T\sum_{\omega_n} \ln\det\left[-\beta\left(\hat{a}(\omega_n) + \hat{\Lambda}(\boldsymbol{\phi})\right)\right],
\end{aligned}
\tag{1.61}
$$

with $\hat{\Lambda}(\boldsymbol{\phi}) = \mathrm{diag}\left(\phi_1\hat{\sigma}_z, \dots, \phi_N\hat{\sigma}_z\right)$. Furthermore $\hat{a}$ as well as $\hat{\Lambda}(\boldsymbol{\phi})$ is a $N \times N$ matrix of the *diagonal* 2×2 matrices. Therefore some permutations of the rows and the columns lead to a diagonal matrix, which looks like $\mathrm{diag}\left(\hat{A}_\uparrow, \hat{A}_\downarrow\right)$, where $\hat{A}_\uparrow$ $\left(\hat{A}_\downarrow\right)$ is a $N \times N$ matrix and contains all entries of the initial $2N \times 2N$ matrix with index $\uparrow$ ($\downarrow$). Thus the potential can be rewritten as

$$
V(\boldsymbol{\phi}) = \frac{1}{U}|\boldsymbol{\phi}|^2 - T\sum_{\omega_n, \sigma=\uparrow,\downarrow} \ln\det\left[-\beta\left(\hat{a}_\sigma(\omega_n) + \hat{\Lambda}_\sigma(\boldsymbol{\phi})\right)\right],
\tag{1.62}
$$

---

[4] $\int 1\, dc^\dagger\, dc = 0$, $\int a c^\dagger c\, dc^\dagger\, dc = -a \int c^\dagger\, dc^\dagger = -a$, where a is a complex number and c and $c^\dagger$ are Grassmann variables.
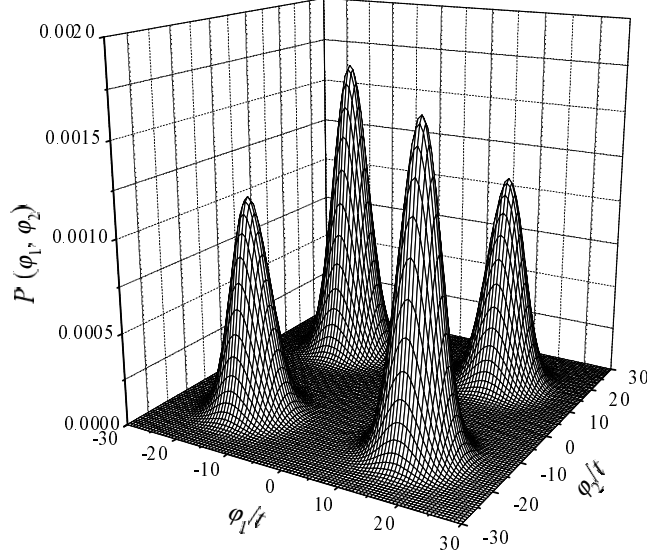
Figure 1.4: The probability $P(\varphi_1, \varphi_2) = \exp\{-\beta V(\varphi_1, \varphi_2)\}/Z$ for 2-site cluster in the FI method for the Hubbard model on a square lattice at $U/t = 16, T/t = 0.3$ [24]. The fact, that the peaks at $\boldsymbol{\varphi}/t = (\pm 16, \mp 16)^T$ greater than the peaks at $\boldsymbol{\varphi}/t \approx (\pm 16, \pm 16)^T$ shows antiferromagnetic correlation. Note, the antiferromagnetism was suppressed; without the suppression we get a dominant peak at $\boldsymbol{\varphi}/t \approx (-16, 16)^T$ or at $\boldsymbol{\varphi}/t \approx (16, -16)^T$

where $\hat{\Lambda}_\sigma(\boldsymbol{\phi}) = \mathrm{diag}(\phi_1, \ldots, \phi_N)\,\sigma_z$, with $\sigma_z = 1$ (-1), if $\sigma = \uparrow (\downarrow)$.

According to equation (1.19) the impurity Green function becomes

$$\hat{G}_\sigma(\omega_n) = \frac{2^N}{ZN} \int_{-\infty}^{\infty} d\phi_1 \ldots d\phi_N\, e^{-\beta V(\boldsymbol{\phi})} \left(\hat{a}_\sigma(\omega_n) + \hat{\Lambda}_\sigma(\boldsymbol{\phi}) \right)^{-1}. \qquad (1.63)$$

In order to reduce the computational time in the large-U regime, we assume that the barriers among the minima of the potential $V(\boldsymbol{\phi})$ are very high. In fact, Figure 1.4 shows the probability distribution as a function of $\boldsymbol{\varphi}$ for a two-site cluster at large interaction ($U/t = 16$). One can clearly see that the probability is strongly centered at the minima of the potential. On this account we substitute the integration over $\phi_1, \ldots, \phi_N$ by the sum over all minima [34]

$$Z = \frac{1}{N_{\min}} \sum_{i=1}^{N_{\min}} e^{-\beta V(\boldsymbol{\phi}_i)}, \qquad (1.64)$$

where $N_{\min}$ is the number of minima of the potential $V(\boldsymbol{\phi})$. Also the impurity Green function in the strong interaction regime becomes

$$\hat{G}_\sigma(\omega_n) = \frac{1}{ZNN_{\min}} \sum_{i=1}^{N_{\min}} e^{-\beta V(\boldsymbol{\phi}_i)} \left(\hat{a}_\sigma(\omega_n) + \hat{\Lambda}_\sigma(\boldsymbol{\phi}) \right)^{-1}. \qquad (1.65)$$

The minima of the potential could be found using a Newton-Raphson algorithm [27].

Implementation

Two-site cluster   The two site cluster consideration requires a Weiss field that consists of two components $a_0(\omega_n)$ and $a_1(\omega_n)$. For simplicity of notation we will not write the ω_n-dependency of the Weiss field explicitly. The Weiss field grows to the matrix

$$\hat{a}_\sigma = \begin{pmatrix} a_{0\sigma} & 0 \\ 0 & a_{0\bar{\sigma}} \end{pmatrix} + \begin{pmatrix} 0 & a_{1\sigma} \\ a_{1\sigma} & 0 \end{pmatrix}, \tag{1.66}$$

where we implied $a_{1\uparrow} = a_{1\downarrow}$. We consider antiferromagnetic order because the corresponding equations are correct in the paramagnetic case too. Using the semiclassical field $\boldsymbol{\phi} = (\phi_1, \phi_2)^T$, we obtain a two-site cluster potential

$$
\begin{aligned}
V(\boldsymbol{\phi}) &= \frac{\phi_1^2 + \phi_2^2}{U} - T \sum_{\omega_n, \sigma} \ln \det \left[-\beta \begin{pmatrix} a_{0\sigma} + \phi_1\sigma_z & a_{1\sigma} \\ a_{1\sigma} & a_{0\bar{\sigma}} + \phi_2\sigma_z \end{pmatrix} \right] \\
&= \frac{\phi_1^2 + \phi_2^2}{U} - T \sum_{\omega_n, \sigma} \ln \mathrm{Det}_\sigma,
\end{aligned}
\tag{1.67}
$$

where

$$\mathrm{Det}_\sigma \equiv \mathrm{Det}_\sigma(\omega_n) = \beta^2 \left[(a_{0\sigma} + \phi_1\sigma_z)(a_{0\bar{\sigma}} + \phi_2\sigma_z) - a_{1\sigma}^2 \right]. \tag{1.68}$$

According to equations (1.59) and (1.63), we calculate the partition sum and the Green functions in the 2-site cluster

$$
\begin{aligned}
Z &= 4 \int_{-\infty}^{\infty} d\phi_1 d\phi_2 \, e^{-\beta V(\boldsymbol{\phi})} \\
G_{0\sigma}(\omega_n) &= \frac{2}{Z} \int_{-\infty}^{\infty} d\phi_1 d\phi_2 \, e^{-\beta V(\boldsymbol{\phi})} \beta^2 \left(\frac{a_{0\bar{\sigma}} + \phi_2\sigma_z}{\mathrm{Det}_\sigma} + \frac{a_{0\bar{\sigma}} + \phi_1\bar{\sigma}_z}{Det_{\bar{\sigma}}} \right) \\
G_{1\sigma}(\omega_n) &= \frac{2}{Z} \int_{-\infty}^{\infty} d\phi_1 d\phi_2 \, e^{-\beta V(\boldsymbol{\phi})} \beta^2 \frac{-2a_{1\sigma}}{\mathrm{Det}_\sigma},
\end{aligned}
\tag{1.69}
$$

thus having solved the two-impurity problem. In order to complete the picture we give the definition of the spin-spin correlation in current presentation

$$\langle \sigma_1 \sigma_2 \rangle = \frac{16}{Z} \int_{-\infty}^{\infty} d\phi_1 d\phi_2 \, \frac{\phi_1 \phi_2}{|\phi_1 \phi_2|} e^{-\beta V(\boldsymbol{\phi})}, \tag{1.70}$$

do not forget $\phi_i = s_i \varphi_i$. An *important* hint [24] for the potential calculation: The sum over Matsubara frequencies in the potential has a divergent part, namely the Weiss field. Therefore it is not possible to calculate this sum numerically. For this reason we compute the sum

$$\sum_{\omega_n, \sigma} \ln \det \left[\begin{pmatrix} 1 & 0 \\ 0 & 1 \end{pmatrix} + \begin{pmatrix} a_{0\sigma} & a_{1\sigma} \\ a_{1\sigma} & a_{0\bar{\sigma}} \end{pmatrix}^{-1} \begin{pmatrix} \phi_1 & 0 \\ 0 & \phi_2 \end{pmatrix} \sigma_z \right]. \tag{1.71}$$
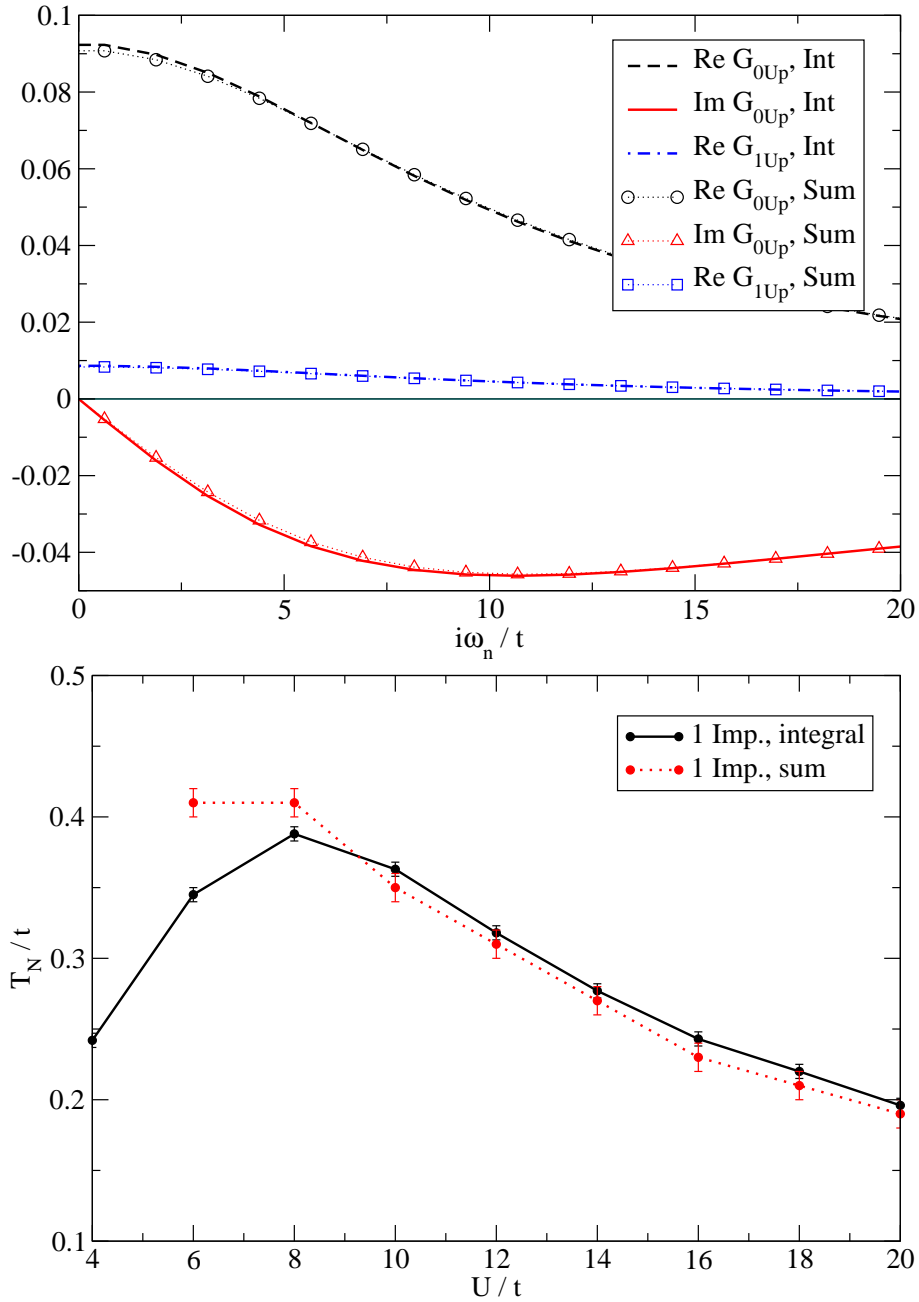
Figure 1.5: Upper panel: The impurity Green function computed using SCA at $U/t = 20$, $T/t = 0.2$, at half filling and within the antiferromagnetic regime. The dotted curve corresponds to the approximated SCA, where the integration is substituted by the sum over all minima of the potential. Lower panel: the Néel temperature of the single-site model computed using sum-SCA and integral-SCA.

The remaining ϕ-independent part of the sum cancels in the course of the derivation of the Green function (1.19). Furthermore the calculation of the potential should be performed very carefully, which is necessary for the accuracy of calculated quantities. For this reason we give the high frequency correction in appendix A.4.

As mentioned before, in order to get quickly results at large interaction value one can use the Newton-Raphson method to find the minima of the potential. In two site case, one should solve the system of two equations $\frac{\delta V(\phi)}{\delta \phi_j} = 0$, $j \in \{1, 2\}$. Explicitly, we are looking for 2^2 values of the semiclassical fields, $\phi_i = (\phi_{i1}, \phi_{i2})^T$, $i \in \{1, 2, 3, 4\}$, which solve the following system

$$\begin{cases} \phi_1 = \dfrac{U}{2T} \sum_{\omega_n, \sigma} \dfrac{a_{0\sigma}\sigma_z + \phi_2}{\mathrm{Det}_\sigma} \\ \phi_2 = \dfrac{U}{2T} \sum_{\omega_n, \sigma} \dfrac{a_{0\sigma}\sigma_z + \phi_1}{\mathrm{Det}_\sigma}. \end{cases} \tag{1.72}$$

Using the results given above we replace the integration $4 \int_{-\infty}^{\infty} d\phi_1 d\phi_2$ in equations (1.69) by the sum $\frac{1}{4} \sum_{i=1}^{4}$. Figure 1.5 (upper panel) demonstrates the impurity Green function calculated using integral- and sum-SCA at $U/t = 20$ and $T/t = 0.2$, with the same anti-ferromagnetic input-Weiss field after first loop. The largest deviation of the approximated result is around $\omega_n/t \approx 0$ and lies below the 3% mark. On the lower panel one can see the Néel temperature computed using a single impurity integral- and sum-SCA. We observe reasonable consistence of both results at $U/t > 8$, the deviation is smaller than 5%. The decreasing interaction leads to the get-together of the peaks and to the decrease of the potential walls among the minima, which causes a significant increase of the computational time in the Newton-Raphson method because the minimization process often gets stuck in the saddle points. Therefore we made use of the sum-SCA for the large-U calculations, in particular in the 4-site cluster calculations.

Four-site cluster Next we consider a four-site cluster. The Weiss field consists of 5 different components ($a_{1\sigma} = a_{1\bar{\sigma}}$) and becomes a 4×4 matrix

$$\hat{a}_\sigma = \begin{pmatrix} a_{0\sigma} & 0 & 0 & 0 \\ 0 & a_{0\bar{\sigma}} & 0 & 0 \\ 0 & 0 & a_{0\sigma} & 0 \\ 0 & 0 & 0 & a_{0\bar{\sigma}} \end{pmatrix} + \frac{1}{\sqrt{2}} \begin{pmatrix} 0 & a_{1\sigma} & 0 & a_{1\sigma} \\ a_{1\sigma} & 0 & a_{1\sigma} & 0 \\ 0 & a_{1\sigma} & 0 & a_{1\sigma} \\ a_{1\sigma} & 0 & a_{1\sigma} & 0 \end{pmatrix} + \begin{pmatrix} 0 & 0 & a_{2\sigma} & 0 \\ 0 & 0 & 0 & a_{2\bar{\sigma}} \\ a_{2\sigma} & 0 & 0 & 0 \\ 0 & a_{2\bar{\sigma}} & 0 & 0 \end{pmatrix}, \tag{1.73}$$

19

where the second matrix is normalized by the factor $\frac{1}{\sqrt{2}}$ [5]. According to equation (1.60) we calculate the semiclassical potential for the 4-site cluster

$$
\begin{aligned}
V(\boldsymbol{\phi}) &= \frac{|\boldsymbol{\phi}|^2}{U} - T \sum_{\omega_n,\sigma} \ln \det \left[-\beta \begin{pmatrix} a_{0\sigma} + \phi_1\sigma_z & \frac{a_{1\sigma}}{\sqrt{2}} & a_{2\sigma} & \frac{a_{1\sigma}}{\sqrt{2}} \\ \frac{a_{1\sigma}}{\sqrt{2}} & a_{0\bar{\sigma}} + \phi_2\sigma_z & \frac{a_{1\sigma}}{\sqrt{2}} & a_{2\bar{\sigma}} \\ a_{2\sigma} & \frac{a_{1\sigma}}{\sqrt{2}} & a_{0\sigma} + \phi_3\sigma_z & \frac{a_{1\sigma}}{\sqrt{2}} \\ \frac{a_{1\sigma}}{\sqrt{2}} & a_{2\bar{\sigma}} & \frac{a_{1\sigma}}{\sqrt{2}} & a_{0\bar{\sigma}} + \phi_4\sigma_z \end{pmatrix} \right] \\
&= \frac{|\boldsymbol{\phi}|^2}{U} - T \sum_{\omega_n,\sigma} \ln \mathrm{Det}_\sigma,
\end{aligned}
$$

(1.74)

with

$$
\begin{aligned}
\mathrm{Det}_\sigma = \beta^4 \Bigg[& (a_{0\sigma} + \phi_1\sigma_z)(a_{0\bar{\sigma}} + \phi_2\sigma_z)(a_{0\sigma} + \phi_3\sigma_z)(a_{0\bar{\sigma}} + \phi_4\sigma_z) \\
& - \frac{a_{1\sigma}^2}{2} \{ (2a_{0\sigma} + (\phi_1 + \phi_3)\sigma_z)(2a_{0\bar{\sigma}} + (\phi_2 + \phi_4)\sigma_z) \\
& + 2a_{2\bar{\sigma}}(2a_{0\sigma} + (\phi_1 + \phi_3)\sigma_z) + 2a_{2\sigma}(2a_{0\bar{\sigma}} + (\phi_2 + \phi_4)\sigma_z) \} \\
& - 2a_{1\sigma}^2 a_{2\sigma} a_{2\bar{\sigma}} + a_{2\sigma}^2 a_{2\bar{\sigma}}^2 - a_{2\sigma}^2 (a_{0\bar{\sigma}} + \phi_2\sigma_z)(a_{0\bar{\sigma}} + \phi_4\sigma_z) \\
& \qquad\qquad\qquad\qquad - a_{2\bar{\sigma}}^2 (a_{0\sigma} + \phi_1\sigma_z)(a_{0\sigma} + \phi_3\sigma_z) \Bigg].
\end{aligned}
$$

(1.75)

Note, the ω_n-sum has a divergent term $\hat{a}$, therefore we perform the sum using the same trick as in the 2-site case. The ϕ-integration in the partition function becomes four-dimensional

$$
Z = 16 \int_{-\infty}^{\infty} d\phi_1 \ldots d\phi_4 \, e^{-\beta V(\boldsymbol{\phi})},
$$

(1.76)

and the derivative of the logarithm of the partition function according to equation (1.19) gives following Green functions

$$
\begin{aligned}
G_{0\sigma}(\omega_n) = \frac{4}{Z} \int_{-\infty}^{\infty} & d\phi_1 \ldots d\phi_4 \, e^{-\beta V(\boldsymbol{\phi})} \beta^4 \times \\
\times \Bigg[& \frac{1}{\mathrm{Det}_\sigma} \{ ((a_{0\bar{\sigma}} + \phi_2\sigma_z)(a_{0\bar{\sigma}} + \phi_4\sigma_z) - a_{2\bar{\sigma}}^2)(2a_{0\sigma} + (\phi_1 + \phi_3)\sigma_z) \\
& \qquad\qquad\qquad + a_{1\sigma}^2 (2a_{2\bar{\sigma}} - 2a_{0\bar{\sigma}} - (\phi_2 + \phi_4)\sigma_z) \} \\
& + \frac{1}{\mathrm{Det}_{\bar{\sigma}}} \{ ((a_{0\bar{\sigma}} + \phi_1\bar{\sigma}_z)(a_{0\bar{\sigma}} + \phi_3\bar{\sigma}_z) - a_{2\bar{\sigma}}^2)(2a_{0\sigma} + (\phi_2 + \phi_4)\bar{\sigma}_z) \\
& \qquad\qquad\qquad + a_{1\sigma}^2 (2a_{2\bar{\sigma}} - 2a_{0\bar{\sigma}} - (\phi_1 + \phi_3)\bar{\sigma}_z) \} \Bigg]
\end{aligned}
$$

---

[5] All matrices have to satisfy equation (1.17)

$$G_{1\sigma}(\omega_n) = \frac{4}{16Z} \int_{-\infty}^{\infty} d\phi_1 \ldots d\phi_4 \, e^{-\beta V(\boldsymbol{\phi})} \beta^4 \times$$

$$\times \frac{1}{\mathrm{Det}_\sigma} \left\{ -a_{1\sigma} \left(2a_{0\bar\sigma} + (\phi_1 + \phi_3)\sigma_z\right) \left(2a_{0\bar\sigma} + (\phi_2 + \phi_4)\sigma_z\right) \right.$$

$$\left. + 2a_{1\sigma} \left(a_{2\sigma} \left(2a_{0\bar\sigma} + (\phi_2 + \phi_4)\sigma_z\right) + a_{2\bar\sigma} \left(2a_{0\sigma} + (\phi_1 + \phi_3)\sigma_z\right)\right) - 4a_{1\sigma}a_{2\sigma}a_{2\bar\sigma} \right\}$$

$$G_{2\sigma}(\omega_n) = \frac{4}{Z} \int_{-\infty}^{\infty} d\phi_1 \ldots d\phi_4 \, e^{-\beta V(\boldsymbol{\phi})} \beta^4 \left[\frac{1}{\mathrm{Det}_\sigma} \left\{ a_{1\sigma}^2 \left(2a_{0\bar\sigma} + (\phi_2 + \phi_4)\sigma_z\right) \right. \right. \tag{1.77}$$

$$\left. -2a_{2\bar\sigma}(a_{1\sigma}^2 - a_{2\sigma}a_{2\bar\sigma}) - 2a_{2\sigma} \left(a_{0\bar\sigma} + \phi_2\sigma_z\right) \left(a_{0\bar\sigma} + \phi_4\sigma_z\right) \right\}$$

$$+ \frac{1}{Det_{\bar\sigma}} \left\{ a_{1\sigma}^2 \left(2a_{0\bar\sigma} + (\phi_1 + \phi_3)\bar\sigma_z\right) - 2a_{2\bar\sigma}(a_{1\sigma}^2 - a_{2\sigma}a_{2\bar\sigma}) \right.$$

$$\left. \left. -2a_{2\sigma} \left(a_{0\bar\sigma} + \phi_1\bar\sigma_z\right) \left(a_{0\bar\sigma} + \phi_3\bar\sigma_z\right) \right\} \right].$$

The four-dimensional integration takes significantly more time than the two-dimensional one. The difference between the integral- and the sum-SCA in the 4-site cluster case at large Coulomb repulsion is smaller then in the 2-site case, therefore we used the sum-approach in large-U regime. The potential of the 4-site cluster is a function of the semiclassical field $\boldsymbol{\phi} = (\phi_1, \phi_2, \phi_3, \phi_4)^T$ and has 16 minima in the large interaction region. Now the procedure is analog to the treatment of the 2-site cluster potential. We are looking for solutions of the system of non-linear equations $\frac{\delta V(\boldsymbol{\phi})}{\delta \phi_j} = 0$, $j \in \{1,2,3,4\}$ using the Newton-Raphson method. There is a system of 4 equations to solve:

$$\begin{cases} \varphi_1 = U\beta^3 \sum_{\omega_n,\sigma} \frac{\sigma_z}{\mathrm{Det}_\sigma} \left\{ \left(a_{0\bar\sigma} + \phi_2\sigma_z\right) \left(a_{0\sigma} + \phi_3\sigma_z\right) \left(a_{0\bar\sigma} + \phi_4\sigma_z\right) \right. \\ \qquad \left. + a_{1\sigma}^2 \left(a_{2\bar\sigma} - a_{0\bar\sigma} - \frac{1}{2}(\phi_2 + \phi_4)\sigma_z\right) - a_{2\bar\sigma}^2 \left(a_{0\sigma} + \phi_3\sigma_z\right) \right\} \\ \varphi_2 = U\beta^3 \sum_{\omega_n,\sigma} \frac{\sigma_z}{\mathrm{Det}_\sigma} \left\{ \left(a_{0\sigma} + \phi_1\sigma_z\right) \left(a_{0\sigma} + \phi_3\sigma_z\right) \left(a_{0\bar\sigma} + \phi_4\sigma_z\right) \right. \\ \qquad \left. + a_{1\sigma}^2 \left(a_{2\sigma} - a_{0\sigma} - \frac{1}{2}(\phi_1 + \phi_3)\sigma_z\right) - a_{2\sigma}^2 \left(a_{0\bar\sigma} + \phi_4\sigma_z\right) \right\} \\ \varphi_3 = U\beta^3 \sum_{\omega_n,\sigma} \frac{\sigma_z}{\mathrm{Det}_\sigma} \left\{ \left(a_{0\sigma} + \phi_1\sigma_z\right) \left(a_{0\bar\sigma} + \phi_2\sigma_z\right) \left(a_{0\bar\sigma} + \phi_4\sigma_z\right) \right. \\ \qquad \left. + a_{1\sigma}^2 \left(a_{2\bar\sigma} - a_{0\bar\sigma} - \frac{1}{2}(\phi_2 + \phi_4)\sigma_z\right) - a_{2\bar\sigma}^2 \left(a_{0\sigma} + \phi_1\sigma_z\right) \right\} \\ \varphi_4 = U\beta^3 \sum_{\omega_n,\sigma} \frac{\sigma_z}{\mathrm{Det}_\sigma} \left\{ \left(a_{0\sigma} + \phi_1\sigma_z\right) \left(a_{0\bar\sigma} + \phi_2\sigma_z\right) \left(a_{0\sigma} + \phi_3\sigma_z\right) \right. \\ \qquad \left. + a_{1\sigma}^2 \left(a_{2\sigma} - a_{0\sigma} - \frac{1}{2}(\phi_1 + \phi_3)\sigma_z\right) - a_{2\sigma}^2 \left(a_{0\bar\sigma} + \phi_2\sigma_z\right) \right\}. \end{cases} \tag{1.78}$$

Then we can substitute the 4-dimensional integration by the sum $\frac{1}{16}\sum_{i=1}^{16}$ in equations (1.76) and (1.77) at large interaction. Sadly this trick works out at $U/t > 10$ only, therefore we have to use the integral-SCA in the low-U regime.

It was found that this version of the semiclassical approximation is in agreement with a well known Quantum Monte-Carlo Algorithm (see next subsection) but takes significantly less computational time (see section 1.8).

1.3.2 Quantum Monte Carlo Method

The Quantum Monte Carlo method (QMC) is one of the most powerful methods in statistical physics. The most successful version of the QMC to solve a general impurity problem was introduced by Hirsch and Fye in 1986 [25]. The procedure is based on the discretization of the effective action and on the decoupling of the interaction using the discrete Hubbard-Stratonovich transformation [13]. The local Green function is determined via a Markov process.

Formalism

Again we start with the partition function (1.50) and discretize the impurity model effective action

$$
\begin{aligned}
S_{\text{eff}} &= \sum_\sigma \int_0^\beta d\tau d\tau'\, c_\sigma^\dagger(\tau) a_\sigma(\tau, \tau') c_\sigma(\tau') - U \int_0^\beta d\tau\, n_\uparrow(\tau) n_\downarrow(\tau) \\
&\approx (\Delta\tau)^2 \sum_{l,l',\sigma} c_\sigma^\dagger(\tau_l) a_\sigma(\tau_l, \tau_{l'}) c_\sigma(\tau_{l'}) - \Delta\tau U \sum_l n_\uparrow(\tau_l) n_\downarrow(\tau_l),
\end{aligned}
\tag{1.79}
$$

where $l, l' \in \{1, \ldots, L\}$, $\Delta\tau = \beta/L$ and $\tau_l = (l-1)\Delta\tau$. The only problematic part of the effective action is the interaction term $U n_\uparrow(\tau_l) n_\downarrow(\tau_l)$, which includes a product of four operators. The problem was solved using the discrete Hubbard-Stratonovich transformation (HST)

$$
e^{-U\Delta\tau n_\uparrow n_\downarrow} = \frac{1}{2} \sum_{s=\pm 1} e^{\lambda s(n_\uparrow - n_\downarrow) - \frac{1}{2}U\Delta\tau(n_\uparrow + n_\downarrow)},
\tag{1.80}
$$

where $\cosh\lambda = e^{\frac{1}{2}U\Delta\tau}$, s (Ising spin) is the component of the discrete auxiliary field. The discrete HST includs the fermionic equation

$$
n_\uparrow n_\downarrow = -\frac{1}{2}(n_\uparrow - n_\downarrow)^2 + \frac{1}{2}(n_\uparrow + n_\downarrow).
\tag{1.81}
$$

So the product of two quadratic terms is decoupled and the meaning of the Hubbard-Stratonovich transformation is the following: the HST replaces the system of interacting particles by a system of noninteracting particles in a fluctuating real field, which couples to the z-component of the spin[6]. Performing the HST (1.80) at every time slice τ_l in the

---

[6]The present transformation works for fermionic systems only.

effective action, we obtain the "new" partition function

$$Z = \frac{1}{2^L} \sum_{\boldsymbol{s}} \int \mathcal{D}\left[c^\dagger c\right] e^{(\Delta\tau)^2 \sum_{l,l',\sigma} c_\sigma^\dagger(\tau_l) a_\sigma(\tau_l, \tau_{l'}) c_\sigma(\tau_{l'}) + \Delta\tau \sum_l \lambda s_l (n_\uparrow(\tau_l) - n_\downarrow(\tau_l))}, \tag{1.82}$$

where $\sum_{\boldsymbol{s}}$ is the sum over all 2^L possible configurations $\boldsymbol{s} = (s_1, \dots, s_L)$ of L Ising spins; the term $-\frac{1}{2}U\Delta\tau(n_\uparrow + n_\downarrow)$ was absorbed by the chemical potential $\mu = \frac{U}{2}$. The inverse Green function is

$$\hat{G}_\sigma^{-1}(\boldsymbol{s}) \equiv \hat{a}_\sigma + \sigma\lambda\hat{A}(\boldsymbol{s}), \tag{1.83}$$

with

$$\hat{A}(\boldsymbol{s}) = \begin{pmatrix} 0 & \cdots & 0 & 0 & -s_L \\ s_1 & 0 & & \ddots & 0 \\ 0 & \ddots & \ddots & & 0 \\ \vdots & \ddots & \ddots & 0 & \vdots \\ 0 & \cdots & 0 & s_{L-1} & 0 \end{pmatrix}. \tag{1.84}$$

The matrix $\hat{A}(\boldsymbol{s})$ includes the interaction between the neighboring components of the auxiliary field (Ising spins). In the present formulation, the Green function (1.84) is written as (see [4])

$$\hat{G}_\sigma^{-1}(\boldsymbol{s}) \equiv \hat{a}_\sigma \hat{e}_\sigma^V(\boldsymbol{s}) + \hat{e}_\sigma^V(\boldsymbol{s}) - \hat{1}, \tag{1.85}$$

where $\hat{e}_\sigma^V(\boldsymbol{s}) = \mathrm{diag}\left(e^{\sigma\lambda s_1}, \dots, e^{\sigma\lambda s_L}\right)$ is an $L \times L$ matrix, with $\sigma = \pm 1$.

Due to the quadratic action the Gauss integration of the Grassmann variables can be performed (see section 1.3.1):

$$Z = \frac{1}{2^L} \sum_{\boldsymbol{s}} \prod_\sigma \det\left[\hat{G}_\sigma^{-1}(\boldsymbol{s})\right] \tag{1.86}$$

and

$$\hat{G}_\sigma = \frac{1}{2^L Z} \sum_{\boldsymbol{s}} \hat{G}_\sigma(\boldsymbol{s}) \prod_{\sigma'} \det\left[\hat{G}_{\sigma'}^{-1}(\boldsymbol{s})\right]. \tag{1.87}$$

The computational time for the upper sum is reasonable for small L only, therefore the Green function is calculated by stochastic Monte Carlo sampling, where a term $\prod_{\sigma'} \det\left[G_{\sigma'}^{-1}(\boldsymbol{s})\right]$ gives the stochastic weight of a configuration $\boldsymbol{s} = (s_1, \dots, s_L)$. The configurations are generated by a Markov process, where the probability of a configuration is proportional to its statistical weight. To reduce the computational effort we consider single spin-flip moves $(s_1, \dots, s_k, \dots, s_L) \to (s_1, \dots, -s_k, \dots, s_L)$ only.

Implementation

The complete derivation of the equations, needed in the QMC algorithm, was often presented in the literature and can be found, among others, in [4, 25]. Therefore we focus our attention on the basic equations, specialized for two impurities.

The QMC algorithm used here calculates the Green function as a function of imaginary time, therefore we start with the Green function in the τ-matrix representation:

$$
\hat{G}_\sigma = \begin{pmatrix}
\left\langle c_{0\tau_1} c_{0\tau_1}^\dagger \right\rangle_\sigma & \cdots & \left\langle c_{0\tau_L} c_{0\tau_1}^\dagger \right\rangle_\sigma & \left\langle c_{1\tau_1} c_{0\tau_1}^\dagger \right\rangle_\sigma & \cdots & \left\langle c_{1\tau_L} c_{0\tau_1}^\dagger \right\rangle_\sigma \\
\vdots & \ddots & \vdots & \vdots & \ddots & \vdots \\
\left\langle c_{0\tau_1} c_{0-\tau_L}^\dagger \right\rangle_\sigma & \cdots & \left\langle c_{0\tau_L} c_{0\tau_L}^\dagger \right\rangle_\sigma & \left\langle c_{1\tau_1} c_{0-\tau_L}^\dagger \right\rangle_\sigma & \cdots & \left\langle c_{1\tau_L} c_{0\tau_L}^\dagger \right\rangle_\sigma \\
\left\langle c_{0\tau_1} c_{1\tau_1}^\dagger \right\rangle_\sigma & \cdots & \left\langle c_{0\tau_L} c_{1\tau_1}^\dagger \right\rangle_\sigma & \left\langle c_{1\tau_1} c_{1\tau_1}^\dagger \right\rangle_{\bar\sigma} & \cdots & \left\langle c_{1\tau_L} c_{1\tau_1}^\dagger \right\rangle_{\bar\sigma} \\
\vdots & \ddots & \vdots & \vdots & \ddots & \vdots \\
\left\langle c_{0\tau_1} c_{1-\tau_L}^\dagger \right\rangle_\sigma & \cdots & \left\langle c_{0\tau_L} c_{1\tau_L}^\dagger \right\rangle_\sigma & \left\langle c_{1\tau_1} c_{1-\tau_L}^\dagger \right\rangle_{\bar\sigma} & \cdots & \left\langle c_{1\tau_L} c_{1\tau_L}^\dagger \right\rangle_{\bar\sigma}
\end{pmatrix}, \tag{1.88}
$$

where $c_{i\tau} = c_i(\tau)$, $\tau_1 = 0$, $\tau_L = \beta - \Delta\tau$. The computation begins with a free Green function, which corresponds to the configuration where all Ising spins were set to 0. The initial Green matrix (1.88), with $\left\langle c_{i\tau_k} c_{j\tau_l}^\dagger \right\rangle_\sigma = \mathcal{G}_{ij\sigma}(\tau_k - \tau_l)$, with $i, j \in \{0, 1\}$, will be transformed into the Green matrix corresponding to the first (random) configuration of the non-zero Ising spins according to the equation

$$
\hat{G}_\sigma^{\text{New}} = \hat{\mathcal{A}}_\sigma^{-1} \hat{G}_\sigma, \tag{1.89}
$$

with

$$
\hat{\mathcal{A}}_\sigma = \hat{1} + \left(\hat{1} - \hat{G}_\sigma \right) \left(\hat{e}_\sigma^{V^{\text{New}} - V} - \hat{1} \right), \tag{1.90}
$$

where the matrix $\hat{e}_\sigma^{V^{\text{New}} - V}$ is defined as

$$
\text{diag} \left[\sigma\lambda \left(s_{01}^{\text{New}} - s_{01} \right), \ldots, \sigma\lambda \left(s_{0L}^{\text{New}} - s_{0L} \right), \bar\sigma\lambda \left(s_{11}^{\text{New}} - s_{11} \right), \ldots, \bar\sigma\lambda \left(s_{1L}^{\text{New}} - s_{1L} \right) \right]. \tag{1.91}
$$

Note that equation (1.89) holds true for *any* two configurations of Ising spins, however its disadvantage is the high computational effort, which is not acceptable in a Monte Carlo simulation. A special case of equation (1.89) for two configurations, which differ in one *single spin* $k \in 1, \ldots, L$ (Sherman-Morrison formula)

$$
\begin{aligned}
G_{k_1 k_2 \sigma}^{\text{New}} = G_{k_1 k_2 \sigma} + \left(G_{k_1 k \sigma} - \delta_{k_1 k} \right) \left(e_{kk\sigma}^{V^{\text{New}} - V} - 1 \right) \times \\
\times \left[1 + (1 - G_{kk\sigma}) \left(e_{kk\sigma}^{V^{\text{New}} - V} - 1 \right) \right]^{-1} G_{kk_2\sigma},
\end{aligned} \tag{1.92}
$$

yields a numerically cheaper way for the transition from one configuration to a different one. In fact, in order to perform equation (1.89) we need $(2L)^3$ numerical operations[7], whereas equation (1.92) requires $(2L)^2$ operations only, which is a crucial difference for the computational time needed for a Monte Carlo simulation.

---

[7]We are talking about the multiplication and the division, the time, which we need for the summation can be neglected.

The transition probability $P(\boldsymbol{s} \to \boldsymbol{s}^{\mathrm{New}})$, which gives the likelihood that the system moves from the configuration $\boldsymbol{s}$ to the configuration $\boldsymbol{s}^{\mathrm{New}}$, can be obtained using the "Boltzmann" weights of the considered states. The "Boltzmann" weight ratio is given by

$$\frac{\det\left[\hat{G}_\sigma\right]}{\det\left[\hat{G}_\sigma^{\mathrm{New}}\right]} = \det\left[\hat{\mathcal{A}}_\sigma\right] = 1 + (1 - G_{kk\sigma})\left(e_{kk\sigma}^{V^{\mathrm{New}}-V} - 1\right), \tag{1.93}$$

yields the transition probability needed in the Markov process.

Equations (1.89)–(1.93) form a complete set, which is sufficient in order to solve a two-impurity problem. In order to get a general idea, we repeat the crucial steps of the Hirsch-Fye QMC algorithm:

1. Start with the free Green function, which is identical to the Green function (1.88) with the initial configuration of the Ising spins ($s_{01} = 0, \ldots, s_{1L} = 0$).

2. Choose an arbitrary configuration of Ising spins $\boldsymbol{s}$, with $s_{01}, \ldots, s_{1L} \in \{\pm 1\}$ and calculate the corresponding Green function using equation (1.89).

3. Visit different Ising spin configurations via single spin flips (1.92) using the Metropolis Monte Carlo dynamics, that satisfying the "detailed balance condition"

$$\frac{P\left(\boldsymbol{s} \to \boldsymbol{s}^{\mathrm{New}}\right)}{P\left(\boldsymbol{s}^{\mathrm{New}} \to \boldsymbol{s}\right)} = \frac{\prod_\sigma \det\left[\hat{G}_\sigma\right]}{\prod_\sigma \det\left[\hat{G}_\sigma^{\mathrm{New}}\right]}, \tag{1.94}$$

which leads to the Metropolis transition probability

$$P(\boldsymbol{s} \to \boldsymbol{s}^{\mathrm{New}}) = \begin{cases} 1, & \text{if } \displaystyle\prod_\sigma \det\left[\hat{G}_\sigma\right] > \prod_\sigma \det\left[\hat{G}_\sigma^{\mathrm{New}}\right] \\[2ex] \dfrac{\prod_\sigma \det\left[\hat{G}_\sigma\right]}{\prod_\sigma \det\left[\hat{G}_\sigma^{\mathrm{New}}\right]} & \text{otherwise.} \end{cases} \tag{1.95}$$

The ratio is given by equation (1.93).

4. The expectations value of the Green function is obtained by the average over all Green functions $\hat{G}_\sigma(\boldsymbol{s})$ corresponding to the Ising spin configurations $\boldsymbol{s}$ visited in the course of the calculation.

Technical details

In this section we want to explane some useful points, which will increase the quality of the data, calculated by the algorithms including Hirsch-Fye QMC. The upper Quantum Monte-Carlo method treats the Green function on the imaginary time axis, but the self-consistency is performed in the Matsubara frequency space. Therefore we have a Fourier

transformation (FT) and an inverse Fourier transformation (IFT) in our DMFT algorithm. Both transformations should be performed very carefully, otherwise the additional inaccuracies will plague the computed quantities.

Fourier transformation $G(\omega_n) \rightarrow G(\tau_l)$ At first we consider a transformation from the ω_n-space into the $\tau-$space. The Green function $G_{0/1}(\omega_n)$ (or the inverse Weiss field $\mathcal{G}_{0/1}(\omega_n)$) is numerically calculated at $\omega_n \in \{-\omega_N, \ldots, \omega_N\}$, but an exact result will be achieved only, if we perform the Fourier transformation taking *all* Matsubara frequencies into account

$$G_j(\tau_l) = \frac{1}{\beta} \sum_{n=-\infty}^{\infty} e^{-i\omega_n \tau_l} G_j(\omega_n), \tag{1.96}$$

with $l \in \{1, \ldots, \text{Ł}\}$ and $j \in \{0, 1\}$. It is evident, that neither of numerical techniques will compute the upper sum exactly, therefore we should make use of the analytical knowledge about the high frequency behavior of the Green function. In appendix A.1 we show, that the Green functions (in our case G_0 and G_1) can be substituted by the following approximate functions

$$\begin{aligned} G_0(\omega_n) &\approx \tilde{G}_0(\omega_n) = \frac{1}{i\omega_n} \\ G_1(\omega_n) &\approx \tilde{G}_1(\omega_n) = \frac{zt}{4\omega_n^2}, \end{aligned} \tag{1.97}$$

at high frequencies ($1 \ll |\omega_n|$). Therefore it should be found out, when ω_N is large enough for the switch to the approximate function. Figure 1.6 displays $G_0(\omega_n)$ and $G_1(\omega_n)$ calculated at $T/t = 0.1$, $U/t = 2, 6, 10$, whereas the Néel phase was suppressed. The insets show the corresponding ratio $G_j/\tilde{G}_j$. From this figure we learn that the aberration from the approximated function is proportional to the value of the Coulomb repulsion. The aberration of the G_0 (upper panel) decreases rapidly beyond the frequency $\omega_n = 10U$. The deviation decreases from $\approx 0.3\%$ to $\approx 0.15\%$ on the interval $[10U; 15U]$. The evolution of the aberration in the same interval on the lower panel shows the similar behavior, where the difference decreases from $\approx 0.7\%$ to $\approx 0.35\%$. The inaccuracy is comparable to the wrongness of the original data, thus it is recommendable to take the ω_N beyond the $15U$ mark, also it is reasonable to take $\omega_N = 5W$, where W is the full band width, in case, if the value of the interaction is small ($U/t < 3$).

So the Fourier transformation will be performed in the following manner

$$G_j(\tau_l) \approx \frac{1}{\beta} \left(\sum_{n=-N}^{N} e^{-i\omega_n \tau_l} G_0(\omega_n) + \sum_{n=-\infty}^{\infty} e^{-i\omega_n \tau_l} \tilde{G}_j(\omega_n) - \sum_{n=-N}^{N} e^{-i\omega_n \tau_l} \tilde{G}_i(\omega_n) \right), \tag{1.98}$$

where the infinite sum is calculated analyticaly (for details see appendix A.1).

Inverse Fourier transformation $G(\tau_l) \rightarrow G(\omega_n)$ The inverse Fourier transformation is one of the most problematical numerical parts of the algorithm. The Hirsch-Fye QMC
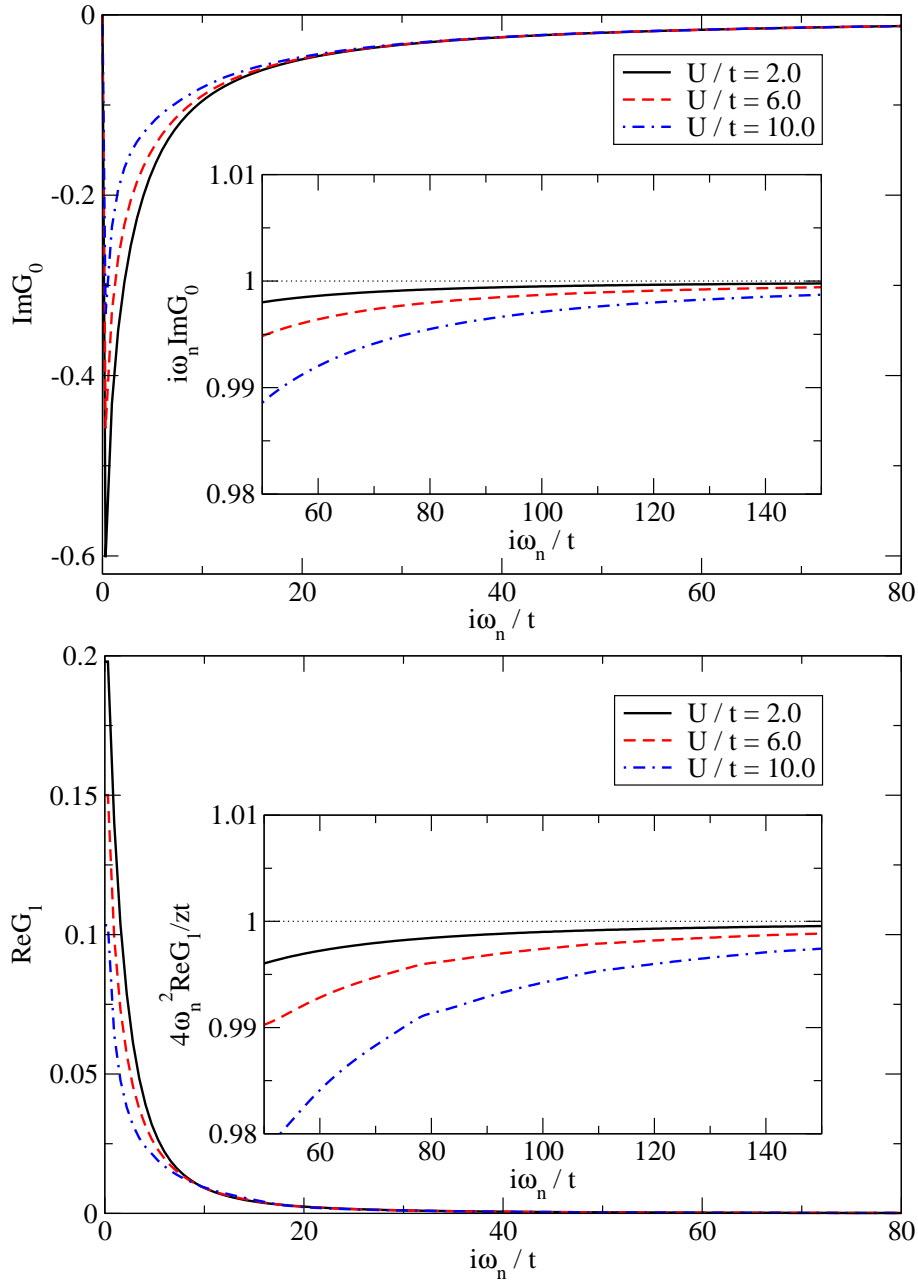
Figure 1.6: The evolution of the Green functions at high frequency. The upper panel shows the imaginary part of G_0 and the lower panel gives the real part of G_1. The inset shows the ratio $G_j/\tilde{G}_j$ in each case (see also the discussion in text). $T/t = 0.1$, $U/t = 2$, 6, 10, $W/t = 8$, $n = 1$ and $L = 50$. The Néel phase was artificially suppressed.

procedure yields a Green function, which is known at L discrete τ_l-values, where L is the number of time slices in the QMC approach. An increasing of the number of time slices causes a growth of the computational time, which is proportional to L^3, therefore the number of time slices is limited. Usually, the discrete Green function $G(\tau_l)$ is interpolated using a cubic spline, which leads to the approximate continues Green function $G(\tau)$, so the IFT can be performed:

$$G_j(\omega_n) \approx \int_0^\beta d\tau \, e^{i\omega_n\tau} G_j(\tau), \tag{1.99}$$

however the 3rd order spline leads to some inaccuracies above the Nyquist frequency $\omega_N = L\pi/\beta$. In fact, the Green function has both magnitude and derivative discontinuities at $\tau = 0$ and $\tau = \beta$, that causes unphysical oscilations of the spline around the trace of the actual Green function at short imaginary time as well as around $\tau = \beta$. In order to compute the high frequency behavior correctly, one should perform the short time interpolation very carefully. We found that the interpolation of G_0 (G_1) using a fourth (fifth) order spline, with boundary conditions $G_j^{(k)}(0) + (-1)^j G_j^{(k)}(\beta) = 0$, where $G^{(k)}(\tau)$ is the derivative of k'th order, $k \in \{1, 2, 3\,(, 4)\}$ and $j \in \{0\,1\}$, gives better results than the cubic spline. In fact, the cubic spline is discontinuous in the third derivative, which effects an unphysical behavior of the self-energy. Figure 1.7 shows the on-site self-energy calculated using 3rd (dash-dotted curve) and 4th (dashed curve) order splines, where the first curve changes the sign and at the same time the second self-energy has correct strict negative sign in the shown region. However, the high frequency behavior is still wrong, therefore performing the Fourier transformation we make use of the analytical knowledge about the behavior of the Green function at large $|\omega_n|$. The following trick, introduced in the PhD thesis by Blümer [28], allows to compute the self-energy with the correct high-frequency behavior:

1. Calculate the model Green function[8] $\tilde{G}_{j\sigma}(\omega_n) = \int (dp) \frac{\gamma^{(j)}}{i\omega_n + \mu - \varepsilon_{\boldsymbol{p}} - \tilde{\Sigma}_\sigma(\omega_n)}$, where the model self-energy is $\tilde{\Sigma}_\sigma(\omega_n) = U(n_{\bar\sigma} - 0.5) + U^2 n_{\bar\sigma}(1.0 - n_{\bar\sigma})/(i\omega_n)$.

2. Perform the Fourier transformation $\tilde{G}_{j\sigma}(\omega_n) \to \tilde{G}_{j\sigma}(\tau_l)$ according to the previous paragraph.

3. Compute the difference between the discrete QMC Green function and the model Green function $\Delta G_{j\sigma}(\tau_l) = G_{j\sigma}(\tau_l) - \tilde{G}_{j\sigma}(\tau_l)$.

4. Fourier transform the difference $\Delta G_{j\sigma}(\tau_l) \to \Delta G_{j\sigma}(\omega_n)$, which can be done approximately exact, because we have the low frequencies only.

5. Get the Green function in the frequency space $G_{j\sigma}(\omega_n) = \Delta G_{j\sigma}(\omega_n) + \tilde{G}_{j\sigma}(\omega_n)$.

---

[8]The approach is given for the FI method, but it can be easily modified according to the requirements of an other method.
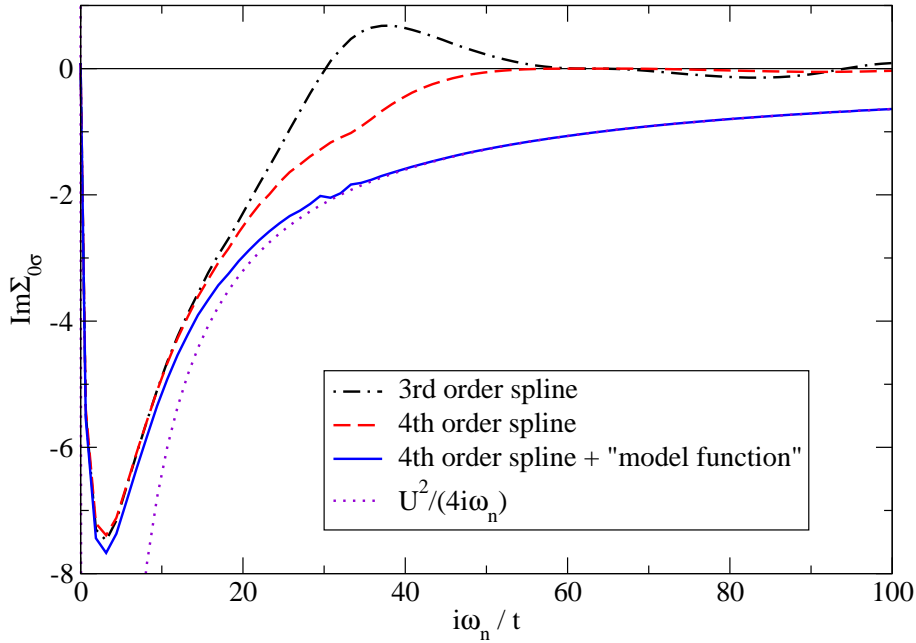
Figure 1.7: The on-site self-energy calculated using different techniques at $T/t = 0.2$, $U/t = 16$, $n = 1$ and $L = 48$. The corresponding Green function was Fourier transformed using 3rd order spline, 4th order spline and 4th order spline with the "model function" trick.

The solid curve in Fig. 1.7 is the self-energy calculated by this procedure. The low frequency part is in agreement with both other curves, but the high frequency behavior is consistent with the analytical result (dotted curve).

In general, the data calculated by the Hirsch-Fye Quantum Monte Carlo algorithm conforms to the experimental data, therefore this method has a good reputation among the physicists. The best results can be achieved at the finite temperature (substantially lower than the band width) in the low- and medium-coupling regime. Because of the Trotter breakup[9] the spacing $\Delta\tau = \beta/L$ should be kept small (generally $\Delta\tau \cdot U \leq 1$). On this account, the calculations at the temperatures close to $T = 0$ and in the strong coupling regime are possible, but associate with a significant increasing of the computational time. Thus the choice of the impurity solver should be matched to the considered temperature-repulsion regime.

QMC vs. SCA

In the present section we are going to compare the Green functions computed by the Hirsch-Fye Quantum Monte Carlo algorithm and by the semiclassical approximation in the medium- and in the large-U regime. Figure 1.8 (upper panel) displays the Green

---

[9] $e^{-\Delta\tau(\hat{H}_0 + \hat{H}_1)} \approx e^{-\Delta\tau\hat{H}_0} e^{-\Delta\tau\hat{H}_1}$.
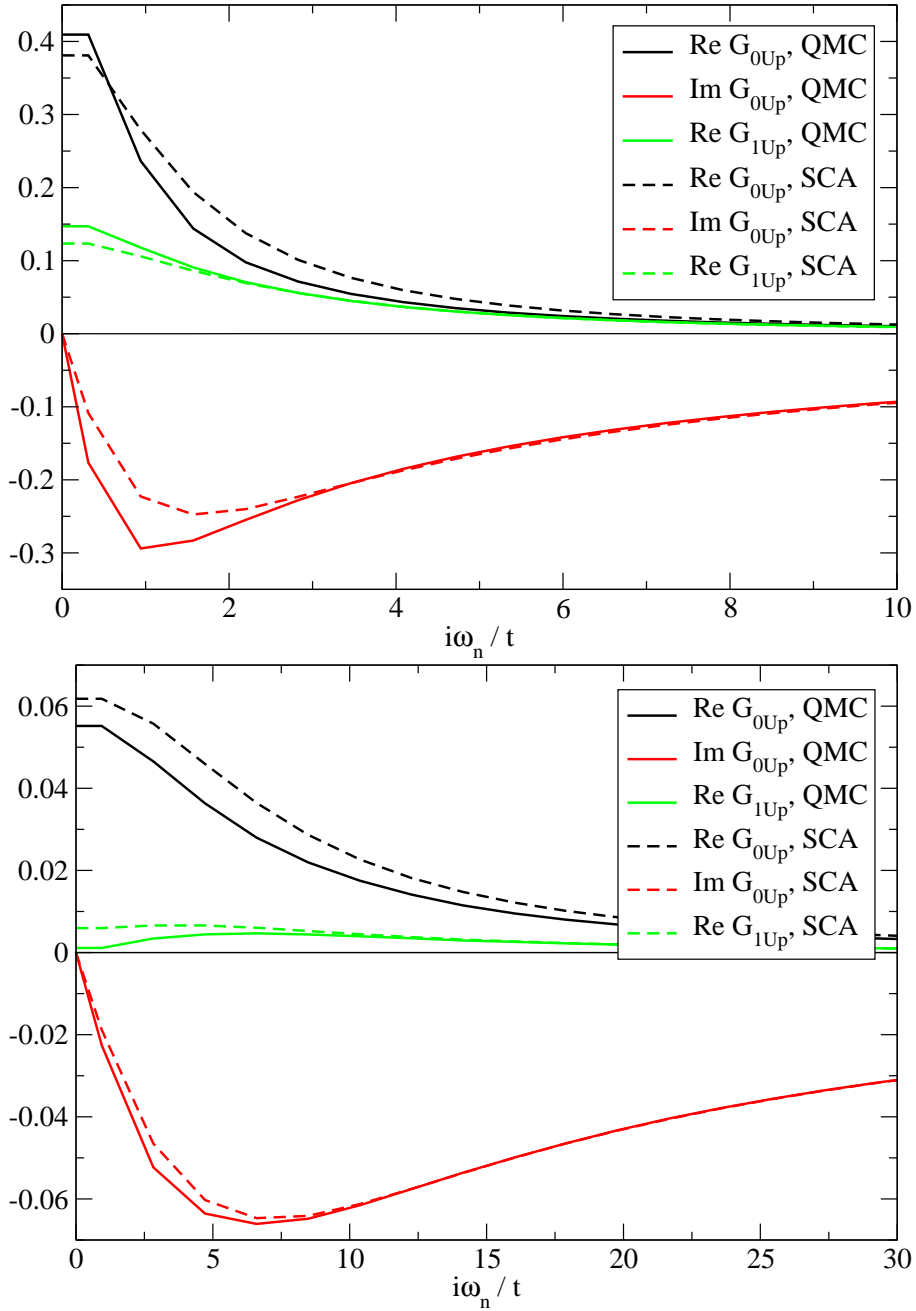
Figure 1.8: G_0 and G_1 calculated by the QMC and the SCA at $T/t = 0.1$, $U/t = 4$ (upper panel) and at $T/t = 0.3$, $U/t = 16$ (lower panel), antiferromagnetic order. The SCA result slightly differs from the QMC one, however the general agreement is notable, because the QMC is a nearly exact method and the SCA is an approximation only.

functions $G_{0\uparrow}$ and $G_{1\uparrow}$ calculated by the QMC ($t\Delta\tau = 0.2$) and by the integral-SCA in the medium-U regime ($U/t = 4$). The imaginary part of $G_{1\uparrow}$ is equal zero. The on-site Green function and the nearest neighbor Green function, obtained by both numerical methods, are mostly similar, however the semiclassical result is slightly underestimated in the low-frequency region. The lower panel shows both results at $U/t = 16$ and $T/t = 0.3$ also in the antiferromagnetic regime. We observe a deviation of nearly the same order in the large-U regime.

Due to the results, we conclude, that the Hirsh-Fye QMC method is substitutable by the present SCA version (section 1.3.1) at least at half filling[10]. The best accordance was achieved in the antiferromagnetic regime. The agreement in the single impurity case was excellent in the paramagnetic as well as in the antiferromagnetic order. Anyway, the semiclassical approximation takes up to second order of magnitude less computational time which was the crucial point for our decision to use the SCA in the present work.

1.4 Approximate Analytical Results

In order to examine our numerical data we obtain the approximate analytical results for a single-site model and for both 2-site methods [34, 35]. The equations will be written for general dimension d in low-temperature limit, where thermal excitations into the upper Hubbard band may be neglected, which legitimates the substitution $T\sum_{\omega_n} \approx \frac{1}{2\pi}\int d\omega$. Due to the fact that SCA was used as an impurity solver in the dynamical mean field theory, we begin with an analytical treatment of the semiclassical approximation. Then we calculate an approximate internal energy for the single impurity DMFT and 2-site FI method and DCA as well as an approximate spin correlation function[11].

1.4.1 Semiclassical Approximation

We start with the partition function in the large-U limit (eq. (1.64)) and concentrate our attention on the paramagnetic case. In order to simplify the considered equations we substitute $\frac{\varphi_i}{2}$ by ϕ_i. Also we assume that in the large-U limit $|a_1| \ll |a_0^2 - \phi^2|$ and that we do not have a spatial symmetry breaking, which means $|\phi|$ is the same on both sites. We expand the two-site potential (1.60) up to second order in the parameter $x = \frac{a_1^2}{a_0^2 - \phi^2}$

$$
\begin{aligned}
V(\boldsymbol{\phi}) &= \frac{|\boldsymbol{\phi}|^2}{U} - T\sum_{\omega_n} \ln \det\left[-\beta\left(\begin{array}{cc} \hat{a}_0 + \phi\hat{\sigma}_{1z} & \hat{a}_1 \\ \hat{a}_1 & \hat{a}_0 + \phi\hat{\sigma}_{2z} \end{array}\right)\right] \\
&= \frac{2\phi^2}{U} - T\sum_{\omega_n} \ln\left[\beta^4(a_0^2 - \phi^2)^2\left(1 - \frac{2(a_0^2 + \phi^2\sigma_{1z}\sigma_{2z})}{a_0^2 - \phi^2}x + x^2\right)\right],
\end{aligned}
\tag{1.100}
$$

---

[10] All considered systems in this work are at half-filling.

[11] In order to keep equations readable we will not write the ω_n-dependency explicit in the current section.

where $|x| \ll 1$, and $\hat{a}_0$ and $\hat{a}_1$ are 2×2 matrices in the spin space. Using the approximation $\ln(1 + bx + \mathcal{O}(x^2)) \approx bx$ we obtain

$$V(\boldsymbol{\phi}) \approx \frac{2\phi^2}{U} - 2T \sum_n \left[\ln\left(\beta^2 \left(a_0^2 - \phi^2\right)\right) - \frac{a_1^2(a_0^2 + \phi^2 S)}{(a_0^2 - \phi^2)^2} \right], \qquad (1.101)$$

where $S \equiv \sigma_{1z}\sigma_{2z}$. The ϕ-differentiation of the effective potential gives an equation

$$\frac{1}{U} = -T \sum_n \left[\frac{1}{a_0^2 - \phi^2} + \frac{a_1^2 \left(2a_0^2 + S\left(a_0^2 + \phi^2\right)\right)}{(a_0^2 - \phi^2)^3} \right], \qquad (1.102)$$

that allows to obtain the extremal values of ϕ. The impurity model Green function, defined in equation (1.19), becomes

$$
\begin{aligned}
G_0 &= \frac{a_0}{a_0^2 - \phi^2}\left(1 + \frac{a_1^2\left(a_0^2 + \phi^2(1 + 2S)\right)}{(a_0^2 - \phi^2)^2}\right) \\
G_1 &= \frac{-a_1\left(a_0^2 + \phi^2 S\right)}{(a_0^2 - \phi^2)^2}.
\end{aligned}
\qquad (1.103)
$$

The approximate self-energy $\hat{\Sigma} = \begin{pmatrix} \Sigma_0 & \Sigma_1 \\ \Sigma_1 & \Sigma_0 \end{pmatrix}$ can be calculated using the Dyson equation $\hat{\Sigma} = \hat{a} - \hat{G}^{-1}$, which requires inverting of $\hat{G}$. At large U (in the Mott insulating phase) we expect that $|G_1| \ll |G_0|$, so the inversion can be executed perturbatively in G_1. However, the substitution of a_0 and a_1 by approximate values[12] $i\omega_n$ and t respectively in equations (1.103) denotes $|G_1| > |G_0|$ at $\omega_n < tS$. Using $S \approx -\frac{t^2}{TU}$ (see section A.3) we get a lower temperature border of present approximation: $\omega_0 = \pi T > \frac{t^3}{TU} \rightarrow T > \sqrt{\frac{t^3}{\pi U}}$. Keeping in mind this temperature restriction, we obtain the self-energy

$$
\begin{aligned}
\Sigma_0 &= a_0 - \frac{G_0}{G_0^2 - G_1^2} \approx a_0 - \frac{1}{G_0}\left(1 + \frac{G_1^2}{G_0^2}\right) \\
&\approx a_0 - \frac{a_0^2 - \phi^2}{a_0}\left(1 - \frac{a_1^2\left(a_0^2 + \phi^2(1 + 2S)\right)}{(a_0^2 - \phi^2)^2}\right) - \frac{a_1^2\left(a_0^2 + \phi^2 S\right)^2}{a_0^3\left(a_0^2 - \phi^2\right)} \\
&= \frac{\phi^2}{a_0}\left[1 + \frac{a_1^2}{a_0^2 - \phi^2}\left(1 - \frac{\phi^2 S^2}{a_0^2}\right)\right] \\
\Sigma_1 &= a_1 + \frac{G_1}{G_0^2 - G_1^2} \approx a_1 + \frac{G_1}{G_0^2} \approx a_1 - \frac{a_1}{a_0^2}\left(a_0^2 + \phi^2 S\right) = -\frac{a_1 \phi^2 S}{a_0^2}.
\end{aligned}
\qquad (1.104)
$$

To conclude, we note, that in the large-U limit the value of $|i\omega_n - \Sigma_0|$ is significantly greater than the bandwidth, which allows an expansion of $G_{0/1}(\omega_n, \boldsymbol{p})$ in powers of $\frac{t}{|i\omega_n - \Sigma_0|}$.

---

[12]Approximate values will be calculated later.

1.4.2 Single-Site Approximation

The single-site problem implies $a_1 = 0$ and simplifies equations (1.103) and (1.104). Using $\int (dp) = \prod_{i=1}^{d} \frac{1}{2\pi} \int_{-\pi}^{\pi} dp_i$ and $\int (dp) \varepsilon_{\boldsymbol{p}}^2 = 2dt^2 \equiv K_d$ we solve the self-consistency equation

$$\frac{a_0}{a_0^2 - \phi^2} = \int (dp) \frac{1}{i\omega_n - \varepsilon_{\boldsymbol{p}} - \frac{\phi^2}{a_0}} \approx \frac{1}{i\omega_n - \frac{\phi^2}{a_0}} + \frac{K_d}{\left(i\omega_n - \frac{\phi^2}{a_0} \right)^3}. \tag{1.105}$$

Inversion and following expansion lead to

$$a_0 \approx \frac{\phi^2}{a_0} + \left(i\omega_n - \frac{\phi^2}{a_0} \right) \left(1 - \frac{K_d}{\left(i\omega_n - \frac{\phi^2}{a_0} \right)^2} \right) \approx i\omega_n \left(1 + \frac{K_d}{\omega_n^2 + \phi^2} \right), \tag{1.106}$$

where the second approximate equality comes from a recurcive substitution of a_0. Substitution of the upper result in equation (1.102) leads to

$$\frac{1}{U} = -T \sum_n \frac{1}{a_0^2 - \phi^2} = T \sum_n \frac{1}{\omega_n^2 \left(1 + \frac{K_d}{\omega_n^2 + \phi^2} \right)^2 + \phi^2}$$

$$\approx T \sum_n \left(\frac{1}{\omega_n^2 + \phi^2} - \frac{2\omega_n^2 K_d}{(\omega_n^2 + \phi^2)^3} \right) \approx \frac{1}{2\pi} \int d\omega \left(\frac{1}{\omega^2 + \phi^2} - \frac{2\omega^2 K_d}{(\omega^2 + \phi^2)^3} \right) \tag{1.107}$$

$$\approx \frac{1}{2\phi} - \frac{K_d}{8\phi^3},$$

the integration was performed using formulary (e.g. [36]). Putting $\phi = \frac{U}{2} + \delta\phi$ we expand the upper equation and get $\delta\phi \approx -\frac{K_d}{2U}$, which denotes

$$\phi \approx \frac{U}{2} - \frac{K_d}{2U}. \tag{1.108}$$

The calculation of the internal energy (1.34) is now straightforward

$$E \approx 2T \sum_n \int (dp) \left(\varepsilon_{\boldsymbol{p}} + \frac{1}{2}\Sigma_0 \right) \left(\frac{1}{i\omega_n - \Sigma_0} + \frac{\varepsilon_{\boldsymbol{p}}}{(i\omega_n - \Sigma_0)^2} + \frac{\varepsilon_{\boldsymbol{p}}^2}{(i\omega_n - \Sigma_0)^3} \right)$$

$$\approx -2T \sum_n \left(\frac{\frac{1}{2}\phi^2}{\omega_n^2 \left(1 + \frac{K_d}{\omega_n^2 + \phi^2} \right) + \phi^2} + \frac{K_d \omega_n^2}{(\omega_n^2 + \phi^2)^2} - \frac{\frac{1}{2}\phi^2 K_d \omega_n^2}{(\omega_n^2 + \phi^2)^3} \right) \tag{1.109}$$

$$\approx -\frac{1}{\pi} \int d\omega \left[\frac{\frac{1}{2}\phi^2}{\omega^2 + \phi^2} - \frac{\phi^2 K_d \omega^2}{(\omega^2 + \phi^2)^3} + \frac{K_d \omega^2}{(\omega^2 + \phi^2)^2} \right] \approx -\frac{\phi}{2} + \frac{K_d}{8\phi} - \frac{K_d}{2\phi}$$

$$\approx -\frac{U}{4} - \frac{K_d}{2U} = -\frac{U}{4} - \frac{dt^2}{U}.$$

So we have obtained the approximate energy for the single-site DMFT in the paramagnetic state at large-U.

	FI approach	DCA
a_0	$i\omega_n \left(1 + \frac{K_d}{\omega_n^2 + \phi^2}\left(1 - \frac{1}{2d}\right)\left(1 - \frac{\phi^2 S}{a_0^2}\right)^2\right)$	$i\omega_n \left(1 + \frac{K_d - I_d^2}{\omega_n^2 + \phi^2}\right)$
a_1	t	$-I_d$
ϕ	$\frac{U}{2} - \frac{K_d}{2U} + \frac{K_d}{2U}\left(6 - \frac{5}{2d}\right)S - \frac{K_d}{T}\left(1 - \frac{1}{2d}\right)S^2$	$\frac{U}{2} - \frac{K_d}{2U} + \frac{I_d^2}{2U}S$
E	$-\frac{U}{4} - \frac{K_d}{2U} - \frac{K_d}{2U}\left(3 - \frac{19}{8d}\right)S - \frac{3K_d}{8U}S^2 + \frac{3K_d}{4T}\left(1 - \frac{1}{2d}\right)S^2$	$-\frac{U}{4} - \frac{K_d}{2U} + \frac{I_d^2}{2U}S$
$\langle S \rangle$	$-\frac{t^2}{TU}$	$-\frac{I_d^2}{TU}$

Table 1.1: Comparison of the approximate analytical large-U results for 2-site FI model and DCA. For details see corresponding text as well as appendix A.5.

1.4.3 Two-Site Approximation

In current subsection we treat approximatively the two-site real space model and two-site DCA. The procedure is similar to the approximation in the previous subsection, the only difference is a 2×2-matrix form of the Weiss field, the Green function and the self-energy. Due to the size of equations we put all derivations into appendix A.5 and resume the most important results in the table 1.1. We see that in the limit of high dimension ($d \to \infty$), where we return to the single-site DMFT, the quantities from the upper table become identical with the corresponding quantities in subsection 1.4.2. In fact, in the large-d limit $t \sim \frac{1}{\sqrt{2d}}$, therefore $S \sim t^2 \sim \frac{1}{d} = 0$; also the integral I_d as a function of d converges to a finite value times hopping amplitude[13].

We focus our attention on the FI as well as on the DCA-energy. As expected, the first two terms reproduce the energy for the single-site DMFT in equation (1.109). The contribution of the intersite spin correlation shifts the energy curve away from the single-site solution: Because of the negative S, the DCA-curve lies lower than the single-site curve. In contrast to the DCA-energy, the energy in the real space model has three S-dependent terms, where both positive terms (linear S-term and T-dependent term) dominate and move the energy curve upwards. It is remarkable, that the DCA-energy is S^2- and T-independent in current order of approximation.

Finally, we discuss an expectation value of the approximate inter-site correlation $\langle S \rangle \equiv \langle \sigma_{1z}\sigma_{2z}\rangle$, which was not treated in the single-site subsection. Expanding the partition

---

[13]$I_1 \approx 1.27t$, $I_2 \approx 1.62t$, $I_3 \approx 2.00t$, $I_5 \approx 2.56t$, $I_7 \approx 3.01t$, ...

function up to leading order in $\frac{a_1^2}{a_0^2 - \phi^2}$ and assuming the same ϕ on both sites, lead to

$$
\langle S \rangle \approx \frac{\sum_{\sigma_{iz}} S e^{-\beta V(\sigma_{iz})}}{\sum_{\sigma_{iz}} e^{-\beta V(\sigma_{iz})}} = \frac{\sum_{\sigma_{iz}} S e^{-\beta \left(\frac{2\phi^2}{U} - 2T \sum_n \left[\ln\left(\beta^2\left(a_0^2 - \phi^2\right)\right) - \frac{a_1^2\left(a_0^2 + \phi^2 S\right)}{\left(a_0^2 - \phi^2\right)^2} \right] \right)}}{\sum_{\sigma_{iz}} e^{-\beta \left(\frac{2\phi^2}{U} - 2T \sum_n \left[\ln\left(\beta^2\left(a_0^2 - \phi^2\right)\right) - \frac{a_1^2\left(a_0^2 + \phi^2 S\right)}{\left(a_0^2 - \phi^2\right)^2} \right] \right)}}
$$

$$
\approx \frac{\sum_{\sigma_{iz}} S \left[1 - 2 \sum_n \frac{a_1^2(a_0^2 + \phi^2 S)}{(a_0^2 - \phi^2)^2} \right]}{\sum_{\sigma_{iz}} \left[1 - 2 \sum_n \frac{a_1^2(a_0^2 + \phi^2 S)}{(a_0^2 - \phi^2)^2} \right]} \approx \frac{1}{4} \sum_{\sigma_{iz}} \left[S - 2 \sum_n \frac{a_1^2(a_0^2 S + \phi^2)}{(a_0^2 - \phi^2)^2} \right]
$$

$$
= -2 \sum_n \frac{a_1^2 \phi^2}{(a_0^2 - \phi^2)^2} \approx -\frac{1}{T\pi} \int d\omega \frac{a_1^2 \phi^2}{(\omega^2 + \phi^2)^2} \approx -\frac{a_1^2}{TU},
$$

(1.110)

where we used $\sigma_{iz} = \pm 1$ and $i \in \{1, 2\}$. Note, the expectation value of S in two-site cases is inversely proportional to the temperature and to the Coulomb interaction, but the constants of proportionality in FI method and in DCA are different.

1.5 Numerical Results

In current section we present numerical results obtained by the methods described in the previous sections. The numerical data was compared to the high-temperature analytical as well as to the low-temperature approximate results. We have studied following quantities: the local density of states, the self-energy as a function of Matsubara and real frequencies, the NN and the NNN spin-spin correlation function, the internal energy, and the phase diagram. Also we have investigated the effect of the filtering in the fictive impurity method.

1.5.1 Density Of States

We start with a local density of states calculated at $U/t = 16$ and $T/t = 0.3$ (Figure 1.9). This temperature is below the actual Néel temperature for the real-space approximation (s. Fig. 1.15), therefore we suppressed the antiferromagnetism and present the results in an artificial paramagnetic state. The density of states on the upper panel was computed from the single site DMFT: the system is in the Mott insulating phase, with well separated upper and lower Hubbard bands at $\omega = U/2$ and $-U/2$ respectively. The middle panel depicts the spectral densities obtained for a 2-site cluster. As in the single-impurity model the two Hubbard bands are centered at $\pm U/2$, but do not have the same width, which is a consequence of the intersite magnetic correlations; such behavior is known from the single-site model, where the bands are substantially narrower in the fully ordered antiferromagnetic state, than in the paramagnetic phase. Also we can see a small unphysical
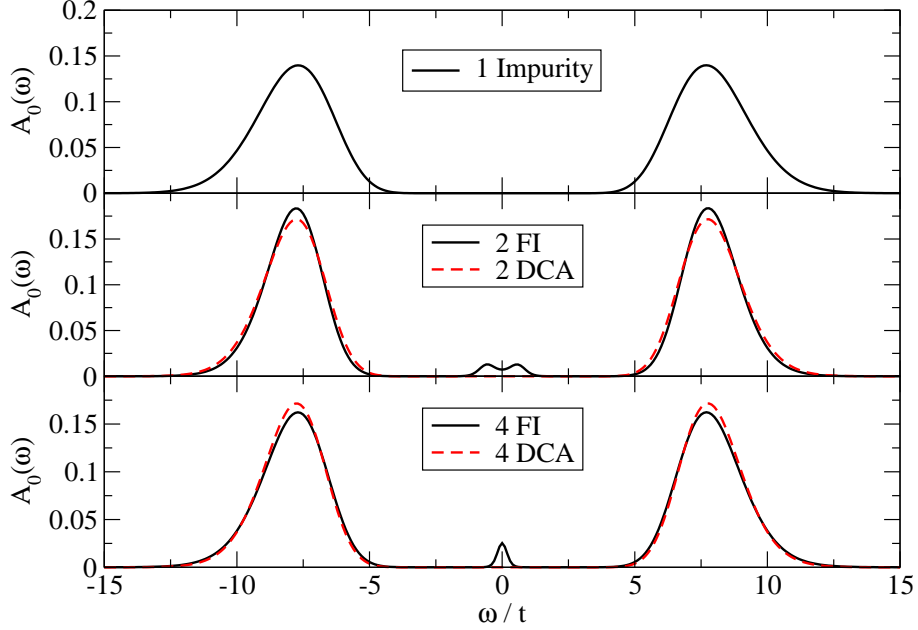
Figure 1.9: Spectral functions, obtained by FI method and DCA at $U/t = 16$ and $T/t = 0.3$. DOS's corresponds to the 1- (upper panel), 2- (middle panel) and 4-site (lower panel) cluster, whereas the antiferromagnetism was suppressed.

(actually we are in the insulating phase) band of the mid-gap states in the real space DOS, which is not visible in the two-site DCA result. The four-site cluster results are shown in the lower panel. The mid-gap states still appear in the DOS computed using the fictive impurity method. However, we note a decrease of the weight as well as the narrowness of the mid-gap states, which lets us assume a disappearance of the mid-gap states in an infinite-size system.

In order to gain insight about the mid-gap problem we use our large-U analytical treatment, to obtain the value of the self-energy at low frequencies. Considering the expression for the on-site Weiss field in the fictive impurity method

$$a_0(\omega_n) \approx i\omega_n \left(1 + \frac{K_d}{\omega_n^2 + \phi^2} \left(1 - \frac{1}{2d} \right) \left(1 - \frac{\phi^2 S}{a_0^2} \right)^2 \right), \qquad (1.111)$$

we see that the second term becomes dominant when $\omega < (dt^6/(2T^2))^{1/4}$. It means, that the lowest Matsubara freqency $\omega_0 = T\pi$ should be greater than the upper one, otherwise

$$a_0(T\pi) \approx \left(\frac{t^6}{T^2} \right)^{1/4}, \qquad (1.112)$$

whereas the non-vanishing of $a(\omega \to 0)$ leads mathematically to the mid-gap states. The absence of the divergent terms in a_0 in DCA explaines the nonexistence of the mid-gap states.

1.5.2 Self-Energy

Figure 1.10 shows the self-energy as a function of real frequency in the paramagnetic state (the antiferromagnetism was artificially suppressed). Real and imaginary parts of the self-energies for 1-, 2-, and 4-site clusters were compared. First of all we obtain a huge difference between the single-site and the multi-site on-site self-energy. Due to the mid-gap states, produced by the FI method, we have found a metallic solution in the 2- and 4-site systems at $U/t = 16$ but an insulating solution in the single-impurity system (compare Figure 1.9). The benchmark of 2- and 4-site self-energies does not display a basic difference, unless the 4-site solution has an additional component Σ_2. The non-vanishing of the Re Σ_1 at zero frequency is an artifact of the maximum entropy data analysis, which does not contain any physical statements. If we look at the maximal amplitudes of Σ_0, Σ_1, and Σ_2, we note a crude ratio of $50 : 5 : 1$ respectively, and get an impression about the contribution of the impurity self-energies to the general self-energy (1.13).

Figure 1.11 displays the imaginary part of the full lattice self-energy as a function of momentum at different frequencies for 2- and 4-site FI clusters. The main notable feature is the smoothness of the self-energy in the whole Brillouin zone, which is not guaranteed in the dynamical cluster approximation. Also we keep the momentum dependency of the self-energy which is not the case in the single-site DMFT.

The shape of the 2- and 4-site self-energies curves is mostly the same, whereas the 4-site self-energies exhibit as expected more structure. The "causality violation", where an intercept of the imaginary part of the self-energy has wrong sign discussed in [12], does not occur at $U/t = 16$ and $T/t = 0.3$, which denotes no relation between the mid-gap states and the "causality violation". In general we found some small sign problems in the 2-site result at large U and low T, but it can be easily fixed using a filtering procedure.

The four-site DCA self-energy is depicted in the lower panel of Figure 1.11. One can see a typical step-wise devolution of the self-energy computed using DCA. Due to the insulating result the magnitudes are significantly greater than in the FI case and the imaginary part of the self-energy does not vanish at the low frequencies only.

1.5.3 Impurity Model Spin Correlations

In this section we consider the spin correlations of the fictive impurity model. One should keep in mind, that the "fictive" impurity cluster is *not* a physical subcluster of the treated lattice, so the accordance of the impurity model spin correlations with the actual spin correlations in the real lattice is not absolute.

Nearest neighbor spin-spin correlation Figure 1.12 shows a nearest neighbor spin-spin correlation to the 2- and 4-site FI method (upper panel) and DCA (lower panel) results as a function of the temperature. The curves were computed in the antiferromagnetic as well as in the paramagnetic (the antiferromagnetism was suppressed) orders. The data was compared to the leading term in the high-temperature-series expansion as well as to the approximate analytical result (for details see section 1.4.3 and appendix A.3). A
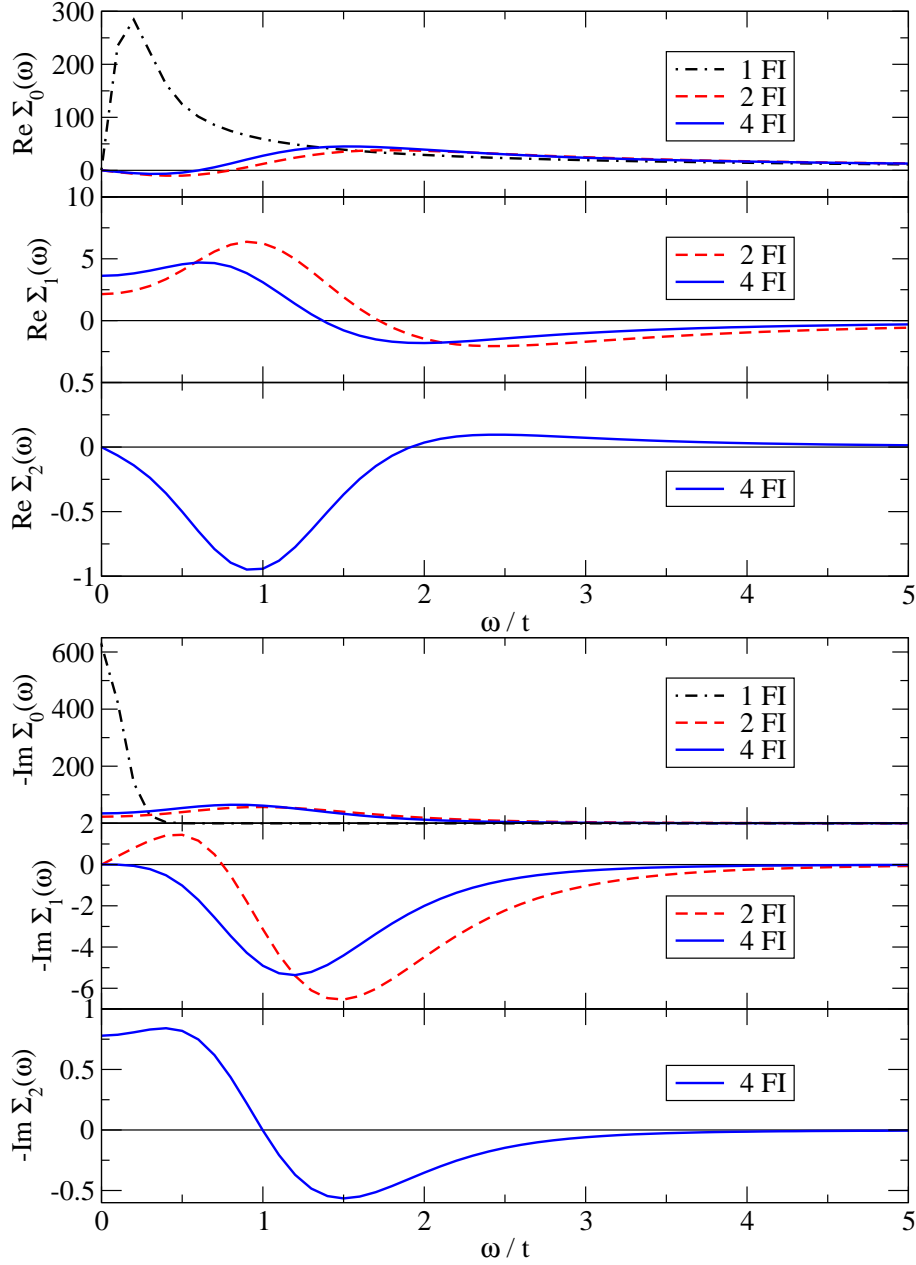
Figure 1.10: Impurity self-energies as a function of the real frequency. The results for 1-, 2-, and 4-site fictive impurity method were compared at $U/t = 16$ and $T/t = 0.3$. Upper panel: real part of the self-energy; lower panel: imaginary part.
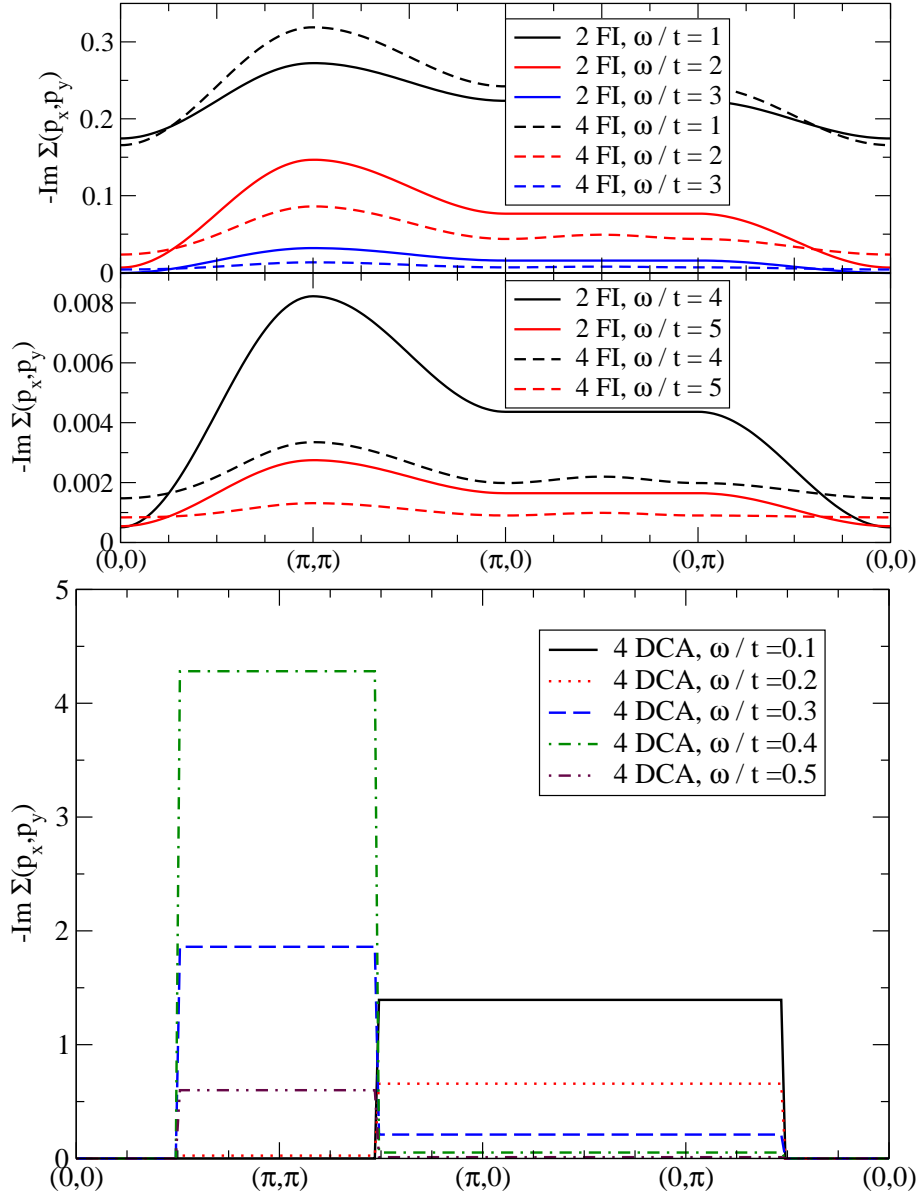
Figure 1.11: Self-energy in the Brillouin zone at $U/t = 16$ and $T/t = 0.3$. The two-dimensional picture is replaced by the one-dimensional plot, using momentums on the line in the Brillouin zone, which connects the points $(0,0)$, (π,π), $(\pi,0)$, $(0,\pi)$, and $(0,0)$. Upper panel: 2- and 4-site real space method for the frequencies $\omega/t = 1, 2, 3, 4$, and 5. Lower panel: 4-site DCA for the frequencies $\omega/t = 0.1, 0.2, 0.3, 0.4$, and 0.5.
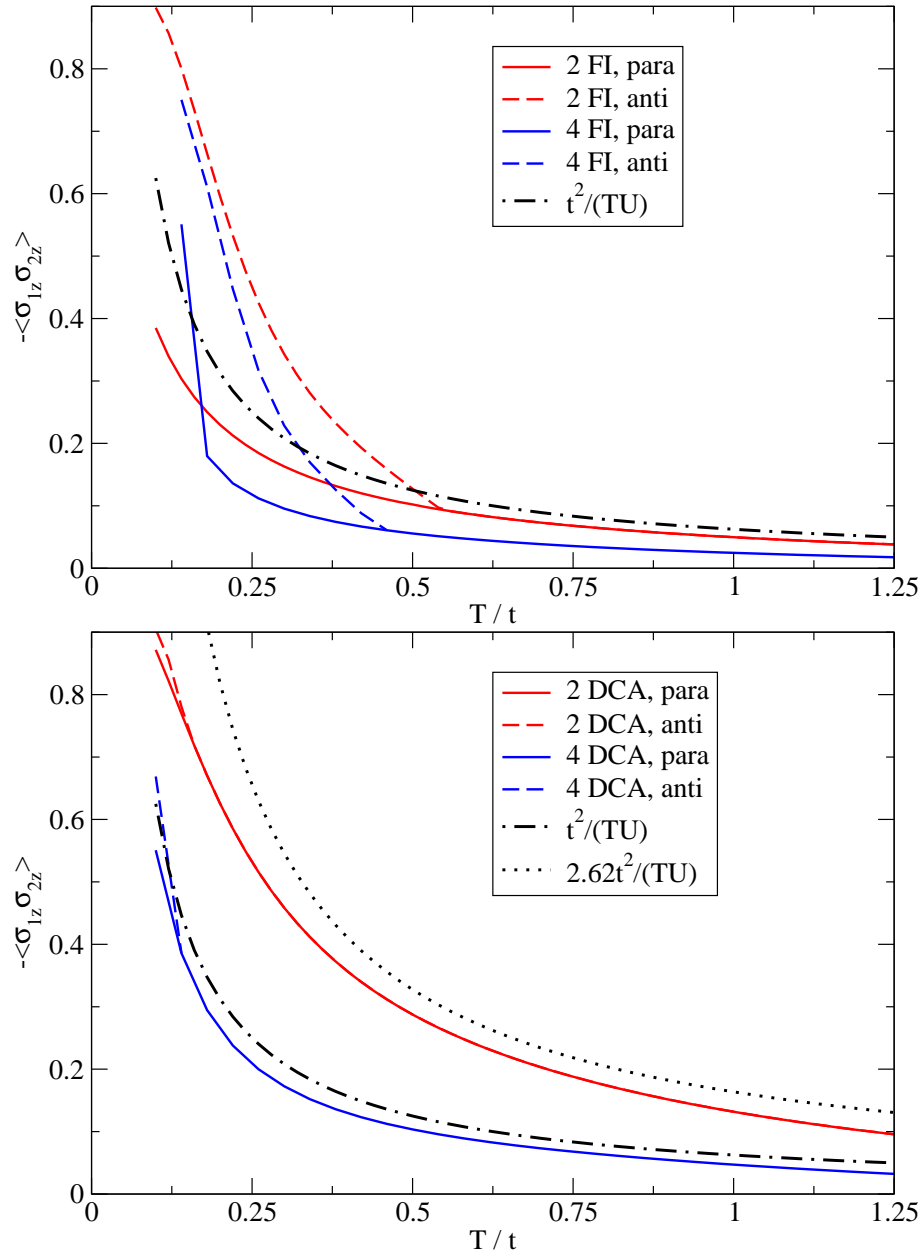
Figure 1.12: NN spin-spin correlation as a function of the temperature obtained using FI method (upper panel) and DCA (lower panel) at $U/t = 16$. Increasing size of the cluster does not cause an improvement in FI method relatively to the approximate curve.

significant difference of the magnitude between 2-site FI and DCA curves was explained by the approximate analysis (subsection 1.4.3), which predicts $-\langle\sigma_{1z}\sigma_{2z}\rangle_{\mathrm{FI}} \approx t^2/(TU)$ and $-\langle\sigma_{1z}\sigma_{2z}\rangle_{\mathrm{DCA}} \approx 2.62t^2/(TU)$. Increasing cluster size (4 sites) improves agreement with the second order approximation in the DCA case, but a stronger underestimation of the nearest neighbor spin-spin correlation was observed in the FI method.

The split of the paramagnetic and of the antiferromagnetic solutions points to the Néel temperature. Both methods shows, that the critical temperature in the 4-site calculation is in general slightly lower than in the 2-site one (see also subsection 1.5.5).

Further we observe a discontinuity in the 4-site FI curve with suppressed Néel phase (the discontinuity is more clear in Figure 1.13). The same behavior was registered in the internal energy (compare Fig. 1.14). A discontinuity in the energy denotes a skip in the first derivative of the grand canonical potential Ω (equation 1.36), which points to the first order phase transition [37]; probably this is a transition to the dimerized spin state. Such transition was not observed in the DCA calculations, therefore we expect it at the lower temperature. Again the kink in the antiferromagnetic curve denotes a second order phase transition at the Néel temperature.

Next nearest neighbor spin-spin correlation   In our study we also consider the next nearest neighbor spin-spin correlation. Figure 1.13 depicts $\langle\sigma_{1z}\sigma_{3z}\rangle$ and $-\langle\sigma_{1z}\sigma_{2z}\rangle$ as a function of temperature. The real space method provides results comparable with results expected from a physical cluster: The fact that site 1 and site 3 lie on the same sublattice[14] explanes the sign opposite to the sign of the NN-curve, where the site 1 and the site 2 lie on the different sublattices. The absolute values of both curves are approximately identical at low temperatures, where the thermal excitations can be neglected. An increasing of the temperature causes a decay, where the NNN-curve falls significantly faster, pointing to the more stable singulet coupling. As anticipated, both para-anti-splits take place at the same temperature. The discontinuity in the fully frustrated solution was discussed in previous paragraph.

1.5.4   Internal Energy

Now we consider an internal energy computed from equation (1.35). The numerical data were compared to the analytical large-U results, which have been obtained up to $\mathcal{O}\left(t^6/(T^2U^3)\right)$ (analytical calculation is briefly presented in section A.2). Internal energy as a function of the temperature at $U/t = 16$ is shown in Figure 1.14 for the real space method (upper panel) and for the DCA (lower panel). Note, the plotted data give the energy *per spin*, *without* a Hartree term, in other words we see $(E + U/4)/2$. We show the paramagnetic and the antiferromagnetic solution for both approaches. The Néel temperature can be identified as a temperature which corresponds to the kink in the $E(T)$ curve. At $T < T_N$ one can see a split, where lower kurve is the antiferromagnetic solution, and the upper kurve is the paramagnetic one, which was obtained by the suppressed

---

[14]In the antiferromagnetic state the quadratic lattice can be split in a $\uparrow$- and a $\downarrow$-sublattice.
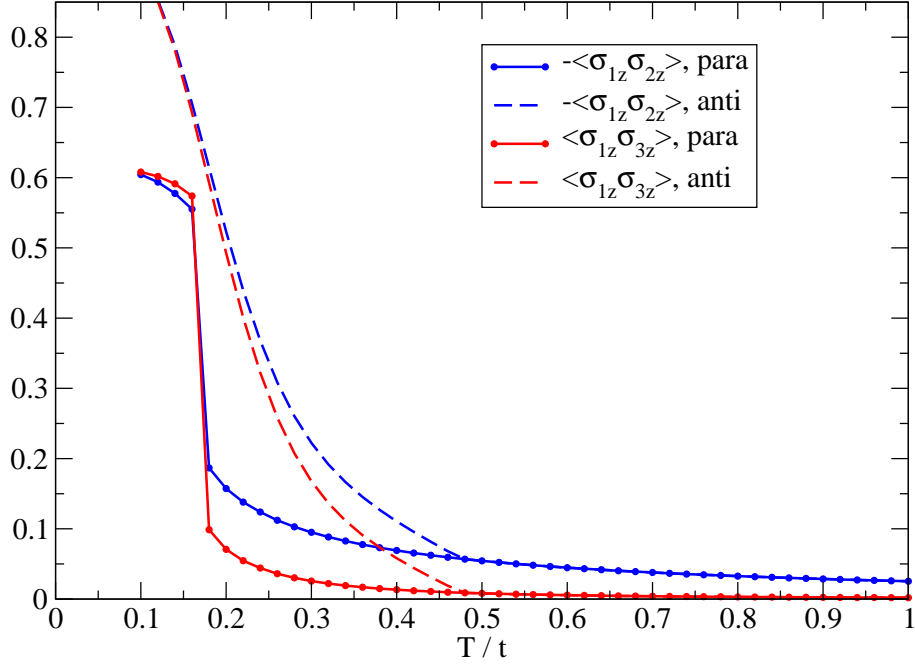
Figure 1.13: NN and NNN spin-spin correlations as a function of temperature obtained by FI method using sum-SCA at $U/t = 16$. The NNN spin-spin correlation function has an opposite sign and decays faster than NN one.

antiferromagnetism.

Three temperature regimes can be viewed: a high temperature regime ($T/t > 0.7$) where the energy increases with growing T, an intermediate regime ($0.5 < T/t < 0.7$) where the energy is independent from the temperature, and a low temperature regime ($T/t < 0.5$) with strong T-dependency.

Due to the real thermal excitations over the Mott-Hubbard gap (at higher temperatures the Fermi edge smears and overlaps with the upper Hubbard band), we observe a strong growth of the energy in high-T regime. The more cliffy sloap of the DMFT results compared to the series expansion is a side-effect of the semiclassical approximation, which overestimates the thermal fluctuations on the gap.

In the T-independent regime, where the Fermi function does not overlap with the upper Hubbard band, we observe a pretty good agreement of the second order expansion curve and the energy from single impurity DMFT, where the energy per spin is equal to $K_2/(4U) = 0.0625$ (compare equation (1.109)). Both FI and DCA results for 2- and 4-site cluster deviate from the second order curve because of the intersite spin correlations. Both FI curves lie above and the DCA results under the single site solution. The 2-site DCA curve is closest to the analytical fourth order curve. The approximate analysis of the 2-site models (subsection 1.4.3) predicts such behavior, where the intersite spin-spin correlations cause a shift of the energy, where the 2-site DCA shift has "correct" sign. We register, that an increasing cluster size generally improves the real space result, but
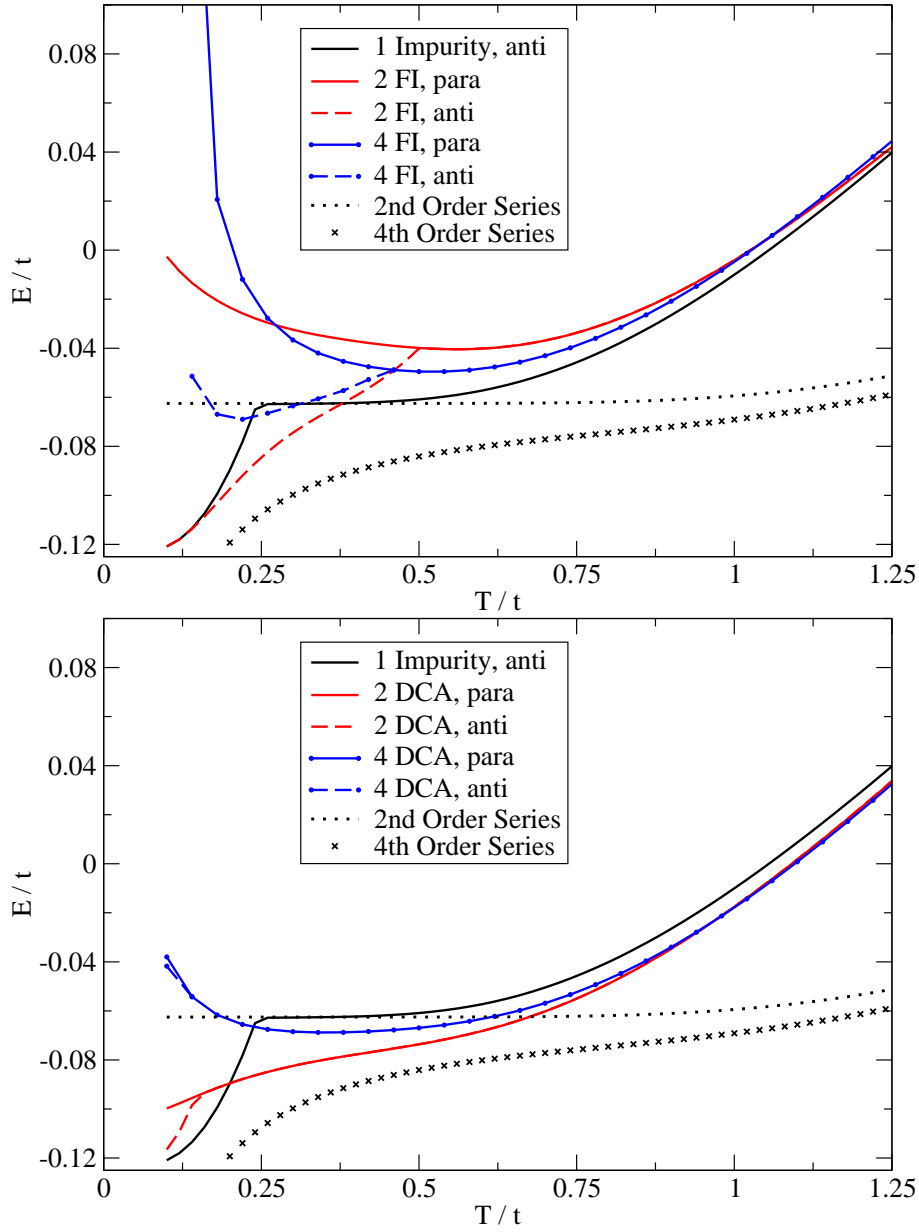
Figure 1.14: Internal energy per spin as a function of the temperature obtained by the FI method (upper panel) and by the DCA (lower panel) at $U/t = 16$ and compared to the analytical results.
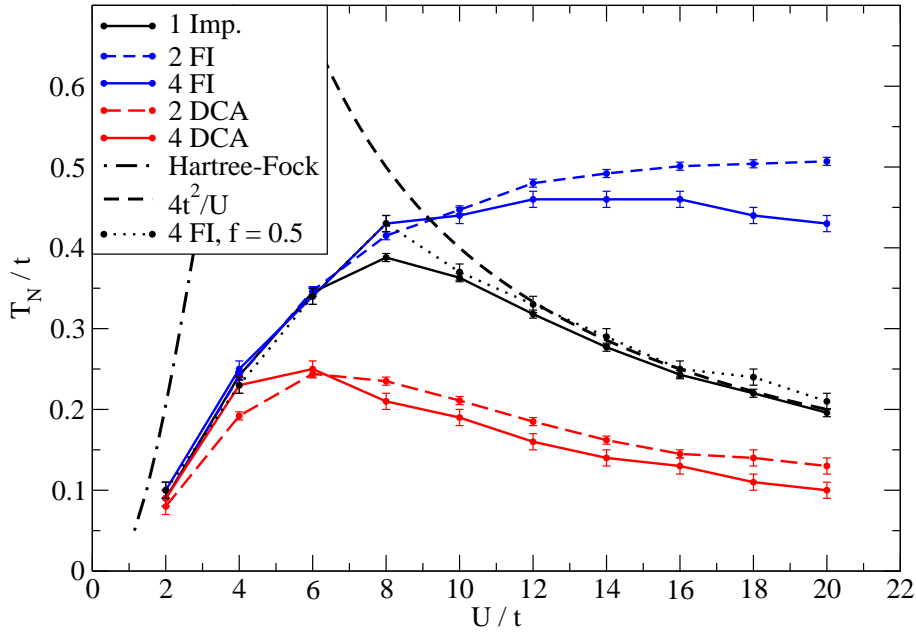
Figure 1.15: The Néel temperature to the 1-, 2-, 4-site clusters computed using FI method and DCA. Also included a large-U and Hartree-Fock approximations. The dotted line corresponds to the 4-site FI result with the filtering parameter $f = 0.5$ (for details see text).

downgrades the developing of the DCA energy.

1.5.5 Néel Temperature

In order to determine a transition temperature between the paramagnetic and the antiferromagnetic states we study the devolution of the energy curve. Because of the second order phase transition the Néel temperature was identified as the temperature, which corresponds to the kink in the antiferromagnetic energy curve.

The resulting phase diagram is shown in Fig. 1.15, where the Néel temperature was determined using the integral-SCA as impurity solver. The closeness of the single-impurity curve to the low-U Hartree-Fock and to the large-U analytical curve points to the correct behavior in low and high interaction limits. The Néel temperature calculated using real space method shows a perfect agreement with the single-site curve in the weak interaction regime $U/t \leq 6$, however the increasing Coulomb repulsion causes the growth of the difference. The DCA curves have generally significantly smaller amplitude than the single site solution, and the agreement was achieved at low interaction ($U/t < 4$) only. Unfortunately, the Néel temperature computed using FI method is strongly overestimated in the large-U regime and the convergency to the analytical result is pretty slow. However, the increasing size of the cluster causes an impovement of the result in the fictive impurity method only. Further we remark, that our low-U results are in reasonable agreement with
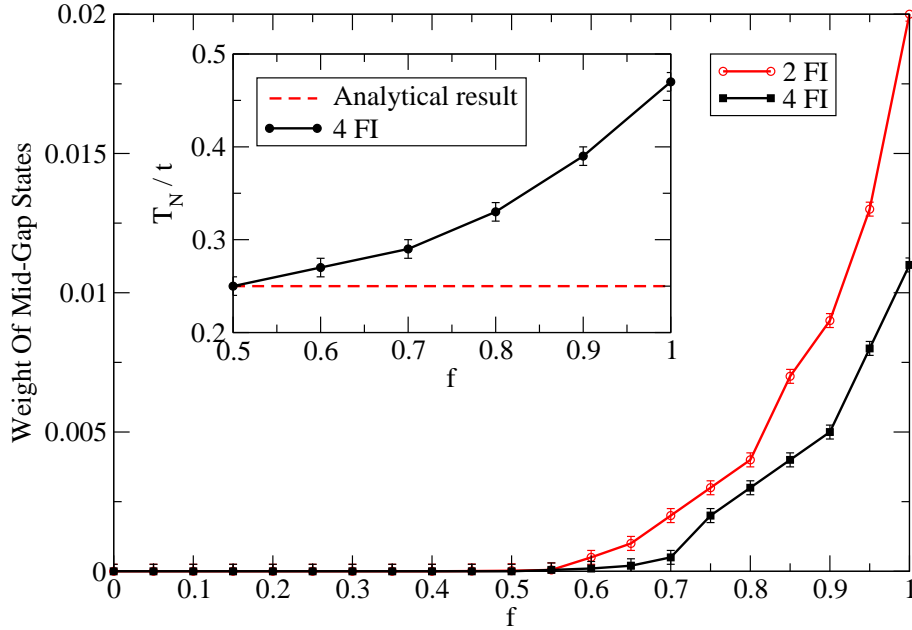
Figure 1.16: Weight of the mid-gap states in the multi-site FI case as a function of filtering at $U/t = 16$ and $T/t = 0.3$. Inset: Néel temperature as a function of filtering in the cluster of 4 fictive impurities is compared to the Néel temperature calculated for the single-site DMFT at $U/t = 16$. Here we have used the sum-SCA as impurity solver.

a low-U study by Jarrel et al. [38].

1.5.6 Filtering

In order to inspect the effect of the mid-gap states on the transition temperature T_N, we have investigated the weight of mid-gap states as a function of filtering (see subsection 1.2.1). Using filtering parameter $f = f_1 = f_2$, with $f \in [0, 1]$ we obtain the following picture (Figure 1.16): The weight of the mid-gap states declines nearly exponentially and we see absolute disappearance at $f = 0.55$ and $f = 0.60$ for 2- and 4-site cluster respectively. The devolution of the Néel temperature as a function of filtering at $U/t = 16$ is presented in the inset. The Néel temperature in the 4-site system achieve the single-site value at $f \approx 0.5$ slightly under the dissappearance-temperature of the mid-gap states, denoting a direct connection between the zero-frequency states and the overestimation of the Néel temperature at large-U.

Due to the fact, that the weight of the mid-gap states decreases when the cluster size increases, we have tried to imitate a large-N_C cluster using a 4-site cluster and the filtering $f = 0.5$. It was found, that the Néel temperature curve is in accordance with the analytical result (compare Fig. 1.15, dotted line). We interpret this result as a ratification of the fictive impurity method, especially by the consideration of the $N_C > 4$ clusters.

1.6   Conclusion

Finishing the present part of the work we consolidate our findings:

1. A recently developed semiclassical impurity solver for dynamical mean fiel theory was investigated at a wide range of the Coulomb repulsion and compared to the well known Quantum Monte Carlo algorithm. We have found, that the numerical data calculated using semiclassical approximation is consistent with the QMC results, especially in the antiferromagnetic regime. An advantage of the SCA is an enormous saving of the computational time (up to twenty times) in the large-U regime, which is crucial for the investigations of the multi-site clusters at finite temperature. An other point of interest of the numerical part was the examination of the sum-SCA versus integral-SCA. It was found that in the large-U regime ($U/t > 12$) the sum-SCA is significantly faster than the integral-SCA, whereas the difference of results is negligible. Unfortunately the sum-SCA breaks down in low repulsion regime, therefore we should use the integral-SCA in that region.

2. In order to compare our numerical results we have calculated approximate analytical results for both real space method and dynamical cluster approximation in the large-U and low-T regime. The strong coupling limit approximation explanes some strange-looking results computed in the present work. The low-temperature regime allowes to neglect the real inter-Hubbard-band excitations and to consider the virtual excursions of a fermion only, so the result still depends on the intersite correlations. We found that all approaches reproduce the leading order $\mathcal{O}(t^2/U)$ result for the internal energy exactly, but the next order contribution $\mathcal{O}(t^4/(TU^2))$, which includes intersite correlations, leads to the unphysical behavior. An early examination of the possible multi-site extensions of the DMFT by Schiller and Ingersent [39] has suggested that the straightforward cluster methods (such as the fictive impurity method) are fundamentally wrong, because they double-count processes involving the hopping of an electron from site to site. It is seen in our results, that the cluster methods have some troubles, but the fundamental overcounting is not the problem of the cluster methods considered in this work.

3. We have studied the multi-site extensions of the dynamical mean field theory. A set of physical quantities, such as self-energy, spin-spin correlation, internal energy, Néel temperature, and other were computed. We have found that neither the fictive impurity method nor the dynamical cluster approximation yields completely correct physical results. Both methods over- or underestimate the Néel temperature and do not evaluate other physical quantities completely correctly. We have shown that the increasing size of the cluster causes an improvement of the FI results, which is not the case in the dynamical cluster approximation. Also we have found, that the FI method provides some unphysical mid-gap states in the Mott-insulating phase. The weight of these states depends on the cluster-size and can be easily removed by a filtering procedure.

4. A possible source of error in the real space method is the assumption that all nearest neighbor (NNN, ...) self-energies can be collapsed into one function. Probably each self-energy contribution should be treated as an independent function, which was impossible in this work because of the huge computational time effort. Also it should be interesting for the future investigations to include an additional term $J \sim t^2/U$ in the impurity models, which will correct the effect of the intersite correlations. Moreover the FI method and the cellular DMFT should be compared too.

Chapter 2

Two-Plane Hubbard Model

2.1 Introduction

The discovery of the high T_C-superconductivity in 1986 sets off an avalanche of experimental and theoretical investigations on this field. The analysis of the crystal structure has shown that most of the high T_C crystals include CuO-chains and CuO-planes in there structure. The growing theoretical basis [40, 41] inducts the series of the nuclear magnetic resonance and the nuclear quadrupole resonance experiments with $Y_2Ba_2Cu_7O_{15}$-crystals [42, 43]. It was found that such crystals consist of $YBa_2Cu_3O_7$- and $YBa_2Cu_3O_8$-layers, which contain the CuO-plane pairs. The later experiments by Fukuzumi et al. [44] pointed to the conductivity in the YBa-superconductors is 3-dimensional. Also, there are some unusual aspects in the behavior of the high temperature superconductors' transport properties. In his earlier works [45, 46], Anderson has accented the difference between the transport properties in a CuO-plane and the inter-plane transport. The photoemission experiments [47, 48] in $YBCO$ show only small if any difference between bonding and anti-bonding CuO-plane bands as a result of the hopping between the CuO-planes, which is unexpected due to the relatively large value of the inter-plane hopping matrix element $t_\perp \approx 0.3\text{eV}$ compared to $t \approx 1\text{eV}$, obtained from the band structure calculations [49]. The experimental data were interpreted as absence of coherent quasi-holes in the CuO-plane [46].

In the present work we investigate the phase diagram of a two-plane Hubbard model–the simplest system displaying a metal-to-band insulator transition competing with a Mott transition. In fact, the nature of the metallic phase as well as the properties of the phase transitions change drastically between one and three dimensions, which caused wide interest in the studies of the dimensional crossovers and behaviors of the coupled low-dimensional systems in the last years [50, 51, 52, 53]. In addition to the earlier works [54, 55, 56, 57] and to the current research [58, 59, 60, 61, 62, 63], we consider the transition from the Mott insulator to the band insulator phase and try to understand is it a crossover or a clear phase transition. In an earlier publication [64], Moeller et al. treated a two-plane Hubbard model in infinite dimensions and found the zero-temperature phase diagram using dynamical mean field theory (DMFT) and iterated perturbation
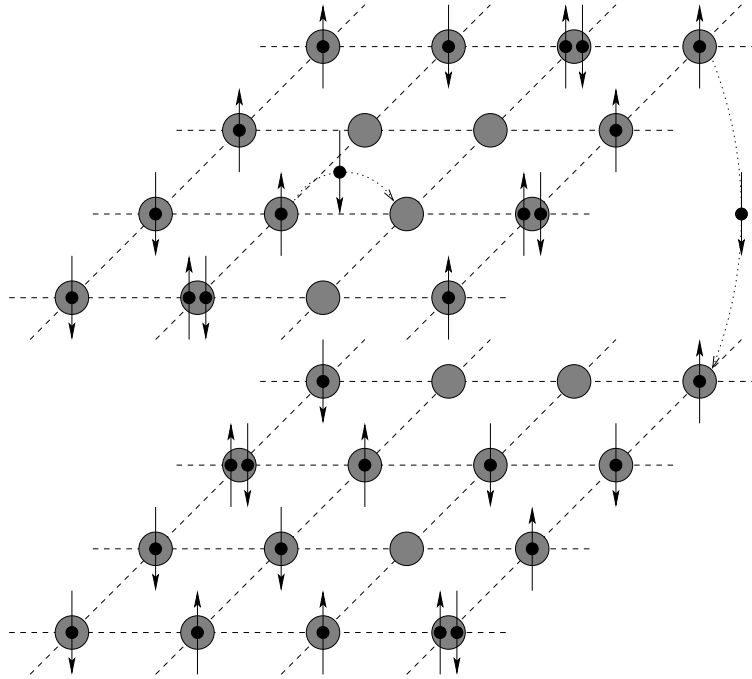
Figure 2.1: Two connected quadratic half-filled lattices (draft). Black circles with arrows symbolize fermions with corresponding orientation of the spin's z-component. The fermions hope between neighboring sites or between *corresponding* sites of both lattices.

theory (IPT). In contrast to this work we use the Quantum Monte Carlo (QMC) method in order to solve the DMFT equations at *finite* temperature without any uncontrolled approximations. In addition to existing publications, we calculate the optical conductivity of a two-plane system, find the Drude weight and other spectral properties.

The rest of this chapter is organized as follows: Section 2.2 presents the model, the solution method and the analytical consideration of the optical conductivity. Section 2.3 gives numerical details which were used in this part of the work but were not discussed in the first chapter. The impurity solver used in the present chapter is the Quantum Monte Carlo algorithm, which can be found in section 1.3 The numerical results are presented in section 2.4, and the resume can be found in 2.5.

2.2 Analytical Approach

2.2.1 Model

We consider a Hubbard model on two coupled quadratic lattices, the inter-plane Coulomb interaction is neglected. The fermions move inside the lattice by hopping between the neighboring sites as well as between the corresponding sites of both planes (Fig. 2.1). The Hamiltonian is defined as

$$H = - \sum_{\langle i,j \rangle \sigma \alpha} t_{ij} c^{\dagger}_{i\sigma\alpha} c_{j\sigma\alpha} - t_{\perp} \sum_{i\sigma\alpha} c^{\dagger}_{i\sigma\alpha} c_{j\sigma(1-\alpha)} + U \sum_{i\alpha} n_{i\uparrow\alpha} n_{i\downarrow\alpha}, \qquad (2.1)$$

where $c^{\dagger}_{i\sigma\alpha}$ ($c_{i\sigma\alpha}$) is an operator, which creates (annihilates) a fermion with spin σ on ith site of the plane $\alpha \in \{0,1\}$; the operator $n_{i\sigma\alpha}$ gives the number of particles with spin σ at site (i, α). The hopping amplitude between neighboring sites is t_{ij}, and $t_{\perp}$ between corresponding sites of both planes.

2.2.2 Solution Method

The problem was solved using dynamical mean field theory (DMFT) [4], where the 2-plane system was reduced to two impurities self-consistently embedded in a bath. The solution of the 2-impurity problem, calculated by Hirsch-Fye QMC, yields an impurity Green functions, which was used to obtain the self-energy for the DMFT equations. The Dyson equation gives the new Weiss field for the 2-impurity problem. The upper steps were repeated until a convergent solution was found.

In details, the algorithm is the following: We start with a Weiss field

$$\hat{a}_{\sigma}(\omega_n) = \begin{pmatrix} a_{00\sigma} & a_{01\sigma} \\ a_{10\sigma} & a_{11\sigma} \end{pmatrix}, \qquad (2.2)$$

which is defined as

$$\hat{a}^{-1}_{\sigma}(\omega_n) = \int d\varepsilon D(\varepsilon) \left((i\omega_n + \mu - \varepsilon)\hat{1} - \hat{t}_{\perp} \right)^{-1}, \qquad (2.3)$$

where

$$\hat{t}_{\perp} = \begin{pmatrix} 0 & t_{\perp} \\ t_{\perp} & 0 \end{pmatrix}; \qquad (2.4)$$

we use the semicircular density of states $D(\varepsilon) = \sqrt{4t^2 - \varepsilon^2}/(2\pi t^2)$, with $t = 2t_{ij}$ in this chapter. The inverse Fourier transformation leads to the Weiss field as a function of the imaginary time and using the effective action

$$S_{\text{eff}} = \sum_{\sigma} \int_0^{\beta} d\tau \int_0^{\beta} d\tau' c^{\dagger}_{\sigma}(\tau) \hat{a}_{\sigma}(\tau, \tau') c_{\sigma}(\tau') + \int_0^{\beta} d\tau U n_{\uparrow}(\tau) n_{\downarrow}(\tau), \qquad (2.5)$$

with $c_{\sigma} = \begin{pmatrix} c_{0\sigma} \\ c_{1\sigma} \end{pmatrix}$ and $n_{\sigma} = c^{\dagger}_{\sigma} c_{\sigma}$; we solve the 2-impurity problem by the Quantum Monte Carlo algorithm (see section 1.3). The following Fourier transformation yields the impurity Green function $\hat{G}_{\text{imp}\,\sigma}(\omega_n)$. The diagonal elements $G_{\text{imp}\,00\sigma}(\omega_n)$ and $G_{\text{imp}\,11\sigma}(\omega_n)$ give the on-site Green functions for the corresponding planes, and the off-diagonal elements $G_{\text{imp}\,01\sigma}(\omega_n)$ and $G_{\text{imp}\,10\sigma}(\omega_n)$ give the Green functions connecting two corresponding sites on different planes. By the Dyson equation we easily obtain the self-energy

$$\hat{\Sigma}_{\sigma}(\omega_n) = \hat{a}_{\sigma}(\omega_n) - \hat{G}^{-1}_{\text{imp}\,\sigma}(\omega_n), \qquad (2.6)$$

and then we perform the DMFT equation

$$\hat{a}_\sigma(\omega_n) = \Sigma_\sigma(\omega_n) + \tilde{D}_\sigma^{-1}(\omega_n), \tag{2.7}$$

which gives the new Weiss field for the 2-impurity problem. In equation (2.7), we used

$$\tilde{D}_\sigma(\omega_n) = \int d\varepsilon D(\varepsilon) \left((i\omega_n + \mu - \varepsilon)\hat{1} - \hat{t}_\perp - \hat{\Sigma}_\sigma(\omega_n) \right)^{-1}, \tag{2.8}$$

with

$$\hat{\Sigma}_\sigma(\omega_n) = \begin{pmatrix} \Sigma_{00\sigma} & \Sigma_{01\sigma} \\ \Sigma_{10\sigma} & \Sigma_{11\sigma} \end{pmatrix}. \tag{2.9}$$

The chemical potential μ is equal 0, and the self-energies satisfy $\Sigma_{00\sigma}(\omega_n) = \Sigma_{11\sigma}(\omega_n)$ and $\Sigma_{01\sigma}(\omega_n) = \Sigma_{10\sigma}(\omega_n)$ because we consider identical planes (impurities).

With the exception of the QMC part, the algorithm was calculated in the symmetric/antisymmetric basis which was achieved by the left- and right-multiplication of the equations (2.6) and (2.7) with the matrix

$$A = \frac{1}{\sqrt{2}} \begin{pmatrix} 1 & 1 \\ 1 & -1 \end{pmatrix}. \tag{2.10}$$

According to this transformation the self-energy now is $\Sigma_{S/A\sigma}(\omega_n) = \Sigma_{0\sigma}(\omega_n) \pm \Sigma_{1\sigma}(\omega_n)$ and the Hilbert transformed density of states becomes diagonal

$$\tilde{D}_\sigma(\omega_n) = \begin{pmatrix} \tilde{D}_{S\sigma}(\omega_n) & 0 \\ 0 & \tilde{D}_{A\sigma}(\omega_n) \end{pmatrix}, \tag{2.11}$$

where the matrix elements are defined as

$$\tilde{D}_{S/A\sigma}(\omega_n) = \int d\varepsilon D(\varepsilon) \left(i\omega_n + \mu - \varepsilon \mp t_\perp - \Sigma_{S/A\sigma}(\omega_n) \right)^{-1}. \tag{2.12}$$

In current the chapter we consider fully a frustrated lattice, therefore the antiferromagnetism was artificially suppressed.

2.2.3 Optical Conductivity And Drude Weight

In order to gain insight about the transport properties of the considering system, we calculated the optical conductivity as well as the Drude weight in the $U - t_\perp$-space.

The optical conductivity for the simple cubic lattice in the limit $d \to \infty$ can be expressed as a function of the current-current correlator [65]

$$\begin{aligned}
\tilde{\sigma}(i\nu) &= \frac{1}{\nu\beta} \sum_{\omega_n} \int_{-\infty}^\infty d\varepsilon D(\varepsilon) G(\varepsilon, i\omega_n) G(\varepsilon, i\omega_n + i\nu) \\
&= \frac{1}{\nu} \int_{-\infty}^\infty d\varepsilon D(\varepsilon) \int_{-\infty}^\infty d\omega \int_{-\infty}^\infty d\omega' A(\varepsilon, \omega) A(\varepsilon, \omega') \frac{f(\omega) - f(\omega')}{\omega - \omega' + i\nu}.
\end{aligned} \tag{2.13}$$

$D(\varepsilon)$ is the free particle density of states and $f(\omega) = (1+\exp(\beta\omega))^{-1}$ is the Fermi function. In equation (2.13) we used $G(\varepsilon, i\omega_n) = \int_{-\infty}^{\infty} d\omega \frac{A(\varepsilon,\omega)}{i\omega_n - \omega}$ and $f(\omega) = \frac{1}{\beta} \sum_n \frac{1}{i\omega_n - \omega}$. The real part of the analytical continuation of equation (2.13) is the optical conductivity[1]

$$\sigma(\omega) = \pi \int_{-\infty}^{\infty} d\omega' \int_{-\infty}^{\infty} d\varepsilon D(\varepsilon) A(\varepsilon, \omega') A(\varepsilon, \omega' + \omega) \frac{f(\omega') - f(\omega' + \omega)}{\omega} \tag{2.14}$$

in which we are interested. The missing constants yield a factor

$$\sigma_0 = \frac{\pi e^2 t^2}{2a\hbar} \approx 0.001 \ldots 0.01 \frac{1}{\mu\Omega cm}, \tag{2.15}$$

where a is the lattice constant and $t \approx 1eV$ is the hopping amplitude. Switching over to the two-plane Hubbard model, the optical conductivity should be modified to

$$\sigma(\omega) = \sigma_0 \sum_{\alpha=S,A} \int_{-\infty}^{\infty} d\omega' \int_{-\infty}^{\infty} d\varepsilon D(\varepsilon) A_\alpha(\varepsilon, \omega') A_\alpha(\varepsilon, \omega' + \omega) \frac{f(\omega') - f(\omega' + \omega)}{\omega}, \tag{2.16}$$

where

$$A_\alpha(\varepsilon, \omega) = -\frac{1}{\pi} \mathrm{Im} G_\alpha(\varepsilon, \omega), \tag{2.17}$$

The summation over symmetric and antisymmetric planes in equation (2.16) matters the following: the optical conductivity is defined in the long-wave limit ($\boldsymbol{E}$ is nearly homogeneous), so the in-plane as well as the inter-plane momentum transferred by the optical conductivity should be zero. The inter-plane component of momentum can assume only two values, 0 and π/a, where a is the inter-plane distance, corresponding to symmetric and antisymmetric orbitals, respectively. Therefore the optical conductivity at vanishing momentum is given by the product of both symmetric or both antisymmetric Green functions. [66, 67]. The constant σ_0 was set to unity in this work.

The Drude weight, was identified with the weight of the central peak of the optical conductivity, which is finite in the metallic phase and vanishes in the insulating state.

2.3 Numerical Techniques

There are two main techniques that we used in the present chapter: the 2-impurity problem was solved using the Hirsch-Fye Quantum Monte Carlo method and the analytical continuation was performed by the maximum entropy data analysis. The Quantum Monte Carlo algorithm was described in detail in section 1.3.2. The maximum entropy data analysis program was coded according to the works by Skilling [31], Von den Linden [29, 30], and Jarrell et al. [32]. The detailed algorithm can be found i. a. by Fuhrmann diploma theses [33]. The technical sophistication applied in this part of the work as well as some useful technical tips are presented in the current section.

---

[1]We use $\frac{1}{\omega-(\omega'+\nu+i0)} = P.P.\frac{1}{\omega-(\omega'+\nu)} + i\pi\delta(\omega - (\omega' + \nu))$.

2.3.1 Technical Details

Maximum entropy data analysis The maximum entropy procedure was used for the analytical continuation of fermionic functions according to the equation

$$G(\tau) = \int_{-\infty}^{\infty} d\omega \frac{A(\omega)\exp(-\tau\omega)}{1+\exp(-\beta\omega)}, \tag{2.18}$$

where τ is the imaginary time. One of the most important issues in the ME procedure is the choice of the default model which should have a similarity with the actual density of states. The analytical considerations yield information about the DOS at $(U/t = 0, t_\perp/t > 0)$ and at $(U > U_C, t_\perp/t = 0)$, which motivates us to use the following default model

$$m_{S/A}(\omega) = \begin{cases} \frac{2}{\pi R^2}\sqrt{R^2-(\omega \pm t_\perp)^2} & \text{if } |\omega \pm t_\perp| < R \\ 10^{-5}/t & \text{else}, \end{cases} \tag{2.19}$$

with $R = \frac{1}{2}U + 2t$, where U is the Coulomb repulsion. The bandwidth of the upper default model is $2R$, which corresponds to the width of the free density of states at $U/t = 0$; also it is centered at $\mp t_\perp$ in the symmetric/ antisymmetric case. The traditional Gauss curve was unusable due to the long tails, which leads to the non-physical results in the band transition region.

Optical conductivity The optical conductivity (2.16) was computed according to the procedure, published in the PhD. theses by Blümer [28]. Here we show the main features of this algorithm:

1. The analytical continuation of $G_\alpha^{\text{Imp}}(\tau)$ yields the imaginary part of the impurity Green function on the real axis

$$\text{Im}\, G_\alpha^{\text{Imp}}(\omega) = -\pi A_\alpha(\omega). \tag{2.20}$$

2. The Kramers-Kronig relation leads to the real part of the impurity Green function

$$\text{Re}\, G_\alpha^{\text{Imp}}(\omega) = P.P. \int_{-\infty}^{\infty} \frac{d\omega'}{\pi} \frac{\text{Im}\, G_\alpha^{\text{Imp}}(\omega')}{\omega' - \omega}. \tag{2.21}$$

3. The semi-elliptic density of states used in the present work allows the analytical performance of the ε integrated Dyson equation, which give us the lattice Green function

$$G_\alpha(\omega) = \frac{1}{2}\left(z_\alpha(\omega) - \sqrt{z_\alpha^2(\omega)-4}\right), \tag{2.22}$$

with $z_{S/A}(\omega) = \omega \mp t_\perp - \Sigma_{S/A}(\omega)$. Some manipulations of the upper equation give us the real frequency self-energy

$$\Sigma_{S/A}(\omega) = \omega \mp t_\perp - G_{S/A}(\omega) - 1/G_{S/A}(\omega). \tag{2.23}$$

4. Finally we calculate the A_α needed in equation (2.16)

$$A_{S/A}(\varepsilon, \omega) = \frac{1}{\omega - \varepsilon \mp t_\perp - \Sigma_{S/A}(\omega)}. \tag{2.24}$$

Note, in order to get qualitative results for the optical conductivity, one should interpolate and refine the numerical data computed using maximum entropy data analysis. The $\Delta\omega/t = 0.0125$ used in our work gave sufficient fineness for extrapolation of the optical conductivity up to $\omega/t = 0$ as well as for the determination of the Drude weight.

Parallel to the numerical schema suggested by Blümer we have tried to develop an alternative schema to compute the optical conductivity. The main idea was to obtain the optical conductivity as a function of bosonic Matsubara frequencies and then to perform the analytical continuation [68]. The following algorithm was developed:

1. Due to the divergent term $1/\nu$ (compare first line in (2.13)) we figured out the "bubble" part as a function of bosonic Matsubara frequencies

$$G_{jj}(i\nu_m) = \int_{-\infty}^{\infty} d\varepsilon D(\varepsilon) \frac{1}{\beta} \sum_{\omega_n} G(\varepsilon, i\omega_n) G(\varepsilon, i\omega_n + i\nu_m), \tag{2.25}$$

where the sum should be performed very carefully, especially at large frequencies.

2. The following Fourier transformation and analytical continuation give $G_{jj}(\nu)$. By reason of the troubles with negative values of the integral core in bosonic case, we considered positive frequencies only, taking advantage of the antisymmetry of $G_{jj}(\nu)$

$$\begin{aligned} G_{jj}(\tau) &= \int_{-\infty}^{\infty} d\omega \frac{G_{jj}(\nu) \exp(-\tau\nu)}{1 - \exp(-\beta\omega)} \\ &= \int_{0}^{\infty} d\omega \left[\frac{G_{jj}(\nu) \exp(-\tau\nu)}{1 - \exp(-\beta\omega)} - \frac{G_{jj}(\nu) \exp(\tau\nu)}{1 - \exp(\beta\omega)} \right]. \end{aligned} \tag{2.26}$$

3. Division by ν gives the optical conductivity.

Our method gives results which are comparable with those from the Blümer method (see Figure 2.2, upper panel). Sadly, it was not possible to determinate the values of the function close to $\nu = 0$ accurately, which is crucial for the finding of the Drude weight. For this reason we went for the first method.

Drude weight The weight of the Drude peak (D) was determined by fitting a Lorentz curve $(L(\omega))$ to the central peak of the optical conductivity. In order to separate the Drude peak from the contribution of the peaks centered at $\omega = U/2$ and $\omega = U$ we only fitted the data points on the interval $[0; 2T]$, where the influence of these peaks is negligible. The Drude weight was calculated by integration of the right half of the Lorentz curve $D = \int_0^\infty d\omega L(\omega)$.
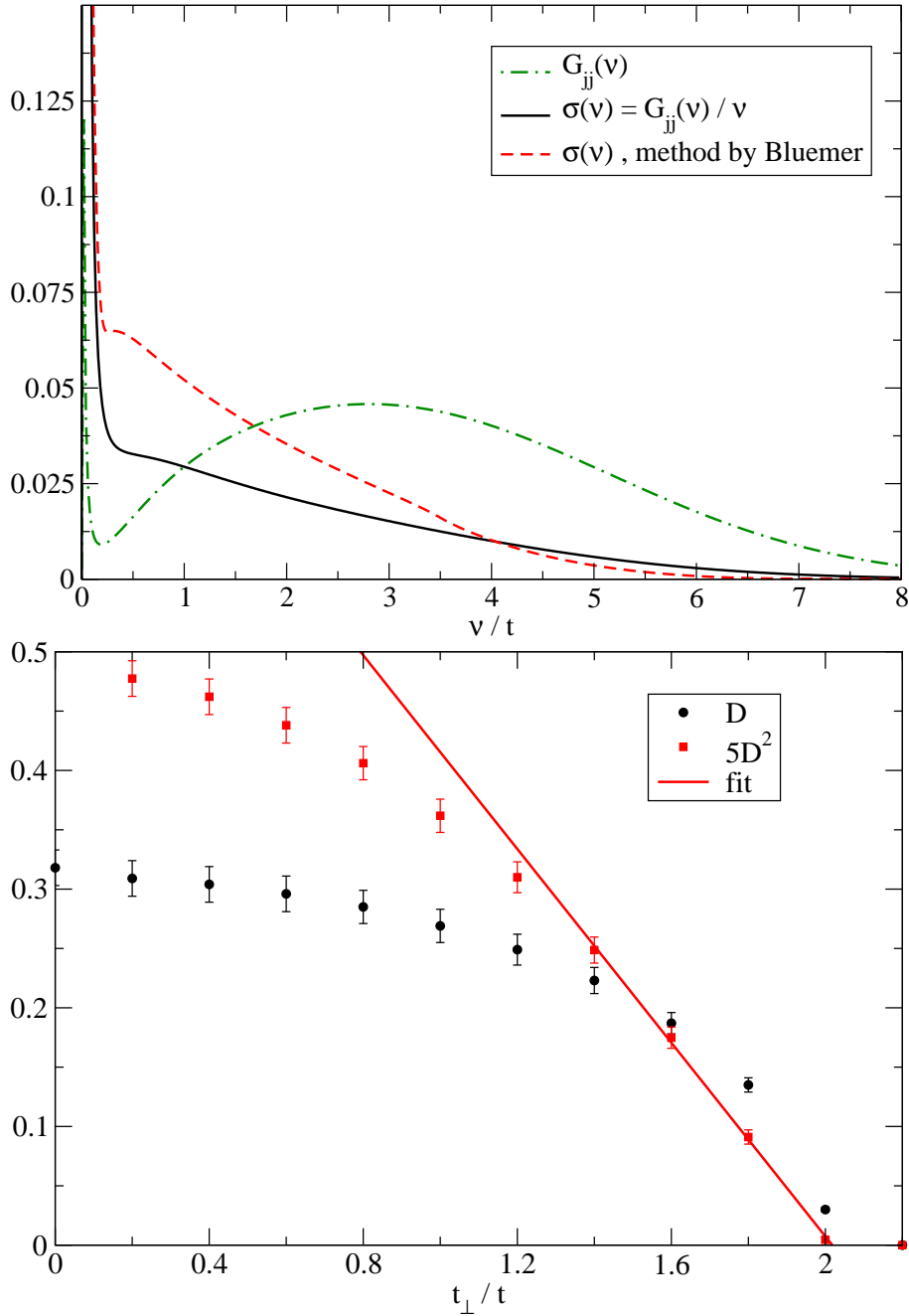
Figure 2.2: Upper panel: Optical conductivity computed using two different methods at $U/t = 3$ and $t_\perp/t = 0$. One can see the "bubble" function (broken-dotted line), out of it following the optical conductivity (solid line), and the optical conductivity computed using the method developed by Blümer. Lower panel: Evolution of the Drude weight and squared Drude weight as a function of $t_\perp$ at $U/t = 0$. The Drude weight vanishes proportional to $\sqrt{t_{\perp C} - t_\perp}$, thus one identifies and fits the linear part of the squared Drude weight, which yields the critical value of $t_{\perp C}$.

The evolution of the Drude weight as a function of the parameter x with $x = U$ or $x = t_\perp$ was crucial for the determination of the metal-to-insulator transition. In general, the Drude weight vanishes in the insulating state and the critical value of x can be easily found. Because of the huge computational effort we were not able to calculate all points in the phase diagram and used a raster with $\Delta U/t = 0.5$ and $\Delta t_\perp/t = 0.2$ which leads to the errors ± 0.25 and ± 0.1 respectively. We found, that in the case of small x the Drude weight vanishes proportionally to $\sqrt{x_C - x}$ allowing us to determine the phase transition with higher accuracy: the squared Drude weight has a linear part close to the phase transition which can be fitted. An example at $U/t = 0$ is depicted on the lower panel of Figure 2.2.

2.4 Numerical Results

In this chapter we present the numerical results computed for the two-plane Hubbard model, where the 2-impurity problem was solved using Hirsch-Fye Quantum Monte Carlo algorithm (see section 1.3.2) at temperature $T/t = 0.025$ at half-filling, the antiferromagnetism was suppressed. The number of imaginary time slices in the QMC algorithm was $L = 100$ and $\Delta\tau = \beta/L = 0.4/t$. The free density of states (DOS) was defined by $D(\varepsilon) = \sqrt{4t^2 - \varepsilon^2}/(2\pi t^2)$, which is an acceptable approximation for the 2 dimensional cubic lattice.

The chapter is organized as follows: at the begin we introduce a 2-plane problem typical DOS at non-zero U and $t_\perp$, the density of states for uncoupled Hubbard planes and the DOS for system without interaction. Then we consider the optical conductivities as well as the Drude weights. The phase diagram completes this section.

2.4.1 Single Particle Density Of States

At the beginning we should note that all following particle densities of states are presented in the symmetric/ antisymmetric basis. Due to the particle-hole symmetry the symmetric and antisymmetric density of states are symmetric relative to the zero frequency, in other words $A_S(\omega) = A_A(-\omega)$, therefore for more clarity we depict *symmetric* DOS only. The transformation to the real space can be easily performed using $A_{0/1}(\omega) = (A_S(\omega) \pm A_A(\omega))/2$.

We start with a system of two decoupled Hubbard planes. The behavior of such a system and of a single Hubbard plane should be identical. The evolution of the symmetric DOS as a function of on-site interaction U is demonstrated in Fig. 2.3 (upper panel). The densities of states at low interaction ($U/t \leq 1$), as expected, show similarity with the free density of states. The DOS at $1 < U/t$ becomes more wide and show the typical three-peak structure Mott transition ($U/t = 4.5$ at $t_\perp/t = 0$). The peak in the middle of the spectrum is the quasiparticle peak and the upper and lower Hubbard bands are located at $+U/2$ and $-U/2$, respectively. The spectral density at $U/t = 4.75$ presents the insulating state just after the vanishing of the quasiparticle peak. The DOS at $U/t = 6$ shows the

lower and upper Hubbard bands in the insulating state. The Mott transition was found at $U/t = 4.70 \pm 0.05$, which is the left border of the coexistence region of the uncoupled system[2]. The coexistence region lies between $U/t = 4.70 \pm 0.05$ and 5.5 ± 0.1 at $t_\perp/t = 0$ and $T/t = 1/40$, which is wider than the coexistence region $[4.70 \pm 0.08; 5.03 \pm 0.01]$ calculated by Blümer [28]. The disagreement of the upper border of the coexistence region might be explained by the relative large discretization ($t\Delta\tau = 0.4$) used in the QMC.

The non-zero inter-plane hopping amplitude causes a shift of the symmetric (antisymmetric) band by exact $-t_\perp$ ($t_\perp$) respectively. The metal-to-band-insulator transition takes place when the overlap of symmetric and antisymmetric DOS vanishes. The critical inter-plane hopping at $U/t = 0$ is equal to the half-bandwidth, which means $t_\perp/t = 2$ in our case. Figure 2.3 (lower panel) confirms the analytical expectation: the symmetric density of states moves left by $t_\perp$ and the overlap with the antisymmetrical DOS (is not depicted) vanishes when $A_S(\omega) = 0$.

Considering the symmetric density of states at finite U and increasing $t_\perp$ we could see the growth of the lower Hubbard band (LHB) and shrinking of the upper Hubbard band (UHB). The whole weight of the symmetric spectral density is concentrated in the LHB at $t_\perp/t > 2$. At the same time the antisymmetric density of states shows the inverse behavior. Figure 2.4 shows the DOSs in the metallic (lower panel) and insulating (upper panel) states at $U/t = 4$. The spectral density at $t_\perp/t = 1.4$ shows composition of pure Mott insulator and pure band insulator, which is typical in this region. This points at the cross-over transition between both insulating states, which will be discussed in detail later in this section.

2.4.2 Optical Conductivity

The optical conductivity (OC), in particular the Drude weight, is a perfect source of information about the state of the system (metal or insulator) as well as about the system's conductivity properties. The $U - t_\perp$ phase diagram, determined in the current work, based on the data obtained from the OC. Therefore it is reasonable to consider the optical conductivity in detail.

At first we considered the optical conductivity of the uncoupled system ($t_\perp/t = 0$). Using equation (2.16) we calculated the optical conductivity at different values of U (Fig. 2.5, upper panel). The shape of the optical conductivity at $U/t = 0.5$ does not distinguish from the OC at $U/t = 0$, which consists of the Drude peak (Lorentz peak) only. The difference can be seen in the weight of the Drude peak (s. inset), that is significantly larger at $U/t = 0$. Increasing interaction ($U/t = 2.0, 3.5, 4.5$) causes displacement of the weight from the Drude peak to a mid-infrared peak and to an incoherent peak at $\omega \approx U/2$ and $\omega \approx U$ respectively. The Drude weight vanishes in the insulating state and the OC is identical with the incoherent peak ($U/t = 5.0, 6.5$). As expected, the devolution of the Drude weight (inset) gives the critical value of interaction at $U/t \approx 4.7$. We note that our results are compatible with the single-plane data calculated by Pruschke et al. [65].

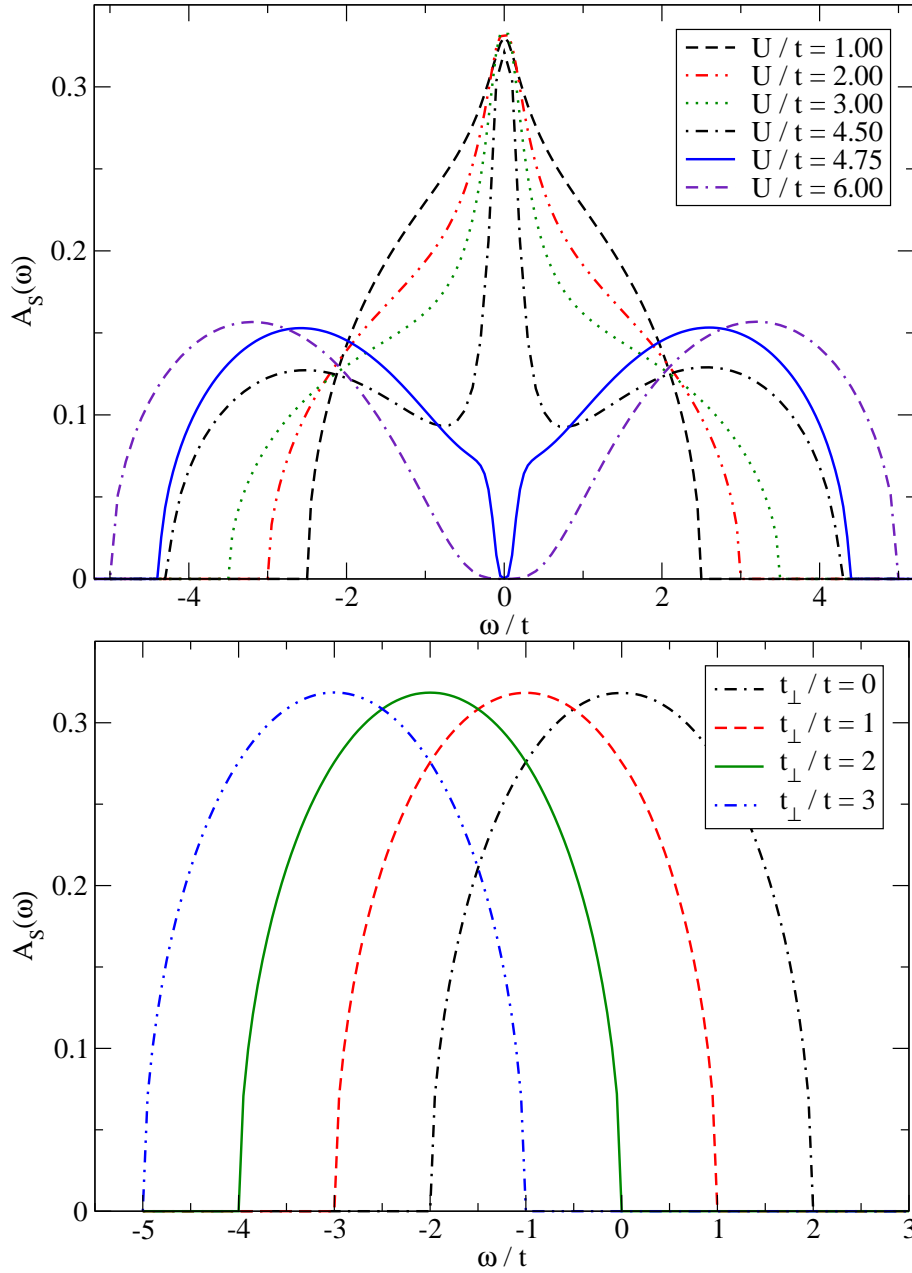[2]We used an insulating Weiss field as input guess.

Figure 2.3: Mott transition (upper panel). Spectral densities of the uncoupled ($t_\perp/t = 0$) two-plane Hubbard model. The DOSs at $U/t = 1.0$, 2.0, 3.0, and 4.5 correspond to the metallic state, the insulating state is presented by the DOSs at $U/t = 4.75$ and 6.00. The Mott transition took place slightly below $U/t = 4.75$, $T/t = 0.025$. Band transition (lower panel). Reconstructed symmetric spectral densities of the free two-plane Hubbard model ($U/t = 0$). One can see the symmetric DOSs at $t_\perp/t = 0$, 1, 2, and 3. The overlap of $A_S(\omega)$ and $A_A(\omega)$ vanishes above $t_\perp/t = 2$, which denotes the band insulating state.
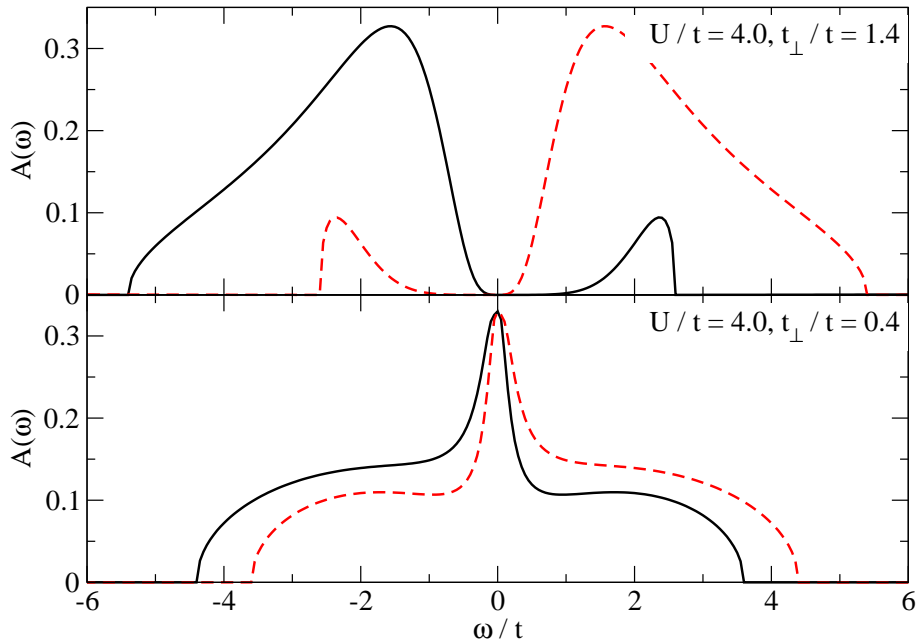
Figure 2.4: Reconstructed spectral densities of the two-plane Hubbard model in the symmetric/ antisymmetric basis at non-zero U and $t_\perp$ at half filling. Upper panel: the overlap of the symmetric (solid line) and antisymmetric (broken line) DOS at $\omega = 0$ is equal 0 – the system is an insulator. Lower panel: the system is in the metallic state.

Now we consider the optical conductivity at constant interaction. We took $U/t = 2$, because the conductivity spectrum at $U/t = 0$ has the Drude peak only, which has small demonstrative worth. The optical conductivity at different $t_\perp$, $U/t = 2$ is depicted on the lower panel of Figure 2.5, again consisting of the Drude peak and hard distinguishable covering of the mid-infrared and incoherent peaks. The growth of the inter-plane hopping amplitude causes the reduction of the spectral weight and leads to the vanishing of the Drude peak above $t_\perp/t \approx 1.8$, indicating the transition to a predominantly band insulating state. The critical value was obtained using a linear fit of the squared weight of the Drude peak (s. inset).

2.4.3 Phase Diagram

The phase diagram was performed using the weight of the Drude peak. The Drude weight as a function of U and $t_\perp$ is shown in Figure 2.6. Note, we present the Drude weight in the pure metallic region, because this result was achieved using an insulating input Weiss field. As expected the function has its maximum at the origin of the U-$t_\perp$-plane. Increasing interaction and (or) inter-plane hopping amplitude decrease(s) the direct-current conductivity until it disappears and the system becomes an insulator.

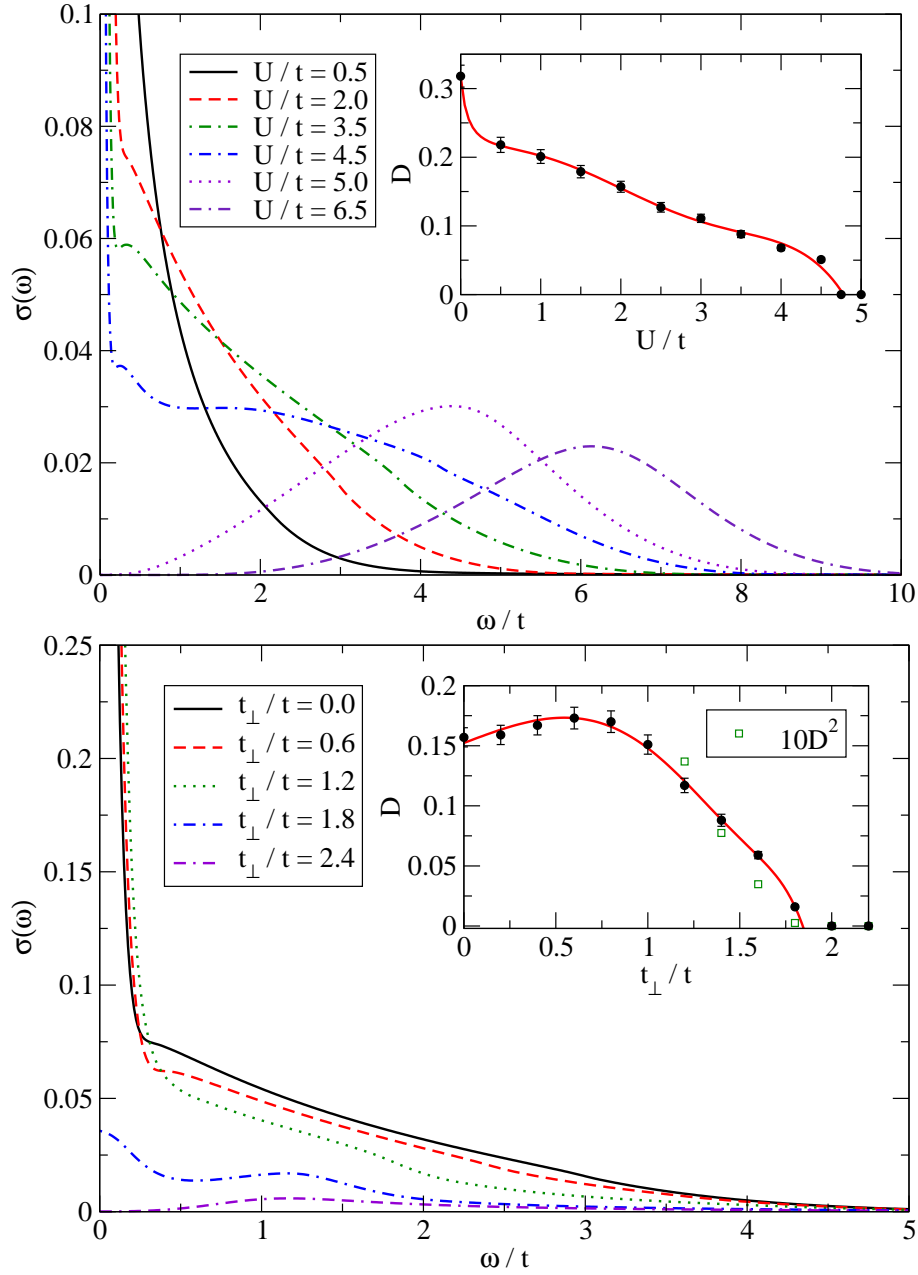In order to localize the metal-to-insulator transition we analyzed the devolution of

Figure 2.5: Evolution of the optical conductivity of the single plane (upper panel), and as a function of $t_\perp$ at $U/t = 2$ (lower panel). Upper inset: the run of the Drude weight with increasing U. As it can be seen, the Drude weight vanishes at $U/t \approx 4.7$, where the metal-to-Mott-insulator transition takes place. Lower inset: The run of the Drude weight as a function of $t_\perp$. The Drude weight vanishes at $t_\perp/t \approx 1.8$, where a metal-to-insulator transition takes place.
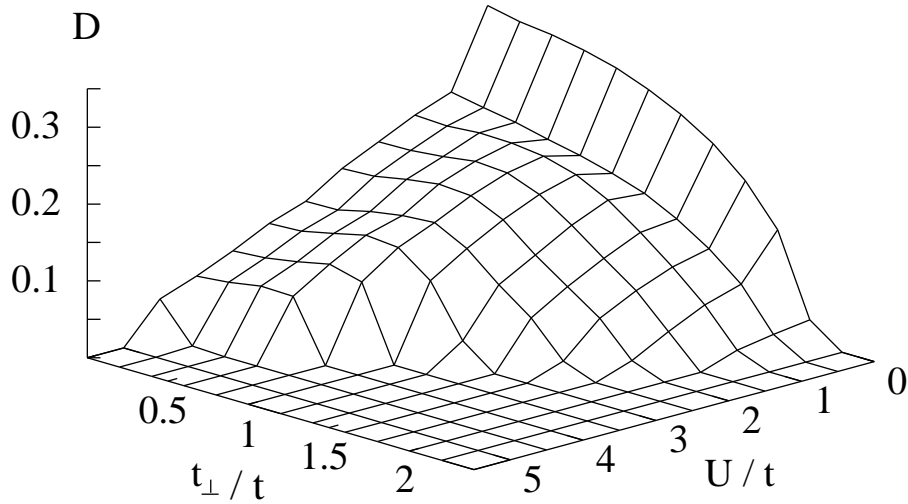
61

Figure 2.6: Drude weight D at temperature $T/t = 0.025$ in the pure metallic region,which corresponds to the low-U, low-$t_\perp$ region, see also phase diagram 2.7.

the weight of the Drude peak as a function of U ($t_\perp$). We found, that the Drude weight vanishes as $D(x) \approx \sqrt{x_C - x}$, where $x < x_C$ and $x = U$ or $x = t_\perp$, close to the U- and $t_\perp$-axis and slightly before the phase transition. Therefore in order to find the phase transition, we focused on the linear part of the squared weight of the Drude peak (compare Fig. 2.2, lower panel).

The obtained phase diagram is given in Figure 2.7 (upper panel). The metal-to-insulator transition could be clearly located. The error bars show which parameter (U or $t_\perp$) was used for the determination of the transition. We observe a second order phase transition between metallic and band-insulating regions. The Mott transition is the first order transition, so we see a coexistence region.

In order to demonstrate both metallic and insulating convergent solution we picked out the typical coexistent point $U/t = 4.6$ and $t_\perp/t = 0.5$ and presented corresponding Green functions as well as the density of states (Figure 2.8). The imaginary part of the metallic Green function has a discontinuity at $\omega = 0$, whereas the insulating solution shows a smooth transition from the negative to the positive frequency region. The similar behavior we observe by the real part of the Green function, where the insulating solution has a finite value at $\omega = 0$ and the metallic one seems to have a infinite value at the same frequency. As expected, at larger frequencies both solutions are identical. On the lower panel we note a clear quasiparticle peak on the metallic density of states, which disappear in the insulating solution.

Returning to the phase diagram 2.7 one can observe a triple point at $U/t \approx 2.5$, $t_\perp/t \approx 1.5$, which gives an approximate clue for the region where the transition between two insulating phases takes place. The absence of the appropriate quantity caused difficulties in the understanding of the transition scenario. In order to throw light on this problem we consider the evolution of the lower Hubbard band (LHB) of the symmetric spectral density
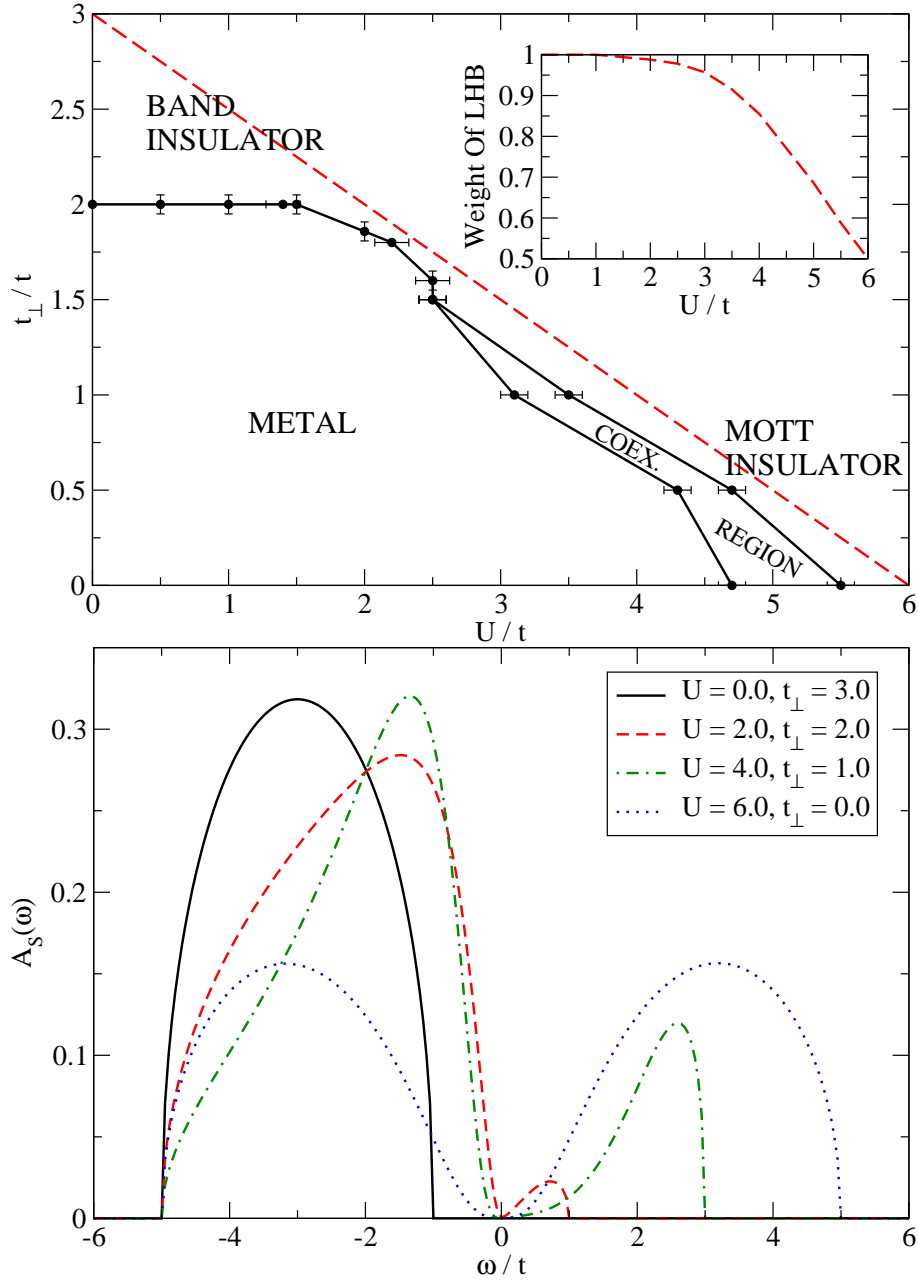
Figure 2.7: Phase diagram at $T/t = 0.025$ (upper panel). Inset: the evolution of the weight of the lower Hubbard band of the symmetric plane on the dotted line. — By comparing to Fig. 2.6, the metallic region is recognized as the region with non-vanishing Drude weight. The lower panel gives selection of the reconstructed spectral densities on the dotted line of the upper panel. — A purely Mott insulating state is characterized by the spectral density of the symmetric or antisymmetric plane, resp., divided by half into a lower and an upper Hubbard band, whereas a purely band insulating state means the symmetric band is entirely located below $\omega = 0$, and the antisymmetric band entirely above.
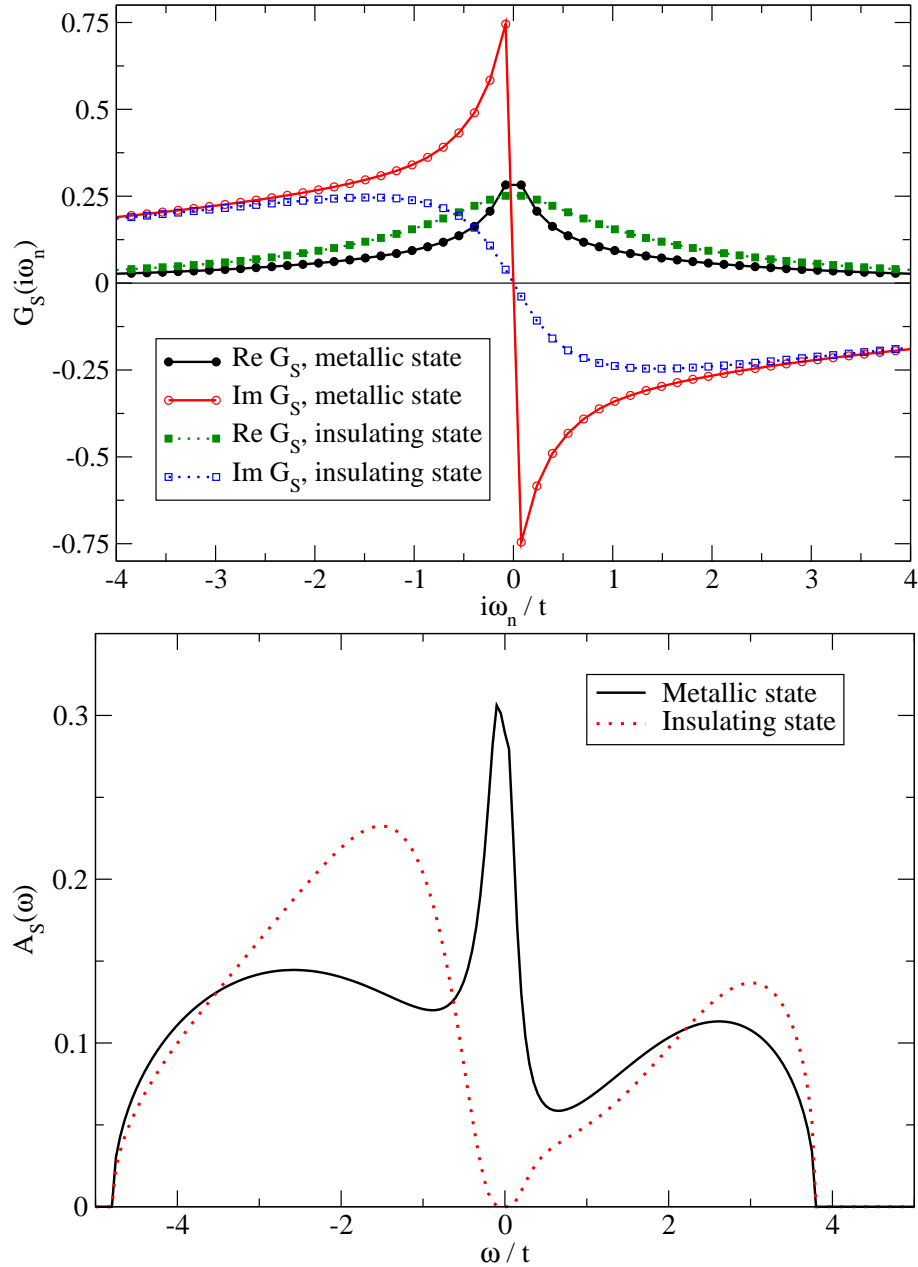
Figure 2.8: Two completely convergent solutions – metallic and insulating state at $U/t = 4.6$ and $t_\perp/t = 0.5$. The symmetric Green function as a function of Matsubara frequencies (upper panel) and the corresponding density of states (lower panel).
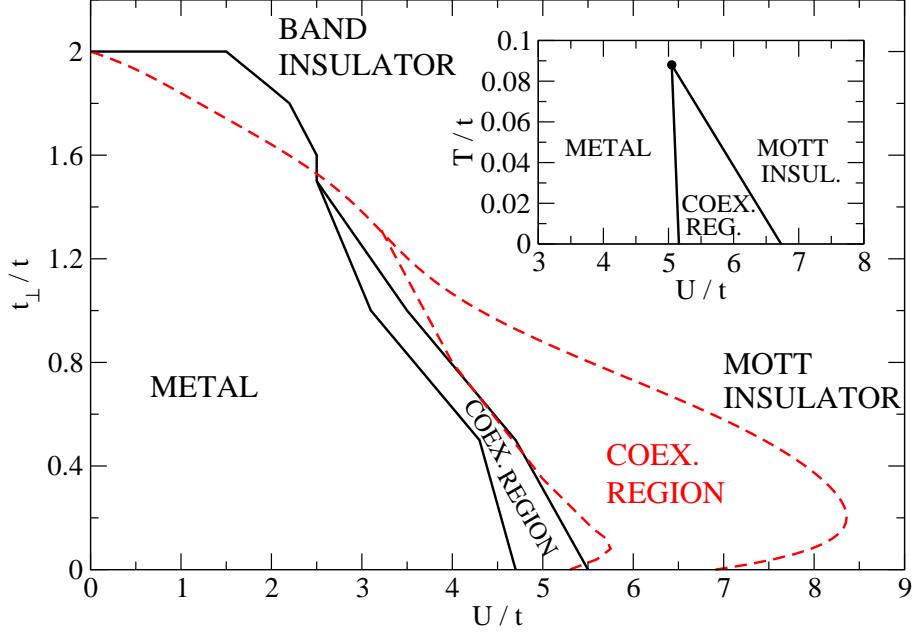
Figure 2.9: Comparison of phase diagrams. Broken line: phase diagram computed by Moeller et al. [64] using IPT at $T/t = 0$ (broken line). Solid line: phase diagram performed in current work using QMC at $T/t = 0.025$. Inset: $T - U$ phase diagram at $t_\perp = 0$ presented by Georges et al. in [4].

on the dotted line on the upper panel of Fig. 2.7. The developing of the LHB's weight, which is defined as $\int_{-\infty}^{0} d\omega\, A_S(\omega)$, can be found in the inset. The lower and the upper Hubbard band (UHB) have identical weight in the Mott phase, namely 1/2, walking along the dotted line we observe a smooth redistribution of the weight: the weight of the LHB grows at the expense of the UHB (antisymmetric DOS: the UHB grows at the expense of the LHB). The weight of the LHB achieves 1 in the band insulator predominant region. Some examples of the symmetric DOS are shown on the lower panel of Figure 2.7. As it can be seen the weight of the LHB does neither show some distinct kink nor vanish from a well-defined point. Therefore, this quantity does not yield any indication for a phase transition between the Mott and the band insulating phase.

In order to get more information about this transition we considered the vanishing exponents of the Drude weight, but it was not possible to obtain accurate results especially in the region, we were interested in.

Finally we compare our diagram with the phase diagram from the earlier work by Moeller et al. [64], which was computed using iteration perturbation theory [72, 73] at $T/t = 0$, with $2t_{ab} = t_\perp$ and $2U_{\text{Moeller}} = U$. We observe following differences (Figure 2.9): The coexistence region computed by Moeller et al. is essentially wider than our one, which can be explained with temperature distinction ($T/t = 0$ vs. $T/t = 0.025$). In fact, the increasing temperature causes shrinking of the coexistence region, which can be seen on

the inset, where the part of the T-U diagram at $t_\perp/t = 0$, presented by Georges et al. [4], is shown. An other disagreement is the devolution of the border between the metal and the band insulator. In contrast to Moeller, we got a constant critical inter-plane hopping equal to $2t$ for repulsions smaller than $1.5t$. We don't expect a crucial change of the diagram in that region with the temperature, and guess that the reason for the difference is of a technical nature, caused by the different computational methods. Further, neither Moeller et al. nor we found a clear transition from Mott to band insulator.

The present numerical results can be combined to the following picture: Even though, it seems that both metal-to-insulator transitions have different nature, we have not found any evidence for a certain transition scenario between two insulating phases. The spectral densities show a smooth transition from Mott to band insulator and the metal-to-insulator transition line is nearly smooth too, which argues for the cross-over between both phases. Moreover, the clear identification of the nature of the metal-to-insulator transition in the central region of the MIT line was impossible, which supports the cross-over assumption.

2.5 Conclusion

Finishing current chapter we resume our work:

1. In order to treat a three-dimensional system using a quadratic Hubbard plane, we consider a two-plane Hubbard model with inter-plane hopping, which corresponds to the CuO-bilayers in the high-T_C superconductors. The main technic, used in the present investigation, was an extended dynamical mean field theory. As two-impurity solver we chose a Quantum Monte-Carlo algorithm, a numerically exact method without any uncontrolled approximations. The analytical continuation was performed via maximum entropy data analysis. Also two different modifications of the algorithm for the calculation of optical conductivity were considered, whereat was found that the method given by Blümer is more appropriate for the purpose of determination of the Drude weight than our approach.

2. The spectral densities of a two-plane Hubbard model at low temperature for different values of the inter-plane coupling were calculated. Further, the optical conductivity and the corresponding Drude weight were obtained at several regions of the phase diagram. A low temperature ($T/t = 0.025$) phase diagram was presented, where the first order Mott transition as well as the second order metal-to-band insulator transitions were found. The clear transition between the Mott insulating phase and the band insulating phase was not detected. The corresponding spectral weights show a continuous behavior which is coherent with the assumption about the crossover between those two insulating phases. The phase diagram computed in the present work differs slightly from Moeller's one, because the calculations were performed at different temperatures, and two fundamentally diverse techniques were used. According to our findings and to the related works, we tend to claim, that the transition between the Mott and the band insulators is a crossover.

3. As a field of the future work, we suggest the inclusion of the inter-plane spin-spin correlations, which was not regarded in the present model, but is surely relevant for the investigation of the magnetic phase diagram of the system. Furthermore the away from half-filling consideration is a matter of particular interest, whereas the computations can be performed at significantly lower temperature using a very recently developed continuous-time QMC algorithm [74].

Appendix A

Analytical Support

A.1 Green Function

High Frequency Limit

We consider the first order high-frequency behavior of the Green functions $G_{0\sigma}(\omega_n)$ and $G_{1\sigma}(\omega_n)$.

$$
\begin{aligned}
G_{a\sigma}(\omega_n) &= \int (dp) \frac{\gamma_{\boldsymbol{p}}^a}{i\omega_n - (\varepsilon_{\boldsymbol{p}} - \mu) - \Sigma_\sigma(\boldsymbol{p}, \omega_n)} \\
&\approx \frac{1}{i\omega_n} \int (dp) \gamma_{\boldsymbol{p}}^a \sum_{j=0}^{\infty} \left(\frac{\varepsilon_{\boldsymbol{p}} - \mu + \Sigma_\sigma(\boldsymbol{p}, \omega_n)}{i\omega_n} \right)^j,
\end{aligned}
\tag{A.1}
$$

with $a = 0, 1$, $\Sigma_\sigma(\boldsymbol{p}, \omega_n) = \Sigma_{0\sigma}(\omega_n) + 2d\gamma_{\boldsymbol{p}}\Sigma_1(\omega_n)$, $\varepsilon_{\boldsymbol{p}} = -zt\gamma_{\boldsymbol{p}}$, $\gamma_{\boldsymbol{p}} = \frac{1}{2}(\cos(p_x) + \cos(p_y))$ and $\int (dp) = \frac{1}{(2\pi)^2} \int_{-\pi}^{\pi} dp_x \int_{-\pi}^{\pi} dp_y$. The high-frequency limit approximation $\Sigma_{0\sigma}(\omega_n) \approx \frac{1}{i\omega_n}$ and $\Sigma_1(\omega_n) \approx \frac{1}{(i\omega_n)^2}$ leads to

$$
\begin{aligned}
G_{0\sigma}(\omega_n) &\approx \frac{1}{i\omega_n} + \frac{\Sigma_{0\sigma}(\omega_n) - \mu}{(i\omega_n)^2} + \frac{\frac{(zt)^2}{4} + \mu^2}{(i\omega_n)^3} + \mathcal{O}(\omega_n^{-4}) \\
G_1(\omega_n) &\approx \frac{z(\Sigma_1(\omega_n) - t)}{4(i\omega_n)^2} + \frac{zt(\mu - \Sigma_{0\sigma}(\omega_n))}{2(i\omega_n)^3} - \frac{\frac{9(zt)^3}{64} + \frac{3zt\mu^2}{4} + \mu^3}{(i\omega_n)^4} + \mathcal{O}(\omega_n^{-5}),
\end{aligned}
\tag{A.2}
$$

where we used $\int (dp) \gamma_{\boldsymbol{p}}^k = 0$ if k odd[1].

Correction Of $G(\tau)$

Considering the leading term in the approximation above we correct the Fourier transformed Green function. In fact, the infinite sum over Matsubara frequencies should be

---

[1] $\int (dp) \gamma_{\boldsymbol{p}}^2 = \frac{1}{4}$; $\int (dp) \gamma_{\boldsymbol{p}}^4 = \frac{9}{64}$

computed very carefully. This requires a summation over *all* frequencies. For this reason an infinite sum should be calculated, which can be done (in G_0 case) using

$$\frac{4}{\pi} \sum_{n=0}^{\infty} \frac{\sin(2n+1)x}{2n+1} = \begin{cases} -1 & -\pi < x < 0 \\ 0 & x = -\pi, 0, \pi \\ 1 & 0 < 0 < \pi. \end{cases} \tag{A.3}$$

The infinite sum becomes

$$\frac{1}{\beta} \sum_{n=-\infty}^{\infty} e^{-i\omega_n \tau} \frac{1}{i\omega_n} = \frac{1}{\beta} \sum_{n=0}^{\infty} -2i \sin(\omega_n \tau) \frac{1}{i\omega_n} = -\frac{2}{\pi} \sum_{n=0}^{\infty} \frac{\sin(2n+1)\frac{\pi\tau}{\beta}}{2n+1} = -0.5, \tag{A.4}$$

where $\omega_n = (2n+1)\pi T$ and $0 < \tau < \beta$. The above sum is equal to 0 at $\tau = 0$, which is explainable with the discontinuity of Green function on the imaginary time axis at $\tau = k\beta$, where k is integer. In fact, the value of the Green function at $\tau = 0$ calculated by the Fourier transformation is $G_0(0^+) + G_0(0^-) = G_0(0^+) - G_0(\beta^-)$, which is equal 0 in the paramagnetic state.

The infinite sum needed for the Fourier transformation of G_1 can be performed using the equation

$$\frac{\pi}{2} - \frac{4}{\pi} \sum_{n=0}^{\infty} \frac{\cos(2n+1)x}{(2n+1)^2} = |x|, \tag{A.5}$$

which leads to

$$\frac{zt}{4\beta} \sum_{n=-\infty}^{\infty} e^{-i\omega_n \tau} \frac{1}{\omega_n^2} = \frac{zt}{4\beta} \sum_{n=0}^{\infty} 2\cos(\omega_n \tau) \frac{1}{\omega_n^2} = \frac{zt\beta}{2\pi^2} \sum_{n=0}^{\infty} \frac{\cos(2n+1)\frac{\pi\tau}{\beta}}{(2n+1)^2}$$
$$= \frac{zt\beta}{8} \left[\frac{1}{2} - \frac{\tau}{\beta} \right], \tag{A.6}$$

where z is the number of nearest neighbors and t is the hopping amplitude.

A.2 Internal Energy

Analytical Derivative

The Internal energy in the Hubbard model is defined as

$$E = \langle H \rangle = \langle T + V \rangle = -t \sum_{i,a,\sigma} \left\langle c_{i+a\sigma}^{\dagger} c_{i\sigma} \right\rangle + U \sum_{i} \langle n_{i\uparrow} n_{i\downarrow} \rangle, \tag{A.7}$$

where the operator $c_{i\sigma}^{\dagger}/c_{i\sigma}$ creates/annihilates a fermion with the spin σ on the site i. The operator $n_{i\sigma}$ gives the number of particles with the spin σ on the site i. t is the nearest neighbor hopping amplitude, U is the on-site Coulomb interaction. The nearest neighbor

to the site i is defined as $i + a$. To find the expression for the Coulomb term we consider the following equation of motion

$$\lim_{\tau \to 0} \frac{\partial G_{ii\uparrow}}{\partial \tau} = \lim_{\tau \to 0} \frac{\partial}{\partial \tau} \left\langle \mathrm{T} c_{i\uparrow}(\tau) c_{i\uparrow}^\dagger(0) \right\rangle = \lim_{\tau \to 0^+} \left\langle [H, c_{i\uparrow}(\tau)] \, c_{i\uparrow}^\dagger(0) \right\rangle. \tag{A.8}$$

Substitution of the commutator

$$\begin{aligned}
[H, c_{i\uparrow}] &= -t \sum_{l,a,\sigma} \left[c_{l+a\sigma}^\dagger c_{l\sigma}, c_{i\uparrow} \right] + U \sum_l [n_{l\uparrow} n_{l\downarrow}, c_{i\uparrow}] \\
&= t \sum_{l,a,\sigma} c_{l\sigma} \delta_{il+a} \delta_{\uparrow\sigma} - U \sum_l n_{l\downarrow} c_{l\uparrow} \delta_{il} = t \sum_a c_{i+a\uparrow} - U n_{i\downarrow} c_{i\uparrow}
\end{aligned} \tag{A.9}$$

in the equation (A.8) yields

$$\begin{aligned}
\lim_{\tau \to 0} \frac{\partial G_{ii\uparrow}}{\partial \tau} &= \lim_{\tau \to 0} \left(t \sum_a \left\langle c_{i+a\uparrow} c_{i\uparrow}^\dagger \right\rangle - U \left\langle n_{i\downarrow} c_{i\uparrow} c_{i\uparrow}^\dagger \right\rangle \right) \\
&= \lim_{\tau \to 0} \left(t \sum_a G_{i+ai\uparrow} - U \left\langle n_{i\downarrow} \right\rangle + U \left\langle n_{i\downarrow} n_{i\uparrow} \right\rangle \right).
\end{aligned} \tag{A.10}$$

Now we have a similar expression for the most problematic part of the internal energy:

$$\lim_{\tau \to 0} U \left\langle n_{i\downarrow} n_{i\uparrow} \right\rangle = \lim_{\tau \to 0} \frac{1}{2} \sum_\sigma \left(\frac{\partial G_{ii\sigma}}{\partial \tau} - t \sum_a G_{i+ai\sigma} + U \left\langle n_{i\sigma} \right\rangle \right). \tag{A.11}$$

Using equation (A.7) the internal energy becomes

$$E = \lim_{\tau \to 0} \frac{1}{2} \sum_{i,\sigma} \left(\frac{\partial G_{ii\sigma}}{\partial \tau} + t \sum_a G_{i+ai\sigma} + U \left\langle n_{i\sigma} \right\rangle \right). \tag{A.12}$$

In the following we calculate each part of the energy individually:

$$\begin{aligned}
\lim_{\tau \to 0} \sum_i \frac{\partial G_{ii\sigma}}{\partial \tau} &= \lim_{\tau \to 0^+} \sum_i \frac{\partial}{\partial \tau} \left\langle c_{i\sigma}(\tau) c_{i\sigma}^\dagger(0) \right\rangle \\
&= \lim_{\tau \to 0^+} \frac{\partial}{\partial \tau} T \sum_n \sum_{\boldsymbol{p},\boldsymbol{q}} \sum_i \frac{\mathrm{e}^{-i(\boldsymbol{p}-\boldsymbol{q})\boldsymbol{r}_i}}{V^2} \mathrm{e}^{-i\omega_n \tau} \left\langle c_{\boldsymbol{p}\sigma} c_{\boldsymbol{q}\sigma}^\dagger \right\rangle,
\end{aligned} \tag{A.13}$$

where in limit of $V \to \infty$, the sum over wave vectors reduces to an integral

$$\begin{aligned}
\sum_{\boldsymbol{p},\lambda} f_\lambda(\boldsymbol{p}) &= \sum_{n_x,n_y,n_z} \sum_\lambda f_\lambda\left(\frac{2\pi \boldsymbol{n}}{L} \right) \xrightarrow[L \to \infty]{} \int dn_x \int dn_y \int dn_z \sum_\lambda f_\lambda\left(\frac{2\pi \boldsymbol{n}}{L} \right) \\
&= \frac{V}{(2\pi)^3} \sum_\lambda \int d^3 p \, f_\lambda(\boldsymbol{p}).
\end{aligned} \tag{A.14}$$

71

In fact, for large L, where L is the length of the considered box, the function $f_\lambda\left(\frac{2\pi\boldsymbol{n}}{L}\right)$ varies very slowly when the integers change by unity so that n_x, n_y, n_z, may be considered as continuous variables [17]. Therefore we follow with

$$
\begin{aligned}
\lim_{\tau\to 0}\sum_i \frac{\partial G_{ii\sigma}}{\partial\tau} &= \lim_{\tau\to 0^+}\frac{\partial}{\partial\tau}T\sum_n\int(dp)\int(dq)\sum_i \mathrm{e}^{-i(\boldsymbol{p}-\boldsymbol{q})\boldsymbol{r}_i}\mathrm{e}^{-i\omega_n\tau}\left\langle c_{\boldsymbol{p}\sigma}c^\dagger_{\boldsymbol{q}\sigma}\right\rangle \\
&= \lim_{\tau\to 0^+}\frac{\partial}{\partial\tau}T\sum_n\int(dp)\int(dq)\delta(\boldsymbol{p}-\boldsymbol{q})\mathrm{e}^{-i\omega_n\tau}\left\langle c_{\boldsymbol{p}\sigma}c^\dagger_{\boldsymbol{q}\sigma}\right\rangle \\
&= \lim_{\tau\to 0^+}T\sum_n\int(dp)(-i\omega_n)\mathrm{e}^{-i\omega_n\tau}\left\langle c_{\boldsymbol{p}\sigma}c^\dagger_{\boldsymbol{p}\sigma}\right\rangle \\
&= T\sum_n\int(dp)(-i\omega_n)\left\langle c_{\boldsymbol{p}\sigma}c^\dagger_{\boldsymbol{p}\sigma}\right\rangle = T\sum_n\int(dp)\frac{-i\omega_n}{i\omega_n-\varepsilon_{\boldsymbol{p}}+\mu-\Sigma(\boldsymbol{p},\omega_n)},
\end{aligned}
\tag{A.15}
$$

where $\int(dp)=\frac{1}{(2\pi)^d}\int d^dp$ and d is dimension of the box. The remaining parts of equation (A.12) are calculated as follows

$$
\begin{aligned}
\lim_{\tau\to 0}t\sum_{i,a}\left\langle c_{i+a\sigma}(\tau)c^\dagger_{i\sigma}(0)\right\rangle &= \lim_{\tau\to 0}Tt\sum_{i,a,n}\sum_{\boldsymbol{p},\boldsymbol{q}}\frac{\mathrm{e}^{-i\boldsymbol{p}\boldsymbol{r}_{i+a}}}{V}\frac{\mathrm{e}^{i\boldsymbol{q}\boldsymbol{r}_i}}{V}\mathrm{e}^{-i\omega_n\tau}\left\langle c_{\boldsymbol{p}\sigma}c^\dagger_{\boldsymbol{q}\sigma}\right\rangle \\
&= \lim_{\tau\to 0}Tt\sum_{i,a,n}\sum_{\boldsymbol{p},\boldsymbol{q}}\frac{\mathrm{e}^{-i(\boldsymbol{p}-\boldsymbol{q})\boldsymbol{r}_i}}{V^2}\mathrm{e}^{-i\boldsymbol{p}\boldsymbol{r}_a}\mathrm{e}^{-i\omega_n\tau}\left\langle c_{\boldsymbol{p}\sigma}c^\dagger_{\boldsymbol{q}\sigma}\right\rangle \\
&= \lim_{\tau\to 0}Tt\sum_{a,n}\int(dp)\int(dq)\delta(\boldsymbol{p}-\boldsymbol{q})\mathrm{e}^{-i\boldsymbol{p}\boldsymbol{r}_a}\mathrm{e}^{-i\omega_n\tau}\left\langle c_{\boldsymbol{p}\sigma}c^\dagger_{\boldsymbol{q}\sigma}\right\rangle \\
&= T\sum_n\int(dp)t\sum_a\mathrm{e}^{-i\boldsymbol{p}\boldsymbol{r}_a}\left\langle c_{\boldsymbol{p}\sigma}c^\dagger_{\boldsymbol{p}\sigma}\right\rangle = T\sum_n\int(dp)(-\varepsilon_{\boldsymbol{p}})\left\langle c_{\boldsymbol{p}\sigma}c^\dagger_{\boldsymbol{p}\sigma}\right\rangle \\
&= T\sum_n\int(dp)\frac{-\varepsilon_{\boldsymbol{p}}}{i\omega_n-\varepsilon_{\boldsymbol{p}}+\mu-\Sigma(\boldsymbol{p},\omega_n)},
\end{aligned}
\tag{A.16}
$$

and

$$
\begin{aligned}
\lim_{\tau\to 0}U\sum_i\langle n_{i\sigma}\rangle &= \lim_{\tau\to 0}U\sum_i\left\langle c^\dagger_{i\sigma}(\tau)c_{i\sigma}(0)\right\rangle \\
&= \lim_{\tau\to 0}UT\sum_{i,n}\sum_{\boldsymbol{p},\boldsymbol{q}}\frac{\mathrm{e}^{-i\boldsymbol{p}\boldsymbol{r}_i}}{V}\frac{\mathrm{e}^{i\boldsymbol{q}\boldsymbol{r}_i}}{V}\mathrm{e}^{i\omega_n\tau}\left\langle c^\dagger_{\boldsymbol{p}\sigma}c_{\boldsymbol{q}\sigma}\right\rangle \\
&= \lim_{\tau\to 0}UT\sum_n\int(dp)\mathrm{e}^{i\omega_n\tau}\left\langle c^\dagger_{\boldsymbol{p}\sigma}c_{\boldsymbol{p}\sigma}\right\rangle = T\sum_n\int(dp)(-U)\left\langle c_{\boldsymbol{p}\sigma}c^\dagger_{\boldsymbol{p}\sigma}\right\rangle \\
&= T\sum_n\int(dp)\frac{-\mu}{i\omega_n-\varepsilon_{\boldsymbol{p}}+\mu-\Sigma(\boldsymbol{p},\omega_n)}.
\end{aligned}
\tag{A.17}
$$

Now we put (A.15) - (A.17) in equation (A.12) and get the new internal energy

$$
\begin{aligned}
E &= -\frac{1}{2}T\sum_{n,\sigma}\int (dp)\frac{i\omega_n + \varepsilon_{\boldsymbol{p}} + \mu}{i\omega_n - \varepsilon_{\boldsymbol{p}} + \mu - \Sigma_\sigma(\boldsymbol{p},\omega_n)} \\
&= T\sum_{n,\sigma}\int (dp)\left(-\frac{1}{2} - \frac{\varepsilon_{\boldsymbol{p}} + \frac{1}{2}\Sigma_\sigma(\boldsymbol{p},\omega_n)}{i\omega_n - \varepsilon_{\boldsymbol{p}} + \mu - \Sigma_\sigma(\boldsymbol{p},\omega_n)}\right) \\
&= T\sum_{n,\sigma}\int (dp)\left[-\frac{1}{2} - \left(\varepsilon_{\boldsymbol{p}} + \frac{1}{2}\Sigma_\sigma(\boldsymbol{p},\omega_n)\right)G_\sigma(\boldsymbol{p},\omega_n)\right]
\end{aligned}
\tag{A.18}
$$

In the following we consider the energy without the constant term $-\frac{1}{2}$ and obtain

$$
E = -T\sum_{n,\sigma}\int (dp)\left(\varepsilon_{\boldsymbol{p}} + \frac{1}{2}\Sigma_\sigma(\boldsymbol{p},\omega_n)\right)G_\sigma(\boldsymbol{p},\omega_n)
\tag{A.19}
$$

and

$$
K = -T\sum_{n,\sigma}\int (dp)\varepsilon_{\boldsymbol{p}}G_\sigma(\boldsymbol{p},\omega_n).
\tag{A.20}
$$

Energy Correction

The energy equation (A.19) contains an infinite sum over fermionic Matsubara frequencies ω_n. The numerical evaluation of such sums will be possible when we combine the computed data (from $n_{\min}$ to $n_{\max}$) with a high frequency correction. For this purpose we calculate the energy E' with self-energy $\Sigma_\sigma(i\omega_n) = \frac{U^2}{4i\omega_n}$ analytically:

$$
\begin{aligned}
E' &= T\sum_{\sigma,n}\int (dp)\frac{\varepsilon_{\boldsymbol{p}} + \frac{U^2}{8i\omega_n}}{i\omega_n - \varepsilon_{\boldsymbol{p}} - \frac{U^2}{4i\omega_n}} = 2T\sum_n\int (dp)\frac{\varepsilon_{\boldsymbol{p}} + \frac{U^2}{8i\omega_n}}{i\omega_n\left(1 - \frac{\varepsilon_{\boldsymbol{p}}}{i\omega_n} - \frac{U^2}{4(i\omega_n)^2}\right)} \\
&\approx 2T\sum_n\frac{1}{i\omega_n}\int (dp)\left(\varepsilon_{\boldsymbol{p}} + \frac{U^2}{8i\omega_n}\right)\left(1 + \frac{\varepsilon_{\boldsymbol{p}}}{i\omega_n} + \frac{U^2 + 4\varepsilon_{\boldsymbol{p}}^2}{4(i\omega_n)^2} + \mathcal{O}\left(\omega_n^{-3}\right)\right)
\end{aligned}
\tag{A.21}
$$

Using $\int (dp)\varepsilon_{\boldsymbol{p}}^k = 0$ if k an odd number, and $\int (dp)\varepsilon_{\boldsymbol{p}}^2 = \frac{(zt)^2}{4}$ we obtain the energy

$$
E' \approx -\frac{1}{4}T\left(2(zt)^2 + U^2\right)\frac{1}{(\pi T)^2}\sum_n\frac{1}{(2n+1)^2} = -\frac{2(zt)^2 + U^2}{4\pi^2 T}\frac{\pi^2}{4},
\tag{A.22}
$$

where we used $\sum_{n=-\infty}^{\infty}\frac{1}{(2n+1)^2} = \frac{\pi^2}{4}$. The energy correction is equal to the difference between $E'(\omega_n = -\infty\ldots\infty)$ and $E'(\omega_n = n_{\min}\ldots n_{\max})$

$$
\Delta E = -\frac{2(zt)^2 + U^2}{4\pi^2 T}\left(\frac{\pi^2}{4} - \sum_{n=n_{\min}}^{n_{\max}}\frac{1}{(2n+1)^2}\right),
\tag{A.23}
$$

where the sum can be performed numerically.

Large-U Expansion

An expansion of the grand canonical potential of the square lattice Hubbard model up to order t^4 was performed by K. Kubo in 1980 [18]. The diagrams contributing to the perturbational series of the thermodynamic potential yield an approximated grand canonical potential per lattice site

$$\Omega \approx \Omega_0 + \Omega_2 + \Omega_{4a+b} + \Omega_{4c+d} + \Omega_{4e} + \Omega_{4f}, \tag{A.24}$$

where the individual terms can be expressed as follows

$$\Omega_0 = -kT \ln Z$$

$$\Omega_2 = -zt^2 \left[\beta \left(\gamma - 2\gamma^2 \right) + \frac{2}{U} \left(1 - e^{-\beta U} \right) \gamma^2 \right]$$

$$\Omega_{4a+b} = -zt^4 \left[\frac{1}{12} \beta^3 \left(\gamma - 2\gamma^2 \right) + 4\frac{\beta}{U^2} \left(1 + e^{-\beta U} \right) \gamma^2 - \frac{8}{U^3} \left(1 - e^{-\beta U} \right) \gamma^2 \right]$$

$$\Omega_{4c+d} = -z \left(z - 1 \right) t^4 \left[\frac{1}{6} \beta^3 \left(\gamma - 2\gamma^2 \right) + \frac{\beta^2}{U} \left(\gamma^2 - 2 \left(1 + e^{-\beta U} \right) \gamma^3 \right) \right.$$

$$\left. + 2\frac{\beta}{U^2} \left(e^{-\beta U} \gamma^2 + 2 \left(1 - e^{-\beta U} \right) \gamma^3 \right) - \frac{2}{U^3} \left(1 - e^{-\beta U} \right) \gamma^2 \right]$$

$$\Omega_{4e} = -pt^4 \left[\frac{2}{3} \beta^3 \left(\gamma - 10\gamma^2 + \left(29 - 3e^{-\beta U} \right) \gamma^3 - \left(26 - 14e^{-\beta U} \right) \gamma^4 \right) \right. \tag{A.25}$$

$$+ 8\frac{\beta^2}{U} \left(\gamma^2 - \left(5 - e^{-\beta U} \right) \gamma^3 + 6 \left(1 - e^{-\beta U} \right) \gamma^4 \right)$$

$$+ 8\frac{\beta}{U^2} \left(-2\gamma^2 + \left(9 + e^{-\beta U} \right) \gamma^3 - 10 \left(1 - e^{-\beta U} \right) \gamma^4 \right)$$

$$\left. + \frac{16}{U^3} \left(1 - e^{-\beta U} \right) \left(\gamma^2 - 5\gamma^3 + 5 \left(1 - e^{-\beta U} \right) \gamma^4 \right) \right]$$

$$\Omega_{4f} = z \left(2z - 1 \right) t^4 \left[\beta^3 \left(\gamma - 2\gamma^2 \right)^2 + 4\frac{\beta^2}{U} \left(1 - e^{-\beta U} \right) \left(\gamma^3 - 2\gamma^4 \right) \right.$$

$$\left. + 4\frac{\beta}{U^2} \left(1 - e^{-\beta U} \right)^2 \gamma^4 \right],$$

where k is a Boltzmann constant (equal 1 in our case), $z = 4$ is the number of nearest neighbors, $\gamma = e^{\beta \mu}/Z$ and p is a constant, which was set equal 1. The partition function Z in the atomic limit is defined as

$$Z = 1 + 2e^{\beta \mu} + e^{-\beta(U - 2\mu)}, \tag{A.26}$$

where $\beta = 1/T$. The chemical potential μ is equal to $U/2$ in the half-filled model. A transformation of the thermodynamical potential[2] leads to

$$E = \Omega - T\frac{\partial \Omega}{\partial T}. \tag{A.27}$$

---

[2] $\Omega = E - TS - \mu N$

The first two orders of the energy can be easily obtained analytically

$$
\begin{aligned}
E_0 &= \frac{U}{2 + 2e^{\frac{U}{2T}}}, \\
E_2 &= -\frac{2t^2}{U}\tanh\left(\frac{U}{4T}\right) + \frac{t^2\left(\frac{U}{2T}\tanh\left(\frac{U}{4T}\right) - 3\right)}{2T\cosh^2\left(\frac{U}{4T}\right)},
\end{aligned}
\tag{A.28}
$$

but the rest was computed with support of the `Maple` software.

A.3   Spin-Spin Correlator

In this section we calculate an approximate value of the $\langle \boldsymbol{S}_1 \cdot \boldsymbol{S}_2 \rangle$-correlator at high T for the 2-site Heisenberg model. The Hamiltonian is defined as

$$
H = J\boldsymbol{S}_1 \cdot \boldsymbol{S}_2,
\tag{A.29}
$$

with $J = \frac{4t^2}{U}$. The correlator at high temperature can be obtained by

$$
\langle \boldsymbol{S}_1 \cdot \boldsymbol{S}_2 \rangle = \frac{\mathrm{Tr}\left[\boldsymbol{S}_1 \cdot \boldsymbol{S}_2 e^{-\beta H}\right]}{\mathrm{Tr}\left[e^{-\beta H}\right]} \approx \frac{\mathrm{Tr}\left[\boldsymbol{S}_1 \cdot \boldsymbol{S}_2(1 - \beta H)\right]}{\mathrm{Tr}\left[1 - \beta H\right]}
\tag{A.30}
$$

There are 4 states $\left(|\uparrow\uparrow\rangle, |\downarrow\downarrow\rangle, \frac{1}{\sqrt{2}}(|\uparrow\downarrow\rangle + |\downarrow\uparrow\rangle), \frac{1}{\sqrt{2}}(|\uparrow\downarrow\rangle - |\downarrow\uparrow\rangle)\right)$, which we should take into account in the equation (A.30). Using $\boldsymbol{S}_i \cdot \boldsymbol{S}_j = S_{iz}S_{jz} + \frac{1}{2}\left(S_i^+ S_j^- + S_i^- S_j^+\right)$, where the eigenvalues of S_{iz} are $\pm\frac{1}{2}$, we get

$$
\begin{aligned}
\mathrm{Tr}\left[1 - \beta H\right] &= 4 - \beta J\left(\frac{1}{4} + \frac{1}{4} + \frac{1}{4} - \frac{3}{4}\right) = 4 \\
\mathrm{Tr}\left[\boldsymbol{S}_1 \cdot \boldsymbol{S}_2(1 - \beta H)\right] &= \left(\frac{1}{4} + \frac{1}{4} + \frac{1}{4} - \frac{3}{4}\right) - \beta J\left(\frac{1}{16} + \frac{1}{16} + \frac{1}{16} + \frac{9}{16}\right) = -\frac{3J}{4T},
\end{aligned}
\tag{A.31}
$$

which leads to

$$
\langle \boldsymbol{S}_1 \cdot \boldsymbol{S}_2 \rangle = -\frac{3t^2}{4UT}.
\tag{A.32}
$$

The correlator $\langle S_{1z}S_{2z}\rangle$ can be obtained analogously

$$
\langle S_{1z}S_{2z}\rangle = \frac{\left(\frac{1}{4} + \frac{1}{4} + \frac{1}{4} - \frac{3}{4}\right) - \beta J\left(\frac{1}{16} + \frac{1}{16} - \frac{1}{16} + \frac{3}{16}\right)}{4} = -\frac{t^2}{4TU},
\tag{A.33}
$$

leading to

$$
\langle \sigma_{1z}\sigma_{2z}\rangle = -\frac{t^2}{TU}.
\tag{A.34}
$$

A.4 SCA-Potential

In order to achieve high quality results in the SCA we should calculate the potential $V(\boldsymbol{\varphi})$ very accurately. In particular, the sum over Matsubara frequencies leads to a deviation from the analytical internal energy result, if the high frequencies are not included. Due to this reason we calculate the high frequency contribution to the sum (1.71)

$$
\begin{aligned}
\Delta &= \sum_{\omega_n,\sigma} \ln \det \left[\begin{pmatrix} 1 & 0 \\ 0 & 1 \end{pmatrix} + \frac{1}{2} \begin{pmatrix} a_{0\sigma} & a_{1\sigma} \\ a_{1\sigma} & a_{0\bar{\sigma}} \end{pmatrix}^{-1} \begin{pmatrix} \varphi_1 & 0 \\ 0 & \varphi_2 \end{pmatrix} \sigma_z \right] \\
&\approx \sum_{\omega_n,\sigma} \ln \det \begin{pmatrix} 1 + \frac{\varphi_1 \sigma_z}{2i\omega_n} & 0 \\ 0 & 1 + \frac{\varphi_2 \sigma_z}{2i\omega_n} \end{pmatrix} = \sum_{\omega_n} \ln \left[\left(1 + \frac{\varphi_1^2}{4\omega_n^2}\right)\left(1 + \frac{\varphi_2^2}{4\omega_n^2}\right) \right],
\end{aligned}
\tag{A.35}
$$

where $\sum_{\omega_n}$ runs over all frequencies $|\omega_n| > \omega_n^{\max}$ and $\omega_n^{\max}$ is the largest Matsubara frequency in the program; also we used high frequency approximation: $a_0 \approx \omega_n$ and $|a_0| \gg |a_1|$. The symmetry of the Δ leads to final result

$$
\Delta \approx 2 \sum_{\omega_n^{\max}}^{\infty} \ln \left[\prod_{i=1}^{2} \left(1 + \frac{\varphi_i^2}{4\omega_n^2}\right) \right] = \ln \left[\prod_{\omega_n^{\max}}^{\infty} \prod_{i=1}^{2} \left(1 + \frac{\varphi_i^2}{4\omega_n^2}\right)^2 \right].
\tag{A.36}
$$

The upper border of the frequency sum should be chosen so that the computations take reasonable amount of time and yield accurate results. Therefore, we chose $\infty \approx 1e5$, which yields a good agreement with the analytical result and does not significantly slow down the calculation. The same correction can be used in the 4-site SCA but the product $\prod_{i=1}^{2}$ should be substituted by $\prod_{i=1}^{4}$.

A.5 Approximate Treatment Of 2-Site Models

In present section we give approximate analytical results for two-site fictive impurity model and two-site DCA solved using semiclassical approximation. At the begin we will derive the Green function and the Weiss field, then we will find the expression for the internal energy.

Fictive Impurity Method

The self-energy in the real space model is defined as

$$
\Sigma(\boldsymbol{p}, \omega_n) = \Sigma_0 - \varepsilon_{\boldsymbol{p}} \frac{\Sigma_1}{t},
\tag{A.37}
$$

therefore the approximated Green functions become

$$
\begin{aligned}
G_0 &= \int (dp) \frac{1}{i\omega_n - \Sigma_0 - \varepsilon_{\boldsymbol{p}}\left(1 - \frac{\Sigma_1}{t}\right)} \approx \frac{1}{i\omega_n - \Sigma_0} \left(1 + \frac{K_d \left(1 - \frac{\Sigma_1}{t}\right)^2}{(i\omega_n - \Sigma_0)^2} \right) \\
G_1 &= \int (dp) \frac{-\frac{\varepsilon_{\boldsymbol{p}}}{2dt}}{i\omega_n - \Sigma_0 - \varepsilon_{\boldsymbol{p}}\left(1 - \frac{\Sigma_1}{t}\right)} \approx -\frac{K_d \left(1 - \frac{\Sigma_1}{t}\right)}{2dt(i\omega_n - \Sigma_0)^2},
\end{aligned}
\tag{A.38}
$$

where $K_d = 2dt^2$; we also assumed, that $i\omega_n - \Sigma_0$ is the dominant term. The Dyson equation $\hat{a} = \hat{\Sigma} + \hat{G}^{-1}$ yields the Weiss field

$$
\begin{aligned}
a_0 &= \Sigma_0 + \frac{G_0}{G_0^2 - G_1^2} \approx \Sigma_0 + \frac{1}{G_0} + \frac{G_1^2}{G_0^3} \\
&\approx \Sigma_0 + (i\omega_n - \Sigma_0)\left(1 - \frac{K_d\left(1 - \frac{\Sigma_1}{t}\right)^2}{(i\omega_n - \Sigma_0)^2}\right) + (i\omega_n - \Sigma_0)^3 \frac{K_d^2\left(1 - \frac{\Sigma_1}{t}\right)^2}{(2dt)^2(i\omega_n - \Sigma_0)^4} \\
&\approx i\omega_n - \frac{K_d\left(1 - \frac{\Sigma_1}{t}\right)^2}{i\omega_n - \Sigma_0}\left(1 - \frac{1}{2d}\right) \approx i\omega_n\left(1 + \frac{K_d\left(1 - \frac{\phi^2 S}{\omega_n^2}\right)^2}{\omega_n^2 + \phi^2}\left(1 - \frac{1}{2d}\right)\right) \\
a_1 &= \Sigma_1 - \frac{G_1}{G_0^2 - G_1^2} \approx \Sigma_1 - \frac{G_1}{G_0^2} \approx \Sigma_1 - (i\omega_n - \Sigma_0)^2 \frac{-K_d\left(1 - \frac{\Sigma_1}{t}\right)}{2dt(i\omega_n - \Sigma_0)^2} = t,
\end{aligned}
\tag{A.39}
$$

whereas we used $|G_0| \gg |G_1|$ at large U. According to equation (1.104) we calculate an approximated equation for the self-energy

$$
\begin{aligned}
\Sigma_0 &= \frac{\phi^2}{a_0}\left[1 + \frac{a_1^2}{a_0^2 - \phi^2}\left(1 - \frac{\phi^2 S^2}{a_0^2}\right)\right] = \frac{\phi^2\left(1 - \frac{t^2}{\omega_n^2 + \phi^2}\left(1 + \frac{\phi^2 S}{\omega_n^2}\right)\right)}{i\omega_n\left(1 + \frac{K_d\left(1 - \frac{\phi^2 S}{\omega_n^2}\right)^2\left(1 - \frac{1}{2d}\right)}{\omega_n^2 + \phi^2}\right)} \\
&\approx \frac{\phi^2}{i\omega_n}\left(1 - \frac{K_d\left(1 - \frac{\phi^2 S}{\omega_n^2}\right)^2\left(1 - \frac{1}{2d}\right)}{\omega_n^2 + \phi^2}\right)\left(1 - \frac{t^2}{\omega_n^2 + \phi^2}\left(1 + \frac{\phi^2 S}{\omega_n^2}\right)\right) \\
&\approx \frac{\phi^2}{i\omega_n}\left(1 - \frac{K_d\left(1 - \frac{\phi^2 S}{\omega_n^2}\right)^2\left(1 - \frac{1}{2d}\right) + t^2\left(1 + \frac{\phi^2 S}{\omega_n^2}\right)}{\omega_n^2 + \phi^2}\right) \\
\Sigma_1 &= -\frac{a_1\phi^2 S}{a_0^2} \approx \frac{t\phi^2 S}{\omega_n^2}.
\end{aligned}
\tag{A.40}
$$

In order to obtain the quantity ϕ, we use the equation (1.102) and the Weiss field and the self-energy calculated above and get

$$
\begin{aligned}
\frac{1}{U} &= -T\sum_n\left(\frac{1}{a_0^2 - \phi^2} + \frac{a_1^2\left(2a_0^2 + S\left(a_0^2 + \phi^2\right)\right)}{(a_0^2 - \phi^2)^3}\right) \\
&\approx T\sum_n\left(\frac{1}{\omega_n^2\left(1 + \frac{K_d\left(1 - \frac{\phi^2 S}{\omega_n^2}\right)^2\left(1 - \frac{1}{2d}\right)}{\omega_n^2 + \phi^2}\right)^2 + \phi^2} + \frac{t^2\left(-2\omega_n^2 + S\left(\phi^2 - \omega_n^2\right)\right)}{(\omega_n^2 + \phi^2)^3}\right),
\end{aligned}
\tag{A.41}
$$

expansion and substitution of the Matsubara sum by the frequency integration $T\sum_n \to \int d\omega/(2\pi)$, which is legitimate due to the low temperatures, leads to

$$
\begin{aligned}
\frac{1}{U} &\approx T\sum_n \left(\frac{1}{\omega_n^2 + \phi^2} - \frac{2K_d\omega_n^2 \left(1 - \frac{\phi^2 S}{\omega_n^2}\right)^2 \left(1 - \frac{1}{2d}\right)}{(\omega_n^2 + \phi^2)^3} + \frac{t^2 \left(S\phi^2 - \omega_n^2(2 + S)\right)}{(\omega_n^2 + \phi^2)^3} \right) \\
&\approx \frac{1}{2}\left[\frac{1}{\phi} - 2K_d\left(1 - \frac{1}{2d}\right)\left(\frac{1}{8\phi^3} - \frac{6S}{8\phi^3} + \frac{S^2}{2\phi^2 T}\right) + \frac{3t^2 S}{8\phi^3} - \frac{t^2(2 + S)}{8\phi^3} \right] \\
&= \frac{1}{2\phi} - \frac{K_d\left(1 - S - 5S\left(1 - \frac{1}{2d}\right) + \frac{4\phi S^2}{T}\left(1 - \frac{1}{2d}\right)\right)}{8\phi^3},
\end{aligned}
\tag{A.42}
$$

where the integration was approximately evaluated[3]. Note, that the sum contains a divergent T-term, so we should treat it separately. The contribution of this term is significant at low frequencies, therefore we should calculate this term more carefully. Using following approximation

$$
T\sum_n \frac{\phi^4 S^2}{\omega_n^2 (\omega_n^2 + \phi^2)^3} \approx \frac{T\phi^4 S^2}{\phi^6 T^2 \pi^2}\sum_n \frac{1}{(2n + 1)^2} = \frac{S^2}{4\phi^2 T},
\tag{A.43}
$$

which is suitable in the low frequency limit, we solve the equation (A.42) (see also subsection 1.4.2) and get

$$
\phi = \frac{U}{2} - \frac{K_d}{2U} + \frac{K_d}{2U}\left(6 - \frac{5}{2d}\right)S - \frac{K_d}{T}\left(1 - \frac{1}{2d}\right)S^2.
\tag{A.44}
$$

Finally, the quantities obtained above, can be substituted into the energy equation (1.34):

$$
\begin{aligned}
E &= T\sum_n \int (dp)\mathrm{Tr}\left[\left(\hat{\varepsilon}_{\boldsymbol{p}} + \frac{1}{2}\hat{\Sigma}\right)\hat{G}^{-1}\right] \\
&= 2T\sum_n \int (dp)\frac{\frac{1}{2}\Sigma_0(i\omega_n - \Sigma_0) + \varepsilon_{\boldsymbol{p}}^2\left(1 - \frac{\Sigma_1}{2t}\right)\left(1 - \frac{\Sigma_1}{t}\right)}{(i\omega_n - \Sigma_0)^2 - \varepsilon_{\boldsymbol{p}}^2\left(1 - \frac{\Sigma_1}{t}\right)^2} \\
&\approx 2T\sum_n \int (dp)\left(\frac{\Sigma_0}{2}(i\omega_n - \Sigma_0) + \varepsilon_{\boldsymbol{p}}^2\left(1 - \frac{\Sigma_1}{2t}\right)\left(1 - \frac{\Sigma_1}{t}\right)\right) \times \\
&\qquad\qquad\qquad\qquad \times\left(\frac{1}{(i\omega_n - \Sigma_0)^2} + \frac{\varepsilon_{\boldsymbol{p}}^2\left(1 - \frac{\Sigma_1}{t}\right)^2}{(i\omega_n - \Sigma_0)^4}\right)
\end{aligned}
\tag{A.45}
$$

---

[3]For the evaluation of the integrals in this chapter, the following equations were used: $\int (d\omega)\frac{1}{\phi^2 + \omega^2} \approx \frac{\pi}{\phi}$, $\int (d\omega)\frac{1}{(\phi^2 + \omega^2)^2} \approx \frac{\pi}{2\phi^3}$, $\int (d\omega)\frac{1}{(\phi^2 + \omega^2)^3} \approx \frac{3\pi}{8\phi^5}$, $\int (d\omega)\frac{\omega^2}{(\phi^2 + \omega^2)^2} \approx \frac{\pi}{2\phi}$, $\int (d\omega)\frac{\omega^2}{(\phi^2 + \omega^2)^3} \approx \frac{\pi}{8\phi^3}$, $\int (d\omega)\frac{\omega^4}{(\phi^2 + \omega^2)^3} \approx \frac{3\pi}{8\phi}$.

$$E \approx 2T \sum_n \int (dp) \left(\frac{\frac{\Sigma_0}{2}}{i\omega_n - \Sigma_0} + \frac{\varepsilon_{\boldsymbol{p}}^2 \left(1 - \frac{\Sigma_1}{2t}\right)\left(1 - \frac{\Sigma_1}{t}\right)}{(i\omega_n - \Sigma_0)^2} + \frac{\frac{\Sigma_0 \varepsilon_{\boldsymbol{p}}^2}{2}\left(1 - \frac{\Sigma_1}{t}\right)^2}{(i\omega_n - \Sigma_0)^3} \right)$$

$$\approx T \sum_n \left(\frac{\Sigma_0}{i\omega_n - \Sigma_0} + \frac{2K_d \left(1 - \frac{\Sigma_1}{2t}\right)\left(1 - \frac{\Sigma_1}{t}\right)}{(i\omega_n - \Sigma_0)^2} + \frac{\Sigma_0 K_d \left(1 - \frac{\Sigma_1}{t}\right)^2}{(i\omega_n - \Sigma_0)^3} \right)$$

$$\approx T \sum_n \left(\frac{\phi^2 - \frac{K_d \phi^2 \left(1 - \frac{\phi^2 S}{\omega_n^2}\right)^2 \left(1 - \frac{1}{2d}\right) + t^2 \phi^2 \left(1 + \frac{\phi^2 S}{\omega_n^2}\right)}{\omega_n^2 + \phi^2}}{-\omega_n^2 - \phi^2 + \frac{K_d \phi^2 \left(1 - \frac{\phi^2 S}{\omega_n^2}\right)^2 \left(1 - \frac{1}{2d}\right) + t^2 \phi^2 \left(1 + \frac{\phi^2 S}{\omega_n^2}\right)}{\omega_n^2 + \phi^2}} \right. \tag{A.46}$$

$$\left. - \frac{2K_d \omega_n^2 \left(1 - \frac{\phi^2 S}{2\omega_n^2}\right)\left(1 - \frac{\phi^2 S}{\omega_n^2}\right)}{(\omega_n^2 + \phi^2)^2} + \frac{K_d \phi^2 \omega_n^2 \left(1 - \frac{\phi^2 S}{\omega_n^2}\right)^2}{(\omega_n^2 + \phi^2)^3} \right),$$

where after the expansion in terms of $(i\omega_n - \Sigma_0)^{-1}$ we neglected all $\mathcal{O}\left[(i\omega_n - \Sigma_0)^{-4}\right]$ and higher order terms in the following line. The expansion in terms of $(\omega_n^2 + \phi^2)^{-1}$ leads to

$$E \approx -T \sum_n \left[\left(\phi^2 - \frac{K_d \phi^2 \left(1 - \frac{\phi^2 S}{\omega_n^2}\right)^2 \left(1 - \frac{1}{2d}\right) + t^2 \phi^2 \left(1 + \frac{\phi^2 S}{\omega_n^2}\right)}{\omega_n^2 + \phi^2} \right) \times \right.$$

$$\times \left(\frac{1}{\omega_n^2 + \phi^2} + \frac{K_d \phi^2 \left(1 - \frac{\phi^2 S}{\omega_n^2}\right)^2 \left(1 - \frac{1}{2d}\right) + t^2 \phi^2 \left(1 + \frac{\phi^2 S}{\omega_n^2}\right)}{(\omega_n^2 + \phi^2)^3} \right)$$

$$\left. + \frac{2K_d \omega_n^2 \left(1 - \frac{\phi^2 S}{2\omega_n^2}\right)\left(1 - \frac{\phi^2 S}{\omega_n^2}\right)}{(\omega_n^2 + \phi^2)^2} - \frac{K_d \phi^2 \omega_n^2 \left(1 - \frac{\phi^2 S}{\omega_n^2}\right)^2}{(\omega_n^2 + \phi^2)^3} \right]$$

$$\approx -T \sum_n \left[\frac{\phi^2}{\omega_n^2 + \phi^2} - \frac{K_d \left(1 - \frac{\phi^2 S}{\omega_n^2}\right)\left[\phi^2 - 2\omega_n^2 + \phi^2 S - \frac{\phi^4 S}{\omega_n^2}\right] + \frac{K_d}{2d}\phi^2 \left(3\frac{\phi^2 S}{\omega_n^2} - \frac{\phi^4 S^2}{\omega_n^4}\right)}{(\omega_n^2 + \phi^2)^2} \right.$$

$$\left. + \frac{K_d \phi^2 \left(1 - \frac{\phi^2 S}{\omega_n^2}\right)^2 (\phi^2 - \omega_n^2) + \frac{K_d}{2d}\phi^4 \left(3\frac{\phi^2 S}{\omega_n^2} - \frac{\phi^4 S^2}{\omega_n^4}\right)}{(\omega_n^2 + \phi^2)^3} \right]$$

$$= -T \sum_n \left[\frac{\phi^2}{\omega_n^2 + \phi^2} + \frac{K_d}{(\omega_n^2 + \phi^2)^3} \left\{ 2\omega_n^4 - \left(3\phi^2 \omega_n^2 + \phi^4 \left(\frac{3}{2d} - 1\right)\right) S \right. \right.$$

$$\left. \left. + \left(\phi^4 - \frac{\phi^6}{\omega_n^2}\left(1 - \frac{1}{2d}\right)\right) S^2 \right\} \right]$$

$$\tag{A.47}$$

and substitution of the sum and evaluation of the integral and calculation of the divergent term yield

$$
E \approx -\frac{1}{2}\left[\phi + K_d\left\{\frac{3}{4\phi} - \left(\frac{3}{8\phi} + \frac{3}{8\phi}\left(\frac{3}{2d} - 1\right)\right)S\right.\right.
$$
$$
\left.\left. + \left(\frac{3}{8\phi} - 2\frac{1}{4T}\left(1 - \frac{1}{2d}\right)\right)S^2\right\}\right] \quad \text{(A.48)}
$$
$$
= -\frac{\phi}{2} - \frac{K_d}{16\phi}\left(6 - \frac{9}{2d}S + 3S^2\right) + \frac{K_d}{4T}\left(1 - \frac{1}{2d}\right)S^2,
$$

the approximated internal energy as a function of ϕ in the fictive impurity case. The ϕ-substitution leads to

$$
E \approx -\frac{1}{2}\left[\frac{U}{2} - \frac{K_d}{2U} + \frac{K_d}{2U}\left(6 - \frac{5}{2d}\right)S - \frac{K_d}{T}\left(1 - \frac{1}{2d}\right)S^2\right]
$$
$$
- \frac{K_d}{8U}\left(6 - \frac{9}{2d}S + 3S^2\right) + \frac{K_d}{4T}\left(1 - \frac{1}{2d}\right)S^2 \quad \text{(A.49)}
$$
$$
= -\frac{U}{4} - \frac{K_d}{2U} - \frac{K_d}{2U}\left(3 - \frac{19}{8d}\right)S - \frac{3K_d}{8U}S^2 + \frac{3K_d}{4T}\left(1 - \frac{1}{2d}\right)S^2.
$$

Note, the energy contains a low-T divergent term, which influence can be seen in the section 1.5.

Dynamical Cluster Approximation

Now we apply the approximate treatment of the previous section to the two-site dynamical cluster approximation. Again the self-energy is defined as

$$
\Sigma(\boldsymbol{p}, \omega_n) = \begin{cases} \Sigma_0 + \Sigma_1 & \text{if } \varepsilon_{\boldsymbol{p}} < 0 \\ \Sigma_0 - \Sigma_1 & \text{else,} \end{cases} \quad \text{(A.50)}
$$

and the Green functions become

$$
G_0 = \frac{1}{2}\int (dp)\left(\frac{1}{i\omega_n - \Sigma_0 - (|\varepsilon_{\boldsymbol{p}}| + \Sigma_1)} + \frac{1}{i\omega_n - \Sigma_0 + (|\varepsilon_{\boldsymbol{p}}| + \Sigma_1)}\right)
$$
$$
= \frac{1}{2(i\omega_n - \Sigma_0)}\int (dp)\frac{2}{1 - \left(\frac{|\varepsilon_{\boldsymbol{p}}| + \Sigma_1}{i\omega_n - \Sigma_0}\right)^2} \approx \frac{\int (dp)\left(1 + \left(\frac{|\varepsilon_{\boldsymbol{p}}| + \Sigma_1}{i\omega_n - \Sigma_0}\right)^2\right)}{i\omega_n - \Sigma_0}
$$
$$
= \frac{1}{i\omega_n - \Sigma_0}\left(1 + \frac{K_d + 2I_d\Sigma_1 + \Sigma_1^2}{(i\omega_n - \Sigma_0)^2}\right) \quad \text{(A.51)}
$$
$$
G_1 = \frac{1}{2}\int (dp)\left(\frac{1}{i\omega_n - \Sigma_0 - (|\varepsilon_{\boldsymbol{p}}| + \Sigma_1)} - \frac{1}{i\omega_n - \Sigma_0 + (|\varepsilon_{\boldsymbol{p}}| + \Sigma_1)}\right)
$$
$$
= \frac{1}{2(i\omega_n - \Sigma_0)}\int (dp)\frac{2\frac{|\varepsilon_{\boldsymbol{p}}| + \Sigma_1}{i\omega_n - \Sigma_0}}{1 - \left(\frac{|\varepsilon_{\boldsymbol{p}}| + \Sigma_1}{i\omega_n - \Sigma_0}\right)^2} \approx \frac{\int (dp)\left(|\varepsilon_{\boldsymbol{p}}| + \Sigma_1\right)}{(i\omega_n - \Sigma_0)^2} = \frac{I_d + \Sigma_1}{(i\omega_n - \Sigma_0)^2},
$$

with $I_d = \int (dp) |\varepsilon_{\boldsymbol{p}}|$. Analog to the fictive impurity case we figure out the Weiss field

$$
\begin{aligned}
a_0 &= \Sigma_0 + \frac{G_0}{G_0^2 - G_1^2} \approx \Sigma_0 + \frac{1}{G_0} + \frac{G_1^2}{G_0^3} \\
&\approx \Sigma_0 + (i\omega_n - \Sigma_0) \left(1 - \frac{K_d + 2I_d\Sigma_1 + \Sigma_1^2}{(i\omega_n - \Sigma_0)^2} \right) + (i\omega_n - \Sigma_0)^3 \frac{(I_d + \Sigma_1)^2}{(i\omega_n - \Sigma_0)^4} \\
&= i\omega_n + \frac{I_d^2 - K_d}{i\omega_n - \Sigma_0} \approx i\omega_n \left(1 + \frac{K_d - I_d^2}{\omega_n^2 + \phi^2} \right) \\
a_1 &= \Sigma_1 - \frac{G_1}{G_0^2 - G_1^2} \approx \Sigma_1 - \frac{G_1}{G_0^2}\Sigma_1 - (i\omega_n - \Sigma_1)^2 \frac{I_d + \Sigma_1}{(i\omega_n - \Sigma_0)^2} = -I_d,
\end{aligned}
\tag{A.52}
$$

where the on-site self-energy was substituted by $\frac{\phi^2}{i\omega_n}$. Substitution of the Weiss field in the self-energy equation (1.104) yields

$$
\begin{aligned}
\Sigma_0 &\approx \frac{\phi^2}{i\omega_n \left(1 + \frac{K_d - I_d^2}{\omega_n^2 + \phi^2} \right)} \left[1 - \frac{I_d^2}{\omega_n^2 + \phi^2} \left(1 + \frac{\phi^2 S^2}{\omega_n^2} \right) \right] \\
&\approx \frac{\phi^2}{i\omega_n} \left(1 - \frac{K_d - I_d^2}{\omega_n^2 + \phi^2} \right) \left[1 - \frac{I_d^2}{\omega_n^2 + \phi^2} \left(1 + \frac{\phi^2 S^2}{\omega_n^2} \right) \right] \\
&\approx \frac{\phi^2}{i\omega_n} \left(1 - \frac{K_d + \frac{I_d^2 \phi^2 S^2}{\omega_n^2}}{\omega_n^2 + \phi^2} \right) \\
\Sigma_1 &\approx -\frac{I_d \phi^2 S}{\omega_n^2}.
\end{aligned}
\tag{A.53}
$$

Solution of the equation (1.102) leads to the expression for ϕ

$$
\begin{aligned}
\frac{1}{U} &\approx -T \sum_n \left(\frac{-1}{\omega_n^2 \left(1 + \frac{K_d - I_d^2}{\omega_n^2 + \phi^2} \right)^2 + \phi^2} - \frac{I_d^2 \left(-2\omega_n^2 + S \left(-\omega_n^2 + \phi^2 \right) \right)}{(\omega_n^2 + \phi^2)^3} \right) \\
&\approx T \sum_n \left(\frac{1}{\omega_n^2 + \phi^2} \left(1 - \frac{2\omega_n^2 (K_d - I_d^2)}{(\omega_n^2 + \phi^2)^2} \right) + \frac{I_d^2 \phi^2 S - I_d^2 \omega_n^2 (2 + S)}{(\omega_n^2 + \phi^2)^3} \right) \\
&\approx \frac{1}{2\pi} \int d\omega \left(\frac{1}{\omega_n^2 + \phi^2} - \frac{2\omega_n^2 (K_d - I_d^2)}{(\omega_n^2 + \phi^2)^3} + \frac{I_d^2 \phi^2 S - I_d^2 \omega_n^2 (2 + S)}{(\omega_n^2 + \phi^2)^3} \right) \\
&\approx \frac{1}{2\phi} - \frac{2(K_d - I_d^2)}{16\phi^3} + \frac{3I_d^2 S}{16\phi^3} - \frac{I_d^2 (2 + S)}{16\phi^3} \approx \frac{1}{2\phi} + \frac{I_d^2 S - K_d}{8\phi^3},
\end{aligned}
\tag{A.54}
$$

which can be solved on the same way like in the subsection 1.4.2, so

$$
\phi = \frac{U}{2} - \frac{K_d}{2U} + \frac{I_d^2}{2U} S.
\tag{A.55}
$$

Again, in order to get the internal energy we expand the energy keeping all $(i\omega_n - \Sigma_0)^{-1}$-terms up to the third order, evaluate the momentum integration, substitute the self-energy and expand in terms of $(\omega_n^2 + \phi^2)^{-1}$:

$$
\begin{aligned}
E &= T\sum_n \int (dp) \mathrm{Tr}\left[\left(\hat{\varepsilon}_{\boldsymbol{p}} + \frac{1}{2}\hat{\Sigma}\right)\hat{G}^{-1}\right] \\
&= 2T\sum_n \int (dp) \frac{\frac{1}{2}\Sigma_0(i\omega_n - \Sigma_0) + \left(|\varepsilon_{\boldsymbol{p}}| + \frac{1}{2}\Sigma_1\right)\left(|\varepsilon_{\boldsymbol{p}}| + \Sigma_1\right)}{(i\omega_n - \Sigma_0)^2 - (|\varepsilon_{\boldsymbol{p}}| + \Sigma_1)^2} \\
&\approx 2T\sum_n \int (dp) \left(\frac{\Sigma_0}{2}(i\omega_n - \Sigma_0) + \varepsilon_{\boldsymbol{p}}^2 + \frac{3\Sigma_1|\varepsilon_{\boldsymbol{p}}|}{2} + \frac{\Sigma_1^2}{2}\right) \times \\
&\qquad\qquad\qquad\qquad \times \left(\frac{1}{(i\omega_n - \Sigma_0)^2} + \frac{(|\varepsilon_{\boldsymbol{p}}| + \Sigma_1)^2}{(i\omega_n - \Sigma_0)^4}\right) \\
&\approx 2T\sum_n \int (dp) \left(\frac{\Sigma_0}{2(i\omega_n - \Sigma_0)} + \frac{\varepsilon_{\boldsymbol{p}}^2 + \frac{3\Sigma_1|\varepsilon_{\boldsymbol{p}}|}{2} + \frac{\Sigma_1^2}{2}}{(i\omega_n - \Sigma_0)^2} + \frac{\Sigma_0(|\varepsilon_{\boldsymbol{p}}| + \Sigma_1)^2}{2(i\omega_n - \Sigma_0)^3}\right) \\
&= T\sum_n \left(\frac{\Sigma_0}{i\omega_n - \Sigma_0} + \frac{2K_d + 3I_d\Sigma_1 + \Sigma_1^2}{(i\omega_n - \Sigma_0)^2} + \frac{\Sigma_0(K_d + 2I_d\Sigma_1 + \Sigma_1^2)}{(i\omega_n - \Sigma_0)^3}\right) \\
&\approx T\sum_n \left(\frac{\frac{\phi^2}{i\omega_n}\left(1 - \frac{K_d + \frac{I_d^2\phi^2 S^2}{\omega_n^2}}{\omega_n^2 + \phi^2}\right)}{i\omega_n - \frac{\phi^2}{i\omega_n}\left(1 - \frac{K_d + \frac{I_d^2\phi^2 S^2}{\omega_n^2}}{\omega_n^2 + \phi^2}\right)} + \frac{2K_d - \frac{3I_d^2\phi^2 S}{\omega_n^2} + \frac{I_d^2\phi^4 S^2}{\omega_n^4}}{\left(i\omega_n - \frac{\phi^2}{i\omega_n}\right)^2}\right. \\
&\qquad\qquad\qquad\qquad\qquad\qquad \left. + \frac{\frac{\phi^2}{i\omega_n}\left(K_d - \frac{2I_d^2\phi^2 S}{\omega_n^2} + \frac{I_d^2\phi^4 S^2}{\omega_n^4}\right)}{\left(i\omega_n - \frac{\phi^2}{i\omega_n}\right)^3}\right) \\
&\approx T\sum_n \left(-\frac{\phi^2\left(1 - \frac{K_d + \frac{I_d^2\phi^2 S^2}{\omega_n^2}}{\omega_n^2 + \phi^2}\right)}{\omega_n^2 + \phi^2 - \frac{K_d\phi^2 + \frac{I_d^2\phi^4 S^2}{\omega_n^2}}{\omega_n^2 + \phi^2}} - \frac{2K_d\omega_n^2 - 3I_d^2\phi^2 S + \frac{I_d^2\phi^4 S^2}{\omega_n^2}}{(\omega_n^2 + \phi^2)^2}\right. \\
&\qquad\qquad\qquad\qquad\qquad\qquad \left. + \frac{\phi^2\left(K_d\omega_n^2 - 2I_d^2\phi^2 S + \frac{I_d^2\phi^4 S^2}{\omega_n^2}\right)}{(\omega_n^2 + \phi^2)^3}\right).
\end{aligned}
$$

(A.56)

Expansion, substitution of the Matsubara sum and evaluation of the integrals give the approximated energy for 2-site DCA:

$$
\begin{aligned}
E \approx &-T \sum_n \left(\phi^2 \left(1 - \frac{K_d + \frac{I_d^2 \phi^2 S^2}{\omega_n^2}}{\omega_n^2 + \phi^2} \right) \left(\frac{1}{\omega_n^2 + \phi^2} + \frac{K_d \phi^2 + \frac{I_d^2 \phi^4 S^2}{\omega_n^2}}{(\omega_n^2 + \phi^2)^3} \right) \right. \\
&\left. + \frac{2K_d \omega_n^2 - 3I_d^2 \phi^2 S + \frac{I_d^2 \phi^4 S^2}{\omega_n^2}}{(\omega_n^2 + \phi^2)^2} - \frac{\phi^2 \left(K_d \omega_n^2 - 2I_d^2 \phi^2 S + \frac{I_d^2 \phi^4 S^2}{\omega_n^2} \right)}{(\omega_n^2 + \phi^2)^3} \right) \\
\approx &-T \sum_n \left(\phi^2 \left(\frac{1}{\omega_n^2 + \phi^2} - \frac{K_d}{(\omega_n^2 + \phi^2)^2} + \frac{K_d \phi^2}{(\omega_n^2 + \phi^2)^3} \right) \right. \\
&\left. + \frac{2K_d \omega_n^2 - 3I_d^2 \phi^2 S}{(\omega_n^2 + \phi^2)^2} - \frac{\phi^2 \left(K_d \omega_n^2 - 2I_d^2 \phi^2 S \right)}{(\omega_n^2 + \phi^2)^3} \right) \\
\approx &-\frac{1}{2} \left(\frac{\phi^2}{\phi} - \frac{K_d \phi^2}{2\phi^3} + \frac{3K_d \phi^4}{8\phi^5} + \frac{2K_d}{2\phi} - \frac{3I_d^2 \phi^2 S}{2\phi^3} - \frac{K_d \phi^2}{8\phi^3} + \frac{6I_d^2 \phi^4 S}{8\phi^5} \right) \\
= &-\frac{1}{2} \left(\phi + \frac{3K_d}{4\phi} - \frac{3I_d^2 S}{4\phi} \right) \approx -\frac{U}{4} - \frac{K_d}{2U} + \frac{I_d^2}{2U} S.
\end{aligned}
\tag{A.57}
$$

Note, that the internal energy is T- and S^2-independent and the S-term reduces the energy (compare figure 1.14).

Appendix B

Zusammenfassung

In dieser Arbeit haben wir uns mit Systemen stark korrelierter Fermionen beschäftigt. Es wurde eine Reihe von neuen numerischen Methoden untersucht sowie deren Gültigkeitsbereiche identifiziert. Ferner haben wir unsere Ergebnisse mit denen aus älteren numerischen Methoden verglichen und diverse physikalische Größen und Phasenübergänge untersucht. Unsere numerischen Ergebnisse wurden im analytischen Teil der Arbeit bestätigt.

B.1   Kapitel 1

1. Die vor kurzem entwickelte semiklassische Näherung (SCA) für die Lösung im Störstellenproblem wurde bei verschiedenen Stärken der Coulomb'schen Wechselwirkung U untersucht und mit dem etablierten Quanten-Monte-Carlo-Algorithmus (QMC) verglichen. Wir haben gefunden, dass die numerische Ergebnisse beider Methoden sehr gut übereinstimmen, wobei der Vorteil der SCA eine enorme Zeitersparnis (SCA ist bis zu 100 mal schneller) im Bereich starker Coulomb-Abstoßung ist, was extrem wichtig für die Modellierung von Multistörstellenclustern ist. Außerdem haben wir zwei verschiedene Modifikationen der SCA untersucht und sind zur Erkenntnis gekommen, dass die Sattelpunktsapproximation (SPA) nur für starke Wechselwirkung funktioniert und für kleine bis mittlere U zusammenbricht.

2. Um die Richtigkeit der numerischen Befunde zu überprüfen, haben wir beide 2-Störstellen Methoden (also die Methode der fiktiven Störstellen (FI) und Dynamical Cluster Approximation (DCA)) analytisch untersucht. Es wurde gefunden, dass beide Verfahren die innere Energie bis zu Entwicklungsordnung $\mathcal{O}(t^2/U)$ exakt reproduzieren. Dennoch führt der nächste Term $\mathcal{O}(t^4/(TU^2))$, der die Spin-Spin-Wechselwirkung zwischen zwei Störstellen beinhaltet, zu einem unphysikalischen Verlauf der Energie. Aufgrund unserer analytischen Ergebnisse zweifeln wir an einer früheren Behauptung [39], dass eine Erweiterung der Dynamical Mean Field Theory (DMFT), wie zum Beispiel unsere FI-Methode, automatisch zu einer doppelten Zählung von Prozessen, die das Hüpfen zwischen Störstellen einbinden, führt.

Unsere Untersuchung hat gezeigt, dass bei den betrachteten Algorithmen die Spin-Terme für die Probleme verantwortlich sind.

3. Wir haben verschiedene Multistörstellencluster numerisch untersucht und eine Reihe von physikalischen Größen wie die Selbstenergie, die Spin-Spin-Korrelation, die Energie sowie die Néel-Temperatur bestimmt. Wir stellten fest, dass weder FI-Methode noch DCA vollständig korrekte physikalische Ergebnisse liefern. Die FI-Methode "findet" einige unphysikalische Zustände mit geringem Gewicht in der Mitte des Mott-Hubbard-Gap, wobei wachsende Cluster-Größe das Gewicht dieser Zuständen drastisch reduziert. Wir haben auch gezeigt, dass eine einfache Filterprozedur im FI-Algorithmus zu physikalisch richtigen Ergebnissen führt. Beide Algorithmen schätzen die Néel Temperatur nicht ganz korrekt ab, wobei die steigende Anzahl von Störstellen in der FI-Methode zur Konvergenz gegen das analytische Ergebnis führt. Dynamical Cluster Approximation tendiert dagegen in die falsche Richtung.

4. Eine mögliche Fehlerquelle ist die Annahme, dass alle benachbarten Selbst-Energien durch eine einzige Funktion dargestellt werden dürfen. Eine separate Behandlung der Beiträge zur Selbst-Energie könnte die Ergebnisse verbessern, was in dieser Arbeit wegen des Rechenaufwands unrealistisch war. Um die FI-Methode weiter zu entwickeln, sollte man einen zusätzlichen Term $J \sim t^2/U$ einzubinden, um den Effekt von Spin-Korrelationen auszugleichen. Ferner sollte ein Vergleich zwischen Cellular-DMFT [10] und unserer FI-Methode in der Zukunft untersucht werden.

B.2   Kapitel 2

1. Ein System aus zwei gekoppelten Hubbard-Ebenen wurde betrachtet. Wir haben das System mit der Dynamical Mean Field Theory (DMFT) untersucht, wobei das zwei-Störstellen-Problem mit einem Quanten-Monte-Carlo-Algorithmus gelöst wurde. Die analytische Fortsetzung erfolgte durch die Maximum-Entropy-Prozedur. Außerdem haben wir zwei verschiedene Algorithmen zur Bestimmung der optischen Leitfähigkeit untersucht. Dabei haben wir herausgefunden, dass beide Methoden ähnliche optische Leitfähigkeiten liefern. Allerdings stellten wir auch fest, dass der von N. Blümer [28] vorgeschlagene Algorithmus für die Bestimmung des Drude Gewichtes wesentlich besser geeignet ist.

2. Wir haben die Ein-Teilchen-Zustandsdichte, die optische Leitfähigkeit sowie das Drude-Gewicht für verschiedene Bereiche des Phasendiagramms bestimmt. Es wurden der Mott-Hubbard- und der Metall-Band-Isolator-Phasenübergang gefunden und klassifiziert. Wir haben keinen eindeutigen Phasenübergang zwischen beiden Isolatoren gefunden. Das Phasendiagramm zeigt zum Teil bemerkenswerte Unterschiede zu dem Diagramm von Moeller, wobei wir die Differenz mit dem Temperatur- und dem Methodenunterschied begründen. Qualitativ stimmen unsere Ergebnisse jedoch überein.

3. Für die weitere Untersuchung dieses Modells sollte man sich die Spin-Korrelation zwischen den entsprechenden Gitterplätzen der beiden Hubbard Ebenen ansehen sowie deren Einfluß auf die Eigenschaften des Systems und des Phasendiagramms untersuchen. Ferner verspricht die Betrachtung des zwei-Ebenen-Hubbard-Modells abseits halber Füllung eine Reihe von interessanten Ergebnissen.

List of Figures

List of Symbols And Abbreviations

$\langle A \rangle$	expectation value of A
$A_{S/A}$	sym./antisym. DOS
a	Weiss field
Anti	antiferromagnetic regime
BZ	Brillouin zone
β	reciprocal temperature
c	fermionic annihilation oper.
$c^\dagger$	fermionic creation oper.
D	Drude weight
DC	direct current
$D(\varepsilon)$	free DOS
$\tilde{D}(\omega_n)$	Hilbert transformed DOS
DCA	dynamical cluster approx.
DMFT	dynamical mean field theory
DOS	density of states
d	dimension
det	determinant
diag	diagonal matrix
δ	small correction
δ_{ij}	Kronecker delta
$\delta(x)$	delta function
E	internal energy
$\boldsymbol{E}$	electric field
$\varepsilon_{\boldsymbol{p}}$	dispersion relation
FI	fictive impurity (method)
FT	Fourier transformation
f	filtering
G	Green function
$\mathcal{G}$	free Green function
γ_i	set of orthogonal functions
H	Hamilton operator
HST	Hubbard-Stratonovich transf.
IFT	inverse Fourier transf.
IPT	iterated perturbation theory
I_d	$\int(dp)\lvert\varepsilon_{\boldsymbol{p}}\rvert$
Im	imaginary part

Imp.	impurity
Int-SCA	original SCA
$\int(dp)$	$\int_{\mathrm{BZ}} \frac{(dp)^d}{(2\pi)^d}$
J	magnetic exchange
K	kinetic energy
K_d	$\int(dp)\varepsilon_{\boldsymbol{p}}^2 = 2dt^2$
L	number of time slices in QMC
LHB	lower Hubbard band
$L(\omega)$	Lorentz curve
$\hat{\Lambda}$	matrix of auxiliary fields
$\hat{M}_i$	set of "orthogonal" matrices
μ	chemical potential
$\mathrm{N_{min}}$	number of minima of potential
NN	nearest neighbor
NNN	next nearest neighbor
n_σ	spin-σ particle number oper.
ν	real frequency
ν_m	bosonic Matsubara frequency
Ω	thermodynamical potential
ω_n	fermionic Matsubara frequency
ω	real frequency
P	probability
$\mathcal{P}$	principal part
Para	paramagnetic regime
$\boldsymbol{p}$	momentum space vector
Φ	Luttinger-Ward functional
ϕ	auxiliary field
$\boldsymbol{\phi}$	vector of aux. fields
ϕ_i	set of orthogonal functions
ψ_i	set of orthogonal functions
φ	auxiliary field
$\boldsymbol{\varphi}$	vector of aux. fields
QMC	Quantum Monte-Carlo
RBZ	reduced Brillouin zone
Re	real part
$\mathbf{r}$	real space vector

SCA	Semiclassical Approximation	Tr	trace
S	$\sigma_i \sigma_j$ or entropy	T_N	Néel temperature
Sum-SCA	$\int$ was substituted by $\sum$	t	hopping matrix el. in DMFT
S^{eff}	effective action	t_{ij}	in-plane hopping matrix el.
S_{iz}	z spin projection $\left(\pm\frac{1}{2}\right)$	$t_\perp$	inter-plane hopping matrix el.
$\boldsymbol{s}$	vector of Ising spins	τ	imaginary time
s_i	auxiliary field	U	Coulomb repulsion
Σ	self-energy	UHB	upper Hubbard band
σ	optical conductivity or spin	V^{eff}	effective potential
OC	optical conductivity	x_C	critical value of x
σ_z	$= 1(-1)$, if $\sigma = \uparrow (\downarrow)$	Z	partition function
T	temperature	z	number of nearest neighbors

Bibliography

[1] M. Imada, A. Fujimori, and Y. Tokura, *Rev. of Mod. Phys.* **70**, 1039 (1998).

[2] J. G. Bednorz and K. A. Müller, *Z. Phys. B* **64**, 189 (1986).

[3] L. H. Chen, S. Jin, T. H. Tiefel, S. H. Chang, M. Eibschutz, and R. Ramesh, *Phys. Rev. B* **49**, 9194-9197 (1994).

[4] A. Georges, G. Kotliar, W. Krauth, M. J. Rozenberg,*Rev. of Mod. Phys.* **68**, 13 (1996).

[5] M. J. Rozenberg, G. Kotliar, and X. Y. Zhang, *Phys. Rev. B* **49**, 10181-10193 (1994).

[6] A. J. Millis, R. Mueller, and B. I. Shraiman, *Phys. Rev. B* **54**, 5405 (1996).

[7] I. A. Nekrasov, Z. V. Pchelkina, G. Keller, Th. Pruschke, K. Held, A. Krimmel, D. Vollhardt, and V. I. Anisimov, *Phys. Rev. B* **67**, 085111 (2003).

[8] A. J. Millis, R. Lobo, A. Zimmers, N. Bontemps and C. C. Homes, cond-mat/0411172.

[9] D. N. Argyriou, J. W. Lynn, R. Osborn, B. Campbell, J. F. Mitchell, U. Ruett, H. N. Bordallo, A. Wildes, and C. D. Ling, *Phys. Rev. Lett.* **89**, 036401 (2002).

[10] G. Kotliar, S. Y. Savrasov, G. Pálsson, and G. Biroli, *Phys. Rev. Lett.* **87**, 186401 (2001).

[11] M. H. Hettler, A. N. Tahvildar-Zadeh, M. Jarrell, T. Pruschke, and H. R. Krishna-murthy, *Phys. Rev. B* **58**, R 7475 (1998).

[12] S. Okamoto, A. J. Millis, H. Monien, and A. Fuhrmann, *Phys. Rev. B* **68**, 195121 (2003).

[13] J. Hubbard, *Phys. Rev. Lett.* **3**, 77 (1959).

[14] S. Okamoto, A. Fuhrmann, A. Comanac, and A. J. Millis, *Phys. Rev. B* **71**, 235113 (2005).

[15] A. A. Abrikosov, L. P. Gorkov, and I. E. Dzyaloshinski, *Methods of Quantum Field Theory in Statistical Physics*, Chapter 3, p. 142, Dover (1963).

BIBLIOGRAPHY

[16] M. Potthoff *Eur. Phys. J. B* **32**, 429 (2003).

[17] A. L. Fetter, J. D. Walecka, *Quantum theory of many-particle systems*, McGraw-Hill Book Company, (1971).

[18] K. Kubo, *Prog. of Theo. Phys.* Vol. **64, No. 3**, 758 (1980).

[19] H. Hasegawa, *J. Phys. Soc. Jpn.* **49**, 178 (1980).

[20] H. Hasegawa, *J. Phys. Soc. Jpn.* **49**, 963 (1980).

[21] R. L. Stratonovich, *Dokl. Akad. Nauk SSSR* **115**, 1097 (1958).

[22] S. Blawid and A. J. Millis, *Phys. Rev. B* **62** 2424 (2000).

[23] S. Pankov, G. Kotliar, and Y. Motome, *Phys. Rev. B* **66** 045117 (2002).

[24] S. Okamoto: private communication.

[25] J. E. Hirsch, R. M. Fye, *Phys. Rev. Lett.* **56, No 23**, 2521 (1986).

[26] J. E. Hirsch, *Phys. Rev. B* **28, No 7**, 4059 (1983).

[27] W. H. Press, S. A. Teukolsky, W. T. Vetterling, B. P. Flannery, *Numerical Recipes in C*, (Cambrige university press, 1988).

[28] N. Bluemer, *PhD theses*, Universität Augsburg (2001).

[29] W. von der Linden, *Appl. Phys. A* **60**, 155-165 (1995).

[30] W. von der Linden, R. Preuss, W. Hanke: preprint `cond-mat/9503098` (1995).

[31] J. Skilling, *Maximum Entropie and Bayesian Methods*, (Kluwer, Dordrech 1990).

[32] M. Jarrell, J. E. Gubernatis *Phys. Rep.* **269**, 133-195 (1996).

[33] A. Fuhrmann, *Diploma theses*, Universität Bonn (2003).

[34] A. J. Millis: private communication.

[35] A. Fuhrmann, S. Okamoto, H. Monien, and A. J. Millis, preprint `cond-mat/0605133`.

[36] I. N. Bronstein, K. A. Semerdjajew, *Teubner-Taschenbuch der Mathematik*, Teubner (1996).

[37] R. K. Pathria *Statistical Mechanics*, Pergamon (1972).

[38] M. Jarrell, Th. Maier, C. Huscraft and S. Mukouri, Phys. Rev. B **64**, 195130 (2001).

[39] A. Schiller and K. Ingersent, *Phys. Rev. Lett.* **75**, 113-116 (1995).

[40] H. Monien, T. M. Rice, *Physica C* (1994).

[41] A. J. Millis, H. Monien, *Phys. Rev. B* **54, No 22**, 16172 (1996).

[42] R. Stern, M. Mali, J. Roos, D. Brinkmann, *Phys. Rev. B* **52, No 22**, 15734 (1995).

[43] J. M. Tranquada, G. Shirane, K. Keimer, S. Shamoto, M. Sato, *Phys. Rev. B* **40, No 7**, 4503 (1989).

[44] Y. Fukuzumi, K. Mizuhashi, K. Takenaga, S. Uchida, *Phys. Rev. Let.* **76, No 4**, 684 (1996).

[45] P. W. Anderson, *Phys. Rev. Lett.* **67**, 3844 (1991).

[46] P. W. Anderson, *Science* **256**, 1526 (1992).

[47] Z. X. Shen, *Phys. Rep.* **253**, 1 (1995).

[48] H. Ding, *Phys. Rev. Lett.* **76**, 1533 (1996).

[49] W. Pickett, *Rev. Mod. Phys.* **61**, 43 (1989).

[50] M. Potthoff and W. Nolting, *Phys. Rev. B* **59**, 2549 (1999).

[51] M. Potthoff and W. Nolting, *Eur. Phys. J. B* (1999).

[52] S. Biermann, A. Georgess, A. Lichtenstein, and T. Giamarchi, *Phys. Rev. Lett.* **87**, 276405 (2001).

[53] S. Biermann, A. Georgess, T. Giamarchi, and A. Lichtenstein, `cond-mat/0201542` (2002).

[54] B. A. Jones, C. M. Varma, and J. W. Wilkins, *Phys. Rev. Lett.* **61**, 125 (1988).

[55] H. Monien, N. Elstner, A. J. Millis, preprint `cond-mat/9707051` (1997).

[56] F. H. L. Essler and A. M. Tsvelik, *Phys. Rev. B* **65**, 115117 (2002).

[57] I. Dzyaloshinski, *Phys. Rev. B* **68**, 85113 (2003).

[58] F. H. L. Essler and A. M. Tsvelik, *Phys. Rev. B* **71**, 195116 (2005).

[59] R. M. Konik, T. M. Rice, and A. M. Tsvelik, preprint `cond-mat/0511268` (2005).

[60] C. Berthod, T. Giamarchi, S. Biermann, and A. Georges, preprint `cond-mat/0602304` (2006).

[61] A. Rosch, preprint `cond-mat/0602656` (2006).

[62] T. D. Stanescu, P. W. Phillips, and T.-P. Choy, preprint `cond-mat/0602280` (2006).

[63] K.-Y. Yang, T. M. Rice, and F.-C. Zhang, preprint `cond-mat/0602164` (2006).

[64] G. Moeller, V. Dobrosavljević, A. E. Ruckenstein, *Phys. Rev. B* **59**, 6846 (1999).

[65] Th. Pruschke, D. L. Cox, *Phys. Rev. B* **47, No 7**, 3553 (1992).

[66] D. Heilmann: private communication.

[67] A. Fuhrmann, D. Heilmann, and H. Monien, preprint `cond-mat/0510150` (2005).

[68] H. Monien: private communication.

[69] W. Metzner, *Phys. Rev. B* **43, No 10**, 8549 (1991).

[70] E. Mueller-Hartmann, *Z. Phys. B* **76**, 211 (1989).

[71] M. Potthoff, preprint `cond-mat/0107502` (2001).

[72] A. Georges, W. Krauth, *Phys. Rev. Lett.* **69**, 1240 (1992).

[73] A. Georges, W. Krauth, *Phys. Rev. B* **48**, 7167 (1993).

[74] A. I. Lichtenstein, A. N. Rubtsov, *JETP Lett.* **80** 61 (2004).

[75] J. E. Hirsch, *Phys. Rev. B* **31**, 4403 (1985).

List Of Publications

"Fictive Impurity Models: An Alternative Formulation Of The Cluster Dynamical Mean-Field Method"
S. Okamoto, A. J. Millis, H. Monien, and A. Fuhrmann,
Physical Review B **68**, 195121 (November 2003).

"Benchmarking A Semiclassical Impurity Solver For Dynamical Mean-Field Theory: Self-Energies And Magnetic Transitions Of The Single-Orbital Hubbard Model"
S. Okamoto, A. Fuhrmann, A. Comanac, and A. J. Millis,
Physical Review B **71**, 235113 (Februar 2005).

"From Mott Insulator to Band Insulator: A DMFT Study"
A. Fuhrmann, D. Heilmann, and H. Monien,
Physical Review B **73**, 245118 (June 2006).

"Fictive Impurity Approach to Dynamical Mean Field Theory: a Strong-Coupling Investigation"
A. Fuhrmann, S. Okamoto, H. Monien, and A. J. Millis,
preprint `cond-mat/0605133`.

Acknowledgments